An Adjoint Analysis of the Great Lakes Hurricane of 2010

by

Craig A. Oswald

A thesis submitted in partial fulfillment of the requirements for the degree of

Master of Science Atmospheric and Oceanic Sciences

at the

UNIVERSITY OF WISCONSIN – MADISON 2018

Abstract

An adjoint-informed case study of the explosively deepening extratropical cyclone that passed through the upper Great Lakes during the period 24-26 October 2010 is conducted by completing a 48-hour numerical weather prediction (NWP) simulation of the event between 0000 UTC 25 October and 0000 UTC 27 October using the Weather Research and Forecast model (WRF-ARW) and its adjoint contained in WRFPLUS. Adjoint-sensitivities of the cyclone intensity, as defined by a response function that is the average dry mass of an atmospheric column surrounding the cyclone, are evaluated over a 48 period. Diagnosis is focused on upper- to mid-tropospheric processes in contrast to many prior adjoint-derived sensitivity studies that focused on mid- to lower-tropospheric processes and features. Initial-time adjoint-derived sensitivities to wind and temperature identify regions within, and more particularly, directly below the jet stream, have the greatest impact on changing the response function, and subsequently, cyclone intensity for this case. Diagnosis of the evolution of adjoint-informed non-optimal and optimal perturbations reveals that enhancement of the precursor upper-tropospheric potential vorticity (PV) anomaly associated with the jet exit region is the most effective means of enhancing cyclone intensity at the final forecast time for this case.

Acknowledgements

Being afforded the opportunity to complete a Master's degree at the University of Wisconsin – Madison is a life feat that I will forever be proud of. Such an endeavor would never have been accomplished without the help of many close family, friends, and colleagues. I would first like to thank my advisor Dr. Michael Morgan for his incredible, and seemingly endless knowledge of adjoint analysis and numerical weather prediction in general. The skills imparted upon me will undoubtedly be critical in the success of my future career. Thank you to my committee members Dr. Jonathan Martin and Dr. Brett Hoover for not only their feedback on this thesis, but also their tutelage throughout the course of this work. Special thanks to my parents for encouraging me to return to UW – Madison for a graduate degree, and continuing that support throughout the way. Thank you to my many friends and family within and outside of the department for not only their academic help, but also being there for me as an outlet to relieve stress and maintain perspective of the journey. Finally, I would like to thank the National Science Foundation for funding this work via research grant AGS – 1638194.

Table of Contents

1. Introduction

a. Background

Mid-latitude cyclones are high impact systems whose annual toll have averaged $37 million in damages across North America between 1985-2014 (Ranson et al. 2016). Diagnosing the dynamical processes that drive the development of these cyclones furthers the understanding of these important weather systems. A case study of the intense 24-26 October 2010 extratropical cyclone that passed through the upper Great Lakes is the focus of this diagnosis. This event developed explosively and featured the merger of two surface circulations into one. A precursor potential vorticity (PV) anomaly associated with super imposed polar and subtropical jet streams over the eastern Pacific and Western United States is the main driver of the development. The minimum sea level pressure (SLP) record was broken for the state of Minnesota as well as other pressure records set by notable extratropical cyclones within the last several decades (Grumm). The combination of the impacts of this event along with the complexity of its dynamics make it one of great interest to study.

The fundamental elements of mid-latitude cyclogenesis are well-known and can be traced to the introduction of the Norwegian Cyclone Model. This model has been crucial in laying the foundation of the modern theory concerning extratropical cyclones. Presented by Jacob Bjerknes, among others, this work has been able to describe the circulation about a cyclone center, the layout of the frontal regions, and the propagation of the cyclone (Fig. 1.1). This was accomplished through the use of sparse observational data available from weather stations at the time, as well as detailed daily weather maps and study of the sky. Based on observations of the cyclonic motion and energy exchanges of warm and cold air lying beside each other on either side of the steering surface, it was concluded that cyclones are most frequent, and develop to the greatest intensity, in zones of great horizontal temperature gradients (Bjerknes 1919).

The Shapiro-Keyser model (Shapiro and Keyser, 1990) describes a similar evolution in the formation of extratropical cyclones. This model shows that there are four distinct stages of the cyclone lifecycle which include the incipient frontal cyclone, frontal fracture, bent-back front and frontal T-bone, and warm core frontal seclusion (Fig. 1.2). It has also shown that cyclone formation and lifecycles are influenced by the dynamics of the jet stream and associated upper

front. Secondary circulations transverse to the mid-latitude jet, diagnosed in a semi-geostrophic frame-work by Sawyer (1956) and Eliassen (1962), help to strengthen the development of an upper frontal region associated with a tropopause fold. It has been found that an upper-tropospheric frontal region, associated with anomalously high PV subducted into the troposphere, is critical in aiding in the initiation of surface mid-latitude cyclogenesis (Hoskins et al. 1985). Hoskins et al. (1985) demonstrated how in typical mid-latitude cyclogenesis, an upper-tropospheric PV anomaly associated with a tropopause undulation interacts with a pre-existing surface baroclinic zone (Fig. 1.3). This mechanism of cyclogenesis has also been previously investigated and described by Petterssen and Smebye (1971). As expressed by Petterssen and Smebye (1971), cyclones that result from the synergistic interaction of a predecessor upper-tropospheric shortwave trough interacting with a surface front have been dubbed 'Type-B' cyclones. Another type of cyclogenesis relevant to the case at hand is *alpine lee cyclogenesis*. Chung et al. (1976) as well as Mattocks and Bleck (1986) maintain that one of the key features for this type of development is the presence of a jet streak and the diffluent flow associated with the exit region oriented perpendicular to an orographic barrier. This type of configuration allows for the ascent associated with the jet exit region and diffluent flow aloft to progress unabated by the inundation of cold, stable air, which is dammed by the orographic barrier, into the region in the lee of the orographic barrier (Fig. 1.4).

b) Adjoints and Cyclogenesis

What is less known about extratropical cyclogenesis is how the dynamical interactions described above might change if small perturbations were made at various stages of the cyclone lifecycle. In the past, studies of this sort have been accomplished through an *impact study* involving the diagnosis of the effect of "intuition-informed" initial perturbations to a numerical weather prediction (NWP) model simulation of an event (Kuo et al., 1991; Zhu and Thorpe, 2006). A control simulation is produced and compared with a perturbed simulation in which a perturbation is made to some variable(s) in the initial model state vector. The perturbation is generally chosen based on what variable or process a researcher decides to investigate to help determine how perturbations to this specific field affect the lifecycle of the cyclone. As a means of assessing the impact of a perturbation, this technique will yield an impact or change on the

final state; however, multiple applications of the technique are required to perform a *sensitivity* analysis. To evaluate, as an example, the sensitivity of a cyclone's intensity to initial state perturbations near the cyclone's upper-tropospheric precursor, multiple perturbations and variables (and numerical integrations) must be performed to assess how small changes in the initial state will impact cyclone intensity. As a means of evaluating sensitivities, multiple impact studies can be both unreliable and inefficient. The unreliability is due to the likelihood that the largest sensitivities might be missed in this approach, or that the synoptic intuition used in identifying where to perturb may have been misguided. The approach is inefficient, because of the high cost of running tens if not hundreds of numerical simulations to assess the phase space of the model appropriately. Indeed, to properly map out the entire phase space of the model, the approach must be repeated for each field in the initial state vector to complete a full diagnostic of what the influence of different perturbations is on cyclone development. This tedious and time consuming procedure can be overcome by application of *adjoint sensitivity analysis*, which is able to determine efficiently, and in many cases reliably, the sensitive regions for all fields in the initial model state vector in a single integration forward followed by a single (backward) adjoint integration.

Having identified a specific feature of a numerical simulation of interest, called the response function, *R*, adjoint analysis identifies sensitivity as the gradient of the response function with respect to the model forecast state, **x**, i.e., the sensitivity is given by $\partial R / \partial \mathbf{x}$. An adjoint-derived sensitivity identifies regions where changes to specific model state variables at the initial forecast time (or along a simulation trajectory) have the largest impact on a selected forecast measure, *R* (Errico 1997). These regions can be perturbed subsequently to produce a desired change in *R* (e.g., the intensity of a simulated cyclone) at the final forecast time. The dynamics most affected by these perturbations during development of the cyclone help to indicate the most important processes critical for development, including explosive development of extratropical cyclones. A more complete description of adjoint models and sensitivity gradients is provided in Chapter 3.

The application of adjoint analysis to models of atmospheric processes first started in the early 1980's when sensitivity analysis applied to a radiative-convective model determined that surface air temperature of the model was most sensitive to saturation vapor pressure (Hall et al., 1982). Subsequent work by Hall and Cacuci (1983) and Cacuci and Hall (1984), further applied

the ideas of adjoint sensitivity analysis to atmospheric processes as simulated by a NWP model. Later works by Langland et al. (1995) apply these techniques specifically to a study of idealized extratropical cyclogenesis where it was determined that temperature and wind in the lower-troposphere, below the jet, were the fields and regions most sensitive to enhanced development of a cyclone. Enhanced heating in the warm sector also was a significant factor that effected cyclone development in their study. Langland et al. (1995) examined adjoint- derived sensitivities in the context of an idealized cyclogenesis event on an f-plane channel model. Others, such as Vukicevic and Raeder (1994), Langland et al. (2001), and Homar and Stensrud (2003) have applied adjoint sensitivity analyses explicitly to the study of extratropical cyclogenesis through the examination of case studies. Errico and Vukicevic (1991) determined in a case study of a 1982 cyclone that developed due to alpine lee cyclogenesis observed during the Alpine Experiment (ALPEX) campaign that the pressure forecast in the vicinity of the predicted lee cyclone was most sensitive to an upstream, upper-tropospheric ridge-trough pattern. Doyle et al. (2013), in their study of Atlantic extratropical cyclone Xynthia (2010) (a storm whose development was strongly influenced by moist dynamics) have shown that many of the sensitive regions lie within the lower- to mid-troposphere and are most sensitive to fields such as temperature and moisture.

The topic which will be the focus of the present study is understanding how slight changes to initial state vector components of wind and temperature throughout the depth of the troposphere in adjoint-determined sensitive regions, can alter the development of an extratropical cyclogenesis event. This will be accomplished by using the WRF-ARW (Skamarock et al. version 3.8.1) model to simulate an explosively deepening 24-25 October 2010 extratropical cyclone that impacted much of the North American Great Lakes region with high winds and tornadic storms across much of the east-central United States. Additionally, the WRFPLUS package (Zhang et al., 2013) will be used to complete an adjoint-based sensitivity analysis of this event in which perturbations will be calculated based on the regions of sensitivity, inserted into the model, and rerun. The analysis performed will follow the ‘SPRD’ (sensitivity, perturbation, response, diagnoses) technique. Sensitivity fields will be first calculated and examined, followed by perturbations being made within the sensitive regions, the response of the reintegrated simulation to the perturbations noted, and finally a synoptic diagnoses performed between the

modified simulation and a control simulation to determine how perturbations evolve to influence the forecast.

In Chapter 2, a synoptic overview and case comparison of the October 2010 event is presented. Data and methods are described in Chapter 3. Results of the adjoint sensitivity calculations as well as perturbed simulations of the event are presented in Chapter 4. A summary of results and a prospective of future work is given in Chapter 5.

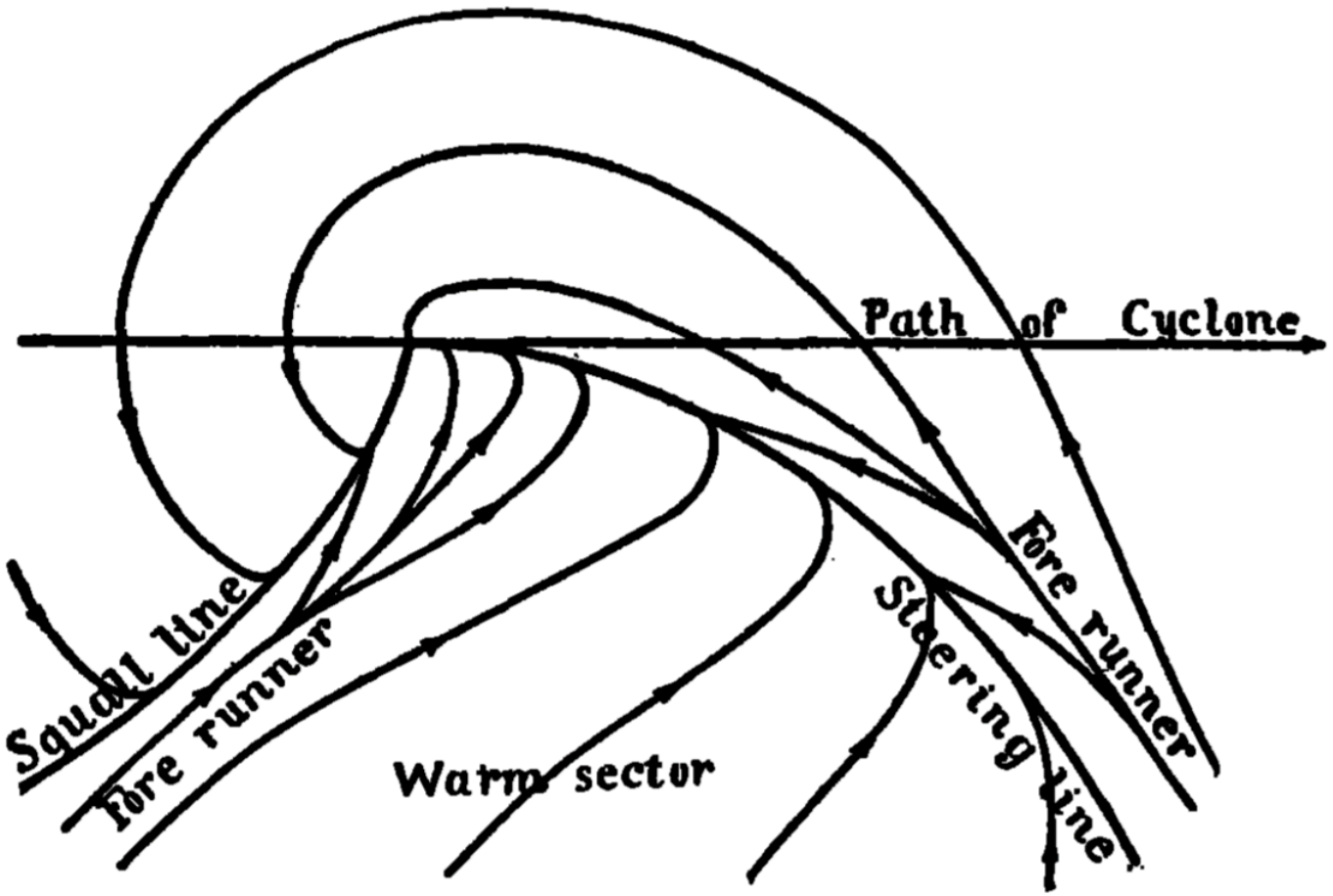

Figure 1.1. J. Bjerknes 1919 diagram depicting air circulations about a cyclone as well as the squall line (cold front), steering line (warm front), the warm sector, and typical cyclone path.

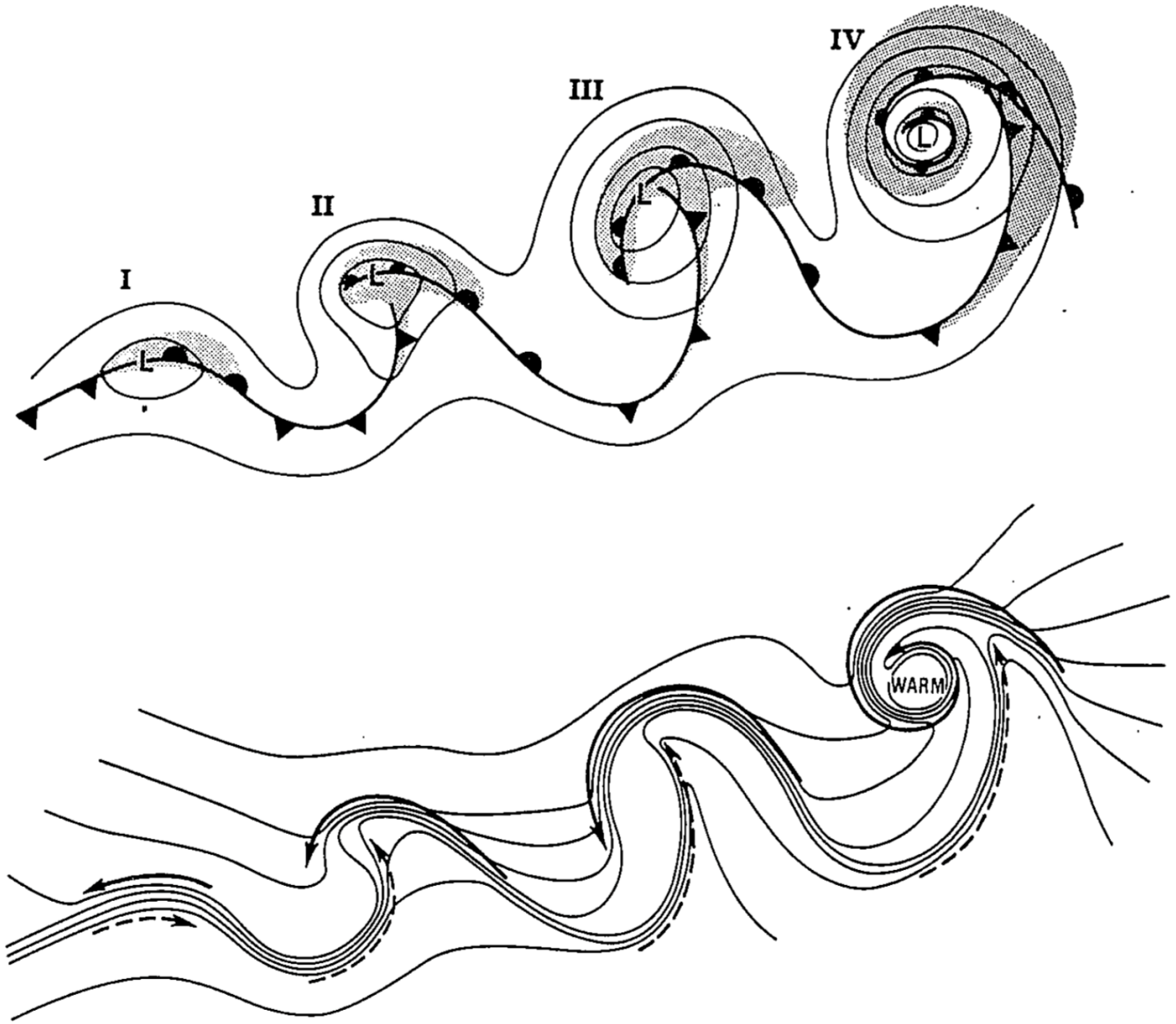

Figure 1.2. Depiction of the four stages of the extratropical cyclone as described by Shapiro and Keyser (Shapiro and Keyser, 1990). (I) incipient frontal cyclone, (II) frontal fracture, (III) bent-back front and frontal T-bone, (IV) warm core frontal seclusion.

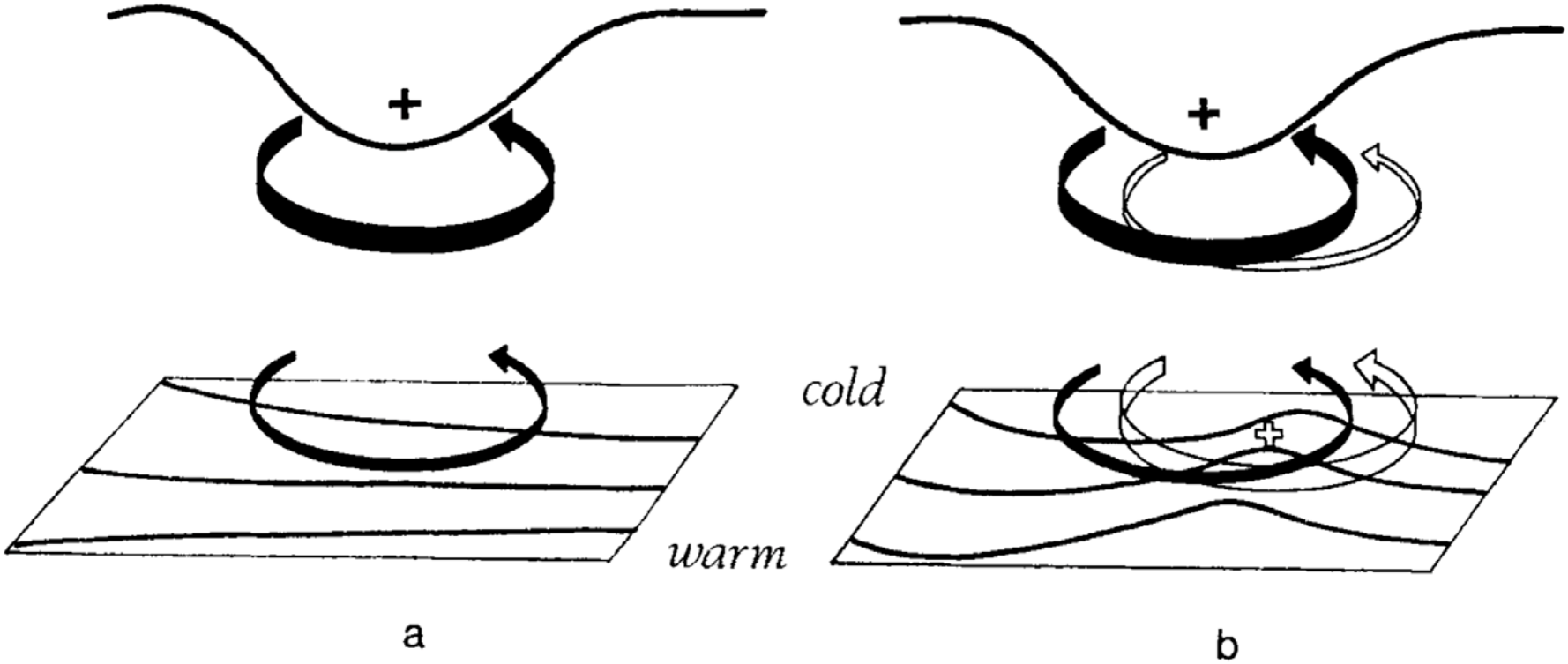

Figure 1.3. Interaction of an upper-tropospheric PV anomaly with a surface baroclinic region as described by Hoskins et al. (1985). (a) the upper level PV anomaly moves over a region of baroclinicity and invokes a 'wrapping' of the isotherms. (b) once a low level warm anomaly at the surface forms slightly ahead of the upper-tropospheric PV anomaly, part of the resultant surface circulation will be projected upon the PV anomaly. This maintains a positive feedback between the upper and lower troposphere and locates the center of the surface cyclone in a region that is ideal for continued development.

Figure 1.4. Schematic borrowed from Mattocks and Bleck (1986) describing a mechanism of alpine lee cyclogenesis. A jet streak propagates across a mountain range while a dome of cold air remains blocked upstream. Ascent associated with the left exit region of the jet is able to carry on unabated as the cold, stable air remains dammed by the mountains.

2. Case Study

The event that will be the focus of this analysis is the 24-26 October 2010 extratropical cyclogenesis event that occurred over North America. This cyclone was centered over the upper Great Lakes region at its peak intensity, but its impacts were felt from Canada to Texas, and from the Rocky Mountains to the US east coast. It reached a minimum sea level pressure (SLP) of 955.2 hPa at 2213 UTC 26 October over northern Minnesota. This SLP was achieved through explosive cyclogenesis, meaning that a developing cyclone deepens at a rate equal to or greater than 24 hPa in 24 hours (Sanders and Gyakum, 1980). There was a total of $18.5 million dollars in damages, most of which resulted from the persistent high winds of this event as well as the multitude of severe weather phenomena including 80 tornadoes, 134 large hail, and 627 high wind reports over the three-day period as recorded by the NOAA Storm Prediction Center. Figure 2.1 shows a GOES-13 visible satellite image taken roughly at 2300 UTC 26 October near the time of maximum intensity.

a) Selection for Case Study

This event has been selected for investigation because many of the dynamics that drove its development are robust and provide strong and clear signals during analysis. This makes it easier to decipher the cyclogenetic precursors and processes that have been most important to its development. Knowing which processes are most critical to the development of a storm of this magnitude may provide insight into whether the same processes are also critical in the transition of a more modest cyclone to one of high impact, especially if there is significant uncertainty in the forecast. This event was well-predicted by the National Centers for Environmental Predictions (NCEP) numerical models and ensemble forecast systems, implying that it will be easy to simulate with high accuracy in a numerical simulation to be used for analysis within the context of this study. Extratropical cyclones that develop explosively have long been of interest due their impacts upon society. Therefore, it is natural to try to better understand the processes critical to their development by applying new methods, such as adjoint sensitivity analysis specifically focused upon upper- to mid-tropospheric dynamics, when possible. By

completing the SPRD analysis on an intense cyclogenesis event such as this, a clear deduction can be made concerning the most critical dynamical processes needed to produce such an event.

b) Synoptic Overview

The synoptic overview begins at 0000 UTC 25 October 2010 (Fig. 2.2) – 48 hours prior to the time at which the cyclone was near peak intensity. The most conspicuous feature at this time is the robust jet at 300 hPa extending from the eastern Pacific into the western United States (Fig. 2.2a). The intensity of this jet appears to be the result of a superposition of the subtropical and polar jet streams that owes its existence, in part, to the presence of Typhoon Megi in the western Pacific several days prior (Wang and Wang, 2013). At 500 hPa (Fig. 2.2b), there is a prominent jet streak/zonally elongated vorticity maximum present on the cyclonic shear side of the jet and beneath the jet's left exit region. This feature will prove to be a critical player in the subsequent cyclogenesis. In the lower-troposphere a broad thermal ridge is centered immediately to the east of the Rocky Mountains, evident in the 850 hPa thermal (Fig. 2.2c) and 1000-to-500 hPa thickness fields (Fig. 2.2d), in response to strong westerly flow over the mountain range. Hydrostatically, there is a broad cyclonic disturbance centered over Montana at both 850 hPa (Fig. 2.2c) and at the surface (Fig. 2.2d). The cyclonic disturbance resembles a nascent cyclone, with its development congruent with the thermal ridge.

By 1200 UTC 25 October (Fig. 2.3), the 300 hPa jet extends into eastern Colorado (Fig. 2.3a) while the 500 hPa vorticity maximum (Fig. 2.3b) has contracted in length and is now located over northern Nevada. A large depression in the 850 hPa height (Fig. 2.3c) and sea level pressure (SLP, Fig. 2.3d) fields occupies much of the Upper Plains coincident with the thermal ridge that has now progressed further to the east, consistent with conceptual models of cyclogenesis in the lee of the Rocky Mountains (Carlson, 1961; Steenburgh and Mass, 1994).

At 1800 UTC 25 October two circulation centers, one to the north over the Dakotas, and one to the south over Kansas, become evident within the broader cyclonic circulation of the developing cyclone (Fig. 2.4d). The development of the northern feature begins to slow as the upper-tropospheric PV anomaly that is associated with the jet exit region and located directly upshear of the surface warm anomaly between 350 and 450 hPa has now shifted slightly to the south and out of phase (not shown). As the jet exit region continues to dig south the vorticity

anomaly at 500 hPa associated with the deepening trough also moves south and can be observed over Utah at this time (Fig. 2.4b).

A shift in the 500 hPa vorticity anomaly, a bullseye of which is located upshear of the southern surface depression, can be noted (Fig. 2.4b). Paired with a strong region of baroclinicity near the surface that stretches from southwest Nebraska through the four corners region (Fig. 2.4d), it can be confirmed that Type-B cyclogenesis is responsible for the development of the southern cyclone. Diffluent flow aloft across the majority of the central U.S. in association with the exit region of the jet and shortwave trough at 300 hPa (Fig. 2.4a) indicates the enhancement of development due to lee cyclogenesis. It has been determined by Chung et al. (1976) that one of the most critical features needed for lee cyclogenesis is a diffluent flow across a mountain barrier in the mid-troposphere. Mattocks and Bleck (1986) have also found that the presence of a jet streak, as well as a deformation of a low level baroclinic region, were critical. As air parcels pass adiabatically over the high terrain of Colorado, their vertical depth is forced to become more compact as isentropic surfaces are forced to become more stratified vertically as they follow the terrain. Once in lee of the Colorado Front Range, the isentropic surfaces are allowed to become less vertically stratified. Any air parcel moving adiabatically will be forced to stretch vertically. In accordance with the stretching term of the vorticity equation, this vertical stretching will produce cyclonic vorticity within the column. It has been determined by McGinley (1982) that strong vertical stretching within the mid-troposphere and strong positive vorticity advection aloft, in lee of an orographic barrier and in the vicinity of a pre-existent baroclinic region, are some of the primary processes necessary for rapid growth. McGinley (1982) also determined that lee cyclones that develop in this fashion are closely related to Petterssen Type-B cyclones with their upshear tilted vertical structure. In the case of this event, it is likely that both Petterssen Type-B development and lee cyclogenesis, as described above, were major factors in contributing to the explosive development of this storm.

By 0000 UTC 26 October, the southern surface depression has advanced to the northeast where it has merged into the larger, broad circulation associated with the northern depression as seen in the SLP field (Fig. 2.5d). An examination of 925 hPa relative vorticity (Fig. 2.5c) shows that the two cyclones are still discernable by their respective lower-tropospheric vorticity signatures. It is important to note that the southern cyclone is propagating more rapidly to the northeast than the northern cyclone is advancing eastward. It will be seen that the explosive

development of the system begins with the southern feature before merging with the northern feature. After merger occurs, explosive development continues at approximately 1.24 hPa/hour (NOAA). A broad cold front can be seen draped across western Iowa through New Mexico (Fig. 2.5d), which will be the key feature in initiating the severe weather associated with this event as it moves across a warm sector that contains temperatures in the mid to upper 20s Celsius, as well as dew points of about 16-18°C. A broad warm front can be discerned from the thickness and SLP field (Fig. 2.5d) that stretches from the upper Great Lakes to Maine. The surface cyclone at this time maintains an ideal location to continue development. There is a 350 to 450 hPa PV anomaly (Fig. 2.6) and associated tropopause fold near the jet exit region directly upshear of the surface cyclone. There is also persistent diffluence in the flow at 300 hPa (Fig. 2.5a) which is helpful for the evacuation of mass over the surface cyclone (Palmén and Newton, 1969). Within the mid-troposphere, it can be seen at 500 hPa (Fig. 2.5b) that there is a significant relative vorticity still upshear of the cyclone as well as a shortwave trough/ridge feature that is beginning to become more apparent in the flow. The cyclone is located downshear of the trough axis, in a region of high baroclinicity at the surface and large horizontal divergence aloft. This divergence results from the divergence of the ageostrophic winds downstream of the trough axis and upstream of the ridge axis. The ageostrophic winds are resultant from accelerations in the flow that are needed to bend the geostrophic wind around curvature present in the geostrophic height field. Ageostrophic winds slow the flow in the base of a trough and speed it up in the peak of a ridge, therefore creating a broad region of horizontal divergence aloft and subsequently, broad ascent which is conducive for cyclogenesis (Martin, 2006).

By 1200 UTC 26 October a well-defined and much more compact cyclone center has formed over Minnesota and Wisconsin as the two surface cyclones have merged (Fig. 2.7d). This merger can also be noted in the 925 hPa vorticity field (Fig. 2.7c). The 925 hPa vorticity field also depicts very well the circulation associated with the cold front. Rapid intensification continues at this time due to the processes discussed in the previous paragraphs.

The cyclone is slightly beyond peak intensity at 0000 UTC 27 October with a SLP value of 957.73 hPa. It can be seen that the low level thermal field is well-wrapped around the cyclone center and occluded at this time (Fig. 2.8c and 2.8d). The cyclonic circulation is cut off from the larger-scale flow all the way up to 300 hPa (Fig 2.8a and 2.8b). With the cyclone now being isolated from synoptic-scale forcing, it begins cyclolysis as it continues to propagate to the east-

northeast toward Greenland. Most of the vorticity present at mid- to upper-tropospheric levels has been thoroughly wrapped into the center of the cyclone due to its strong circulation (Fig. 2.8b).

c) Historical Comparison

As a historical comparison to the October 2010 event presented above, a brief overview is given of the 25-26 January 1978 'Cleveland Superbomb'. Figure 2.9 is an infrared satellite image of the storm near its peak intensity. This event achieved a low pressure of 955.5 hPa through explosive cyclogenesis and was the third strongest north American cyclone of non-tropical origins on record until the October 2010 event took that distinction (Gerhardt, 2011). It produced three feet of snow throughout much of the U.S. Midwest with wind gusts up to 85 knots (TIME, 2011). The Cleveland Superbomb was the result of the merger of two distinct surface depressions. The southern feature was advected by the mean flow to merge with an existent northern feature. The two surface depressions in this event are more clearly defined as separate entities than in the 2010 case. This is due to the merger of two 500 hPa waves and their associated vorticity anomalies whereas in the 2010 case, the same upper-tropospheric PV anomaly associated with the jet exit region was responsible for the initiation of both of the cyclones as it gradually migrated south along the eastern fringe of the Rocky Mountains. Figure 2.10, adapted from Hakim et al. (1995), illustrates the evolution of the 500 hPa quasi-geostrophic potential vorticity (QGPV) anomalies associated with the Cleveland Superbomb in 24 hour increments from 0000 UTC 24 January through 0000 UTC 27 January. It can be seen that one of the PV anomalies, labeled 'A/B', moves across the southwest U.S., while the other, labeled 'C', moves from the polar regions south across Saskatchewan and into the upper Midwest. Much like the 2010 case, the southern feature 'A/B' is the more important feature in driving the explosive development of the system. The Cleveland Superbomb case helps to illustrate the importance of understanding the dynamics that have driven the development and merger of the two surface cyclones in the case under investigation in this paper. The findings in the current study will be able to be applied to studies of similar high impact events where the merger of upper- to mid-tropospheric features, as well as surface circulations, are critical to rapid development.

A study of wave merger phenomena as described by Gaza and Bosart (1990) indicates such events are generally confined to an area over the North American continent that is east of 100°W longitude and north of 35°N latitude. It was also found that out of the 21 cases studied, 14 resulted in explosive cyclogenesis. While the 2010 event was not a product of a 500 hPa wave merger event, the merger of two low level vorticity signatures produced through Type-B and lee cyclogenesis are present and critical to the strength of this storm. It has been indicated in Gaza and Bosart (1990) that the presence of a northern and southern circulation act to advect cold air present behind the northern cyclone southward. At the same time the southern cyclone acts to advect warm, moist air poleward ahead of the system. This process works to increase the baroclinicity in the vicinity of the two systems and thereby condition the environment for explosive cyclogenesis upon merger of the two features.

Climatologically, intense extratropical cyclones such as the 2010 event and other strong gales of the Great Lakes occur primarily during the autumn (Whittaker and Horn, 1984). This is a transition period in which temperature gradients throughout the extratropics are maximized. It has been shown that during La Niña, a stronger storm track across the Midwest and Great Lakes region is produced (Eichler and Higgins 2005). Based on data provided by the NOAA Climate Prediction Center, an Oceanic Niño Index (ONI) of -1.7 (a La Niña regime) was found in the Niño 3.4 region of the equatorial Pacific for the months of September, October, November (SON) 2010. The ONI is based on a threshold value of a +/- 0.5°C sea surface temperature to qualify an event as either El Niño or La Niña. The Rossby wave train generally forms a ridge in the north Pacific during La Niña. This is primarily due to the enhanced convection in the equatorial west pacific (Kiladis and Weickmann, 1992). The enhanced convection effectively injects low PV air into the upper-troposphere forcing the ridge over the north Pacific further poleward and eastward. This climatological regime, paired with the outflow of Typhoon Megi as touched upon earlier, were likely instrumental in setting up the observed upper-tropospheric flow pattern. The large ridge over the northern Pacific, subsequent trough downstream over the western U.S., and superimposed polar and subtropical jet streams owe their development to these processes. These aspects of the larger-scale general circulation were critical to the formation of the robust upper-front necessary for the initiation and development of the 2010 event.

It has also been determined that a 500 hPa trough that is able to sharpen (i.e. reduce its zonal length scale and become deeper along its axis) and transition from a positive to negative barotropic tilt, relative to the horizontal shear present in an intense upper-tropospheric jet, is more advantageous in realizing strong extratropical cyclogenesis than any other orientation (Gaza and Bosart, 1990; Lagouvardos et al., 2007). An increasingly negative barotropic tilt allows for the enhancement of cyclonic relative vorticity and subsequently positive vorticity advection (PVA) downstream. It also helps create divergence downstream of the trough axis, together this is ideal for cyclonic development.

It has been discussed in the preceding paragraphs which features of the atmosphere have been most critical to the explosive development of the October 2010 case. An overview of these dynamical precursors and *how* they force rapid development was also touched upon. It is important to present these processes here as an investigation of how they have been modified by adjoint informed perturbations to the model initial state vector prior to reintegration of the WRF-ARW will be closely examined in the following chapters.

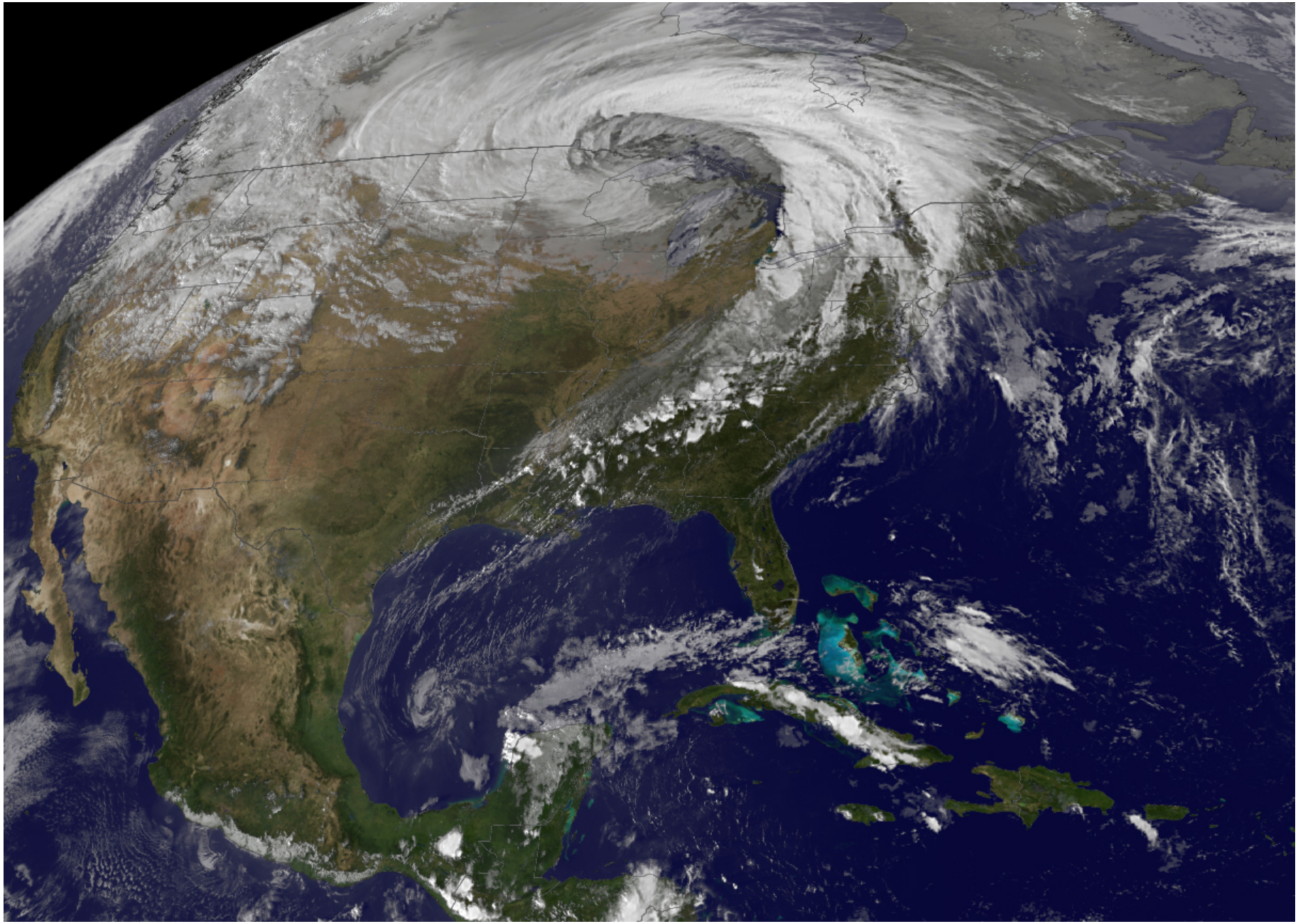

Figure 2.1. GOES-13 satellite image 2300 UTC 26 October showing the cyclone near peak intensity.

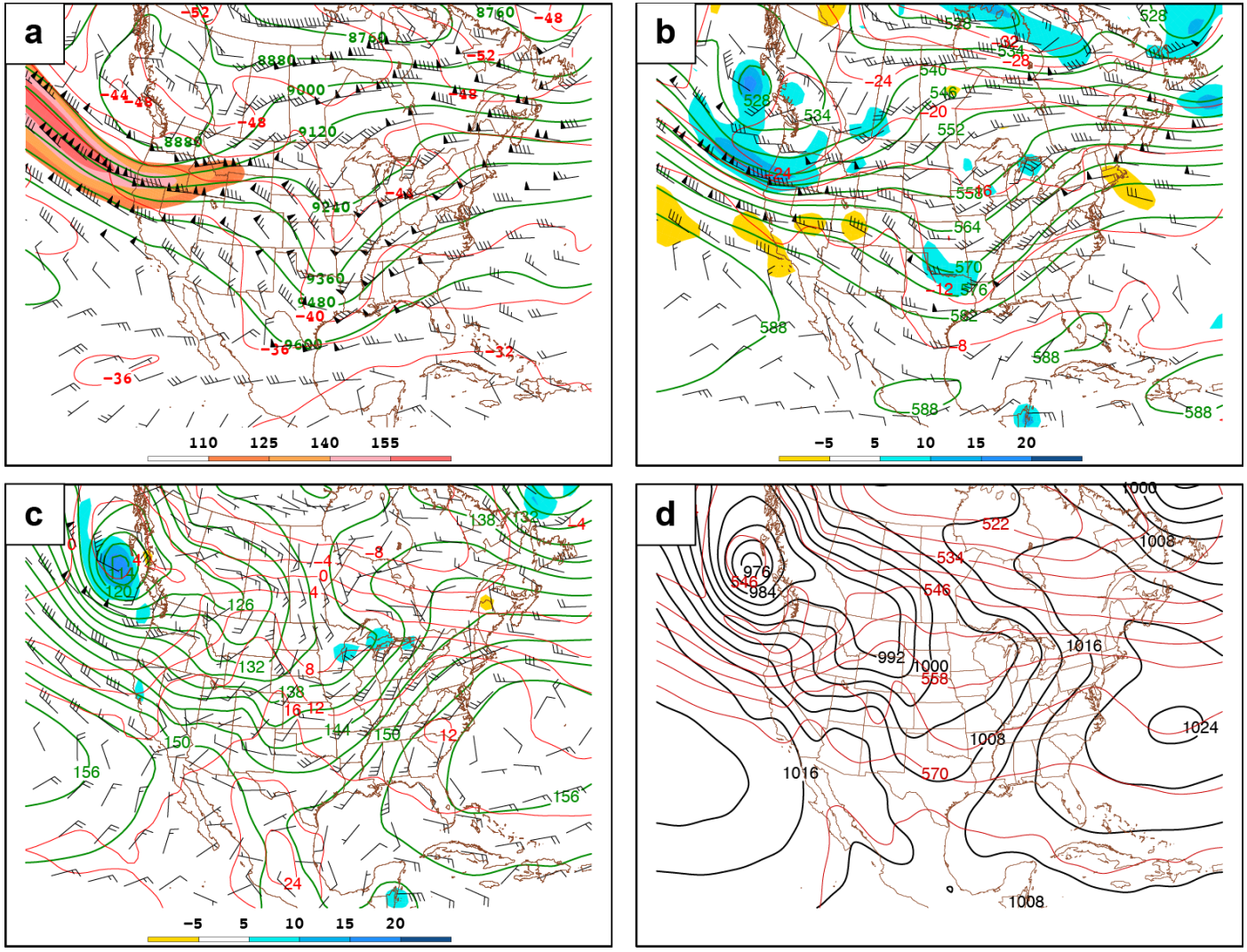

Figure 2.2. Synoptic charts for 0000 UTC 25 October 2010 produced from NCEP analysis data: (a) 300 hPa geopotential height (green contours, interval 120 m), temperature (red contours, interval 4°C), wind (barbs, knots), and isotachs (fill, interval 15 knots above 110 knots); (b) 500 hPa geopotential height (green contours, interval 60 m), temperature (red contours, interval 4°C), wind (barbs, knots), relative vorticity (blue fill, positive beginning at $5x10^{-5}s^{-1}$; gold fill, negative beginning at $-5x10^{-5}s^{-1}$, interval $2x10^{-5}s^{-1}$); (c) 850 hPa geopotential height (green contours, interval 30 m), temperature (red contours, interval 4°C), wind (barbs, knots), and 925 hPa relative vorticity (blue fill, positive beginning at $5x10^{-5}s^{-1}$; gold fill, negative beginning at $-5x10^{-5}s^{-1}$, interval $2x10^{-5}s^{-1}$); (d) SLP (black contours, interval 4 hPa), 1000-to-500 hPa thickness (red contours, interval 60 m), and 10m wind (barbs, knots).

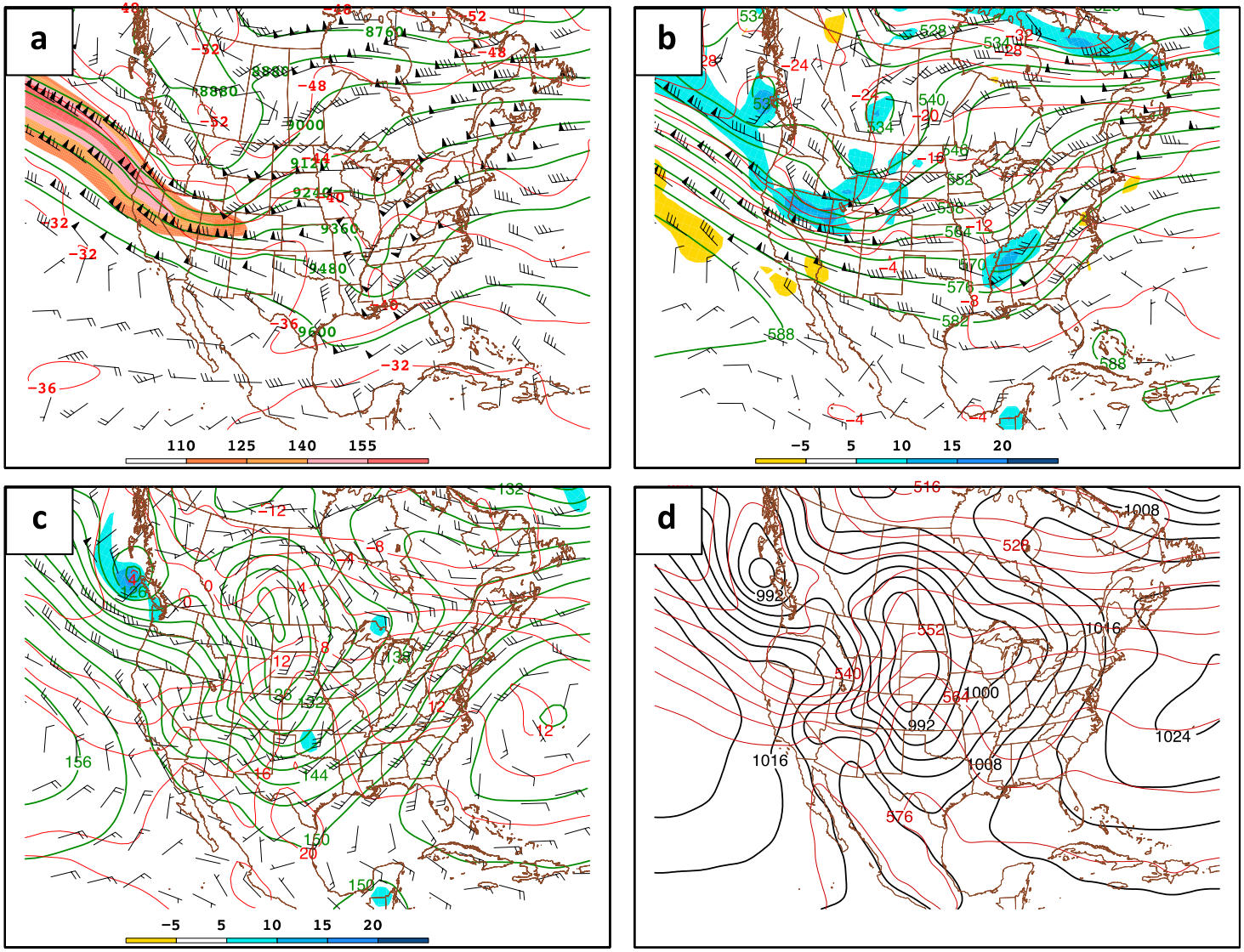

Figure 2.3. As in Fig 2, except for 1200 UTC 25 October 2010

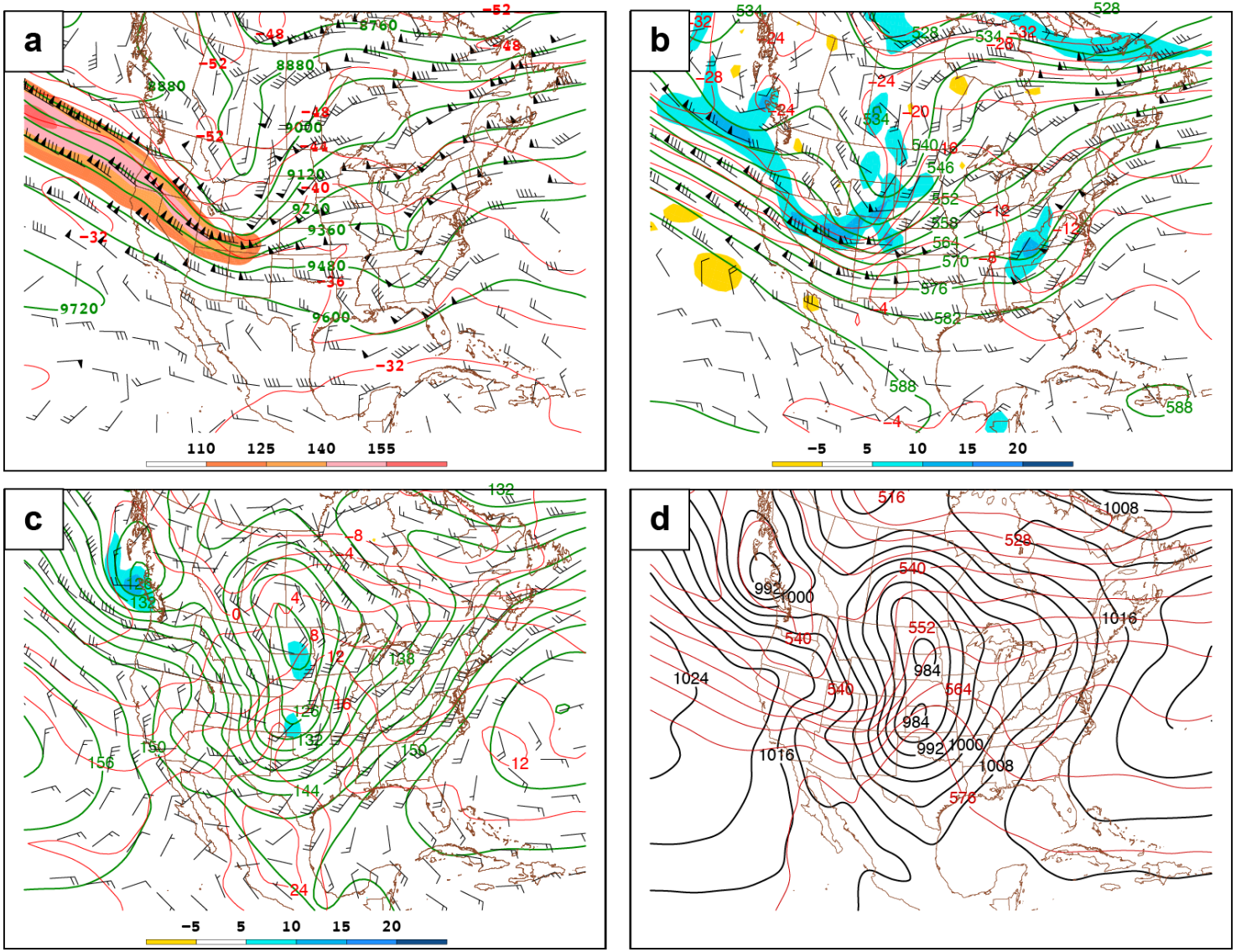

Figure 2.4. As in Fig 2, except for 1800 UTC 25 October 2010

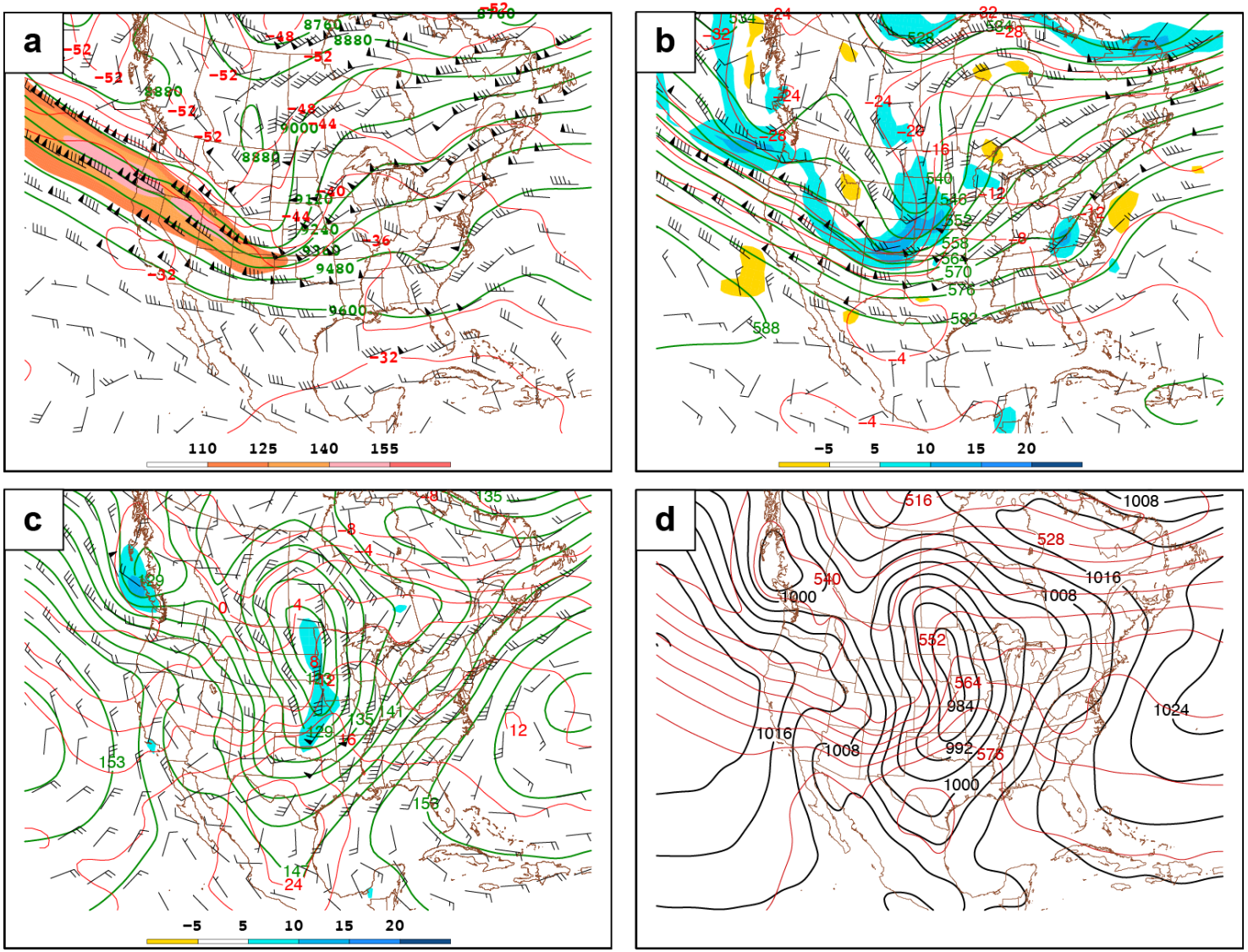

Figure 2.5. As in Fig 2, except for 0000 UTC 26 October 2010

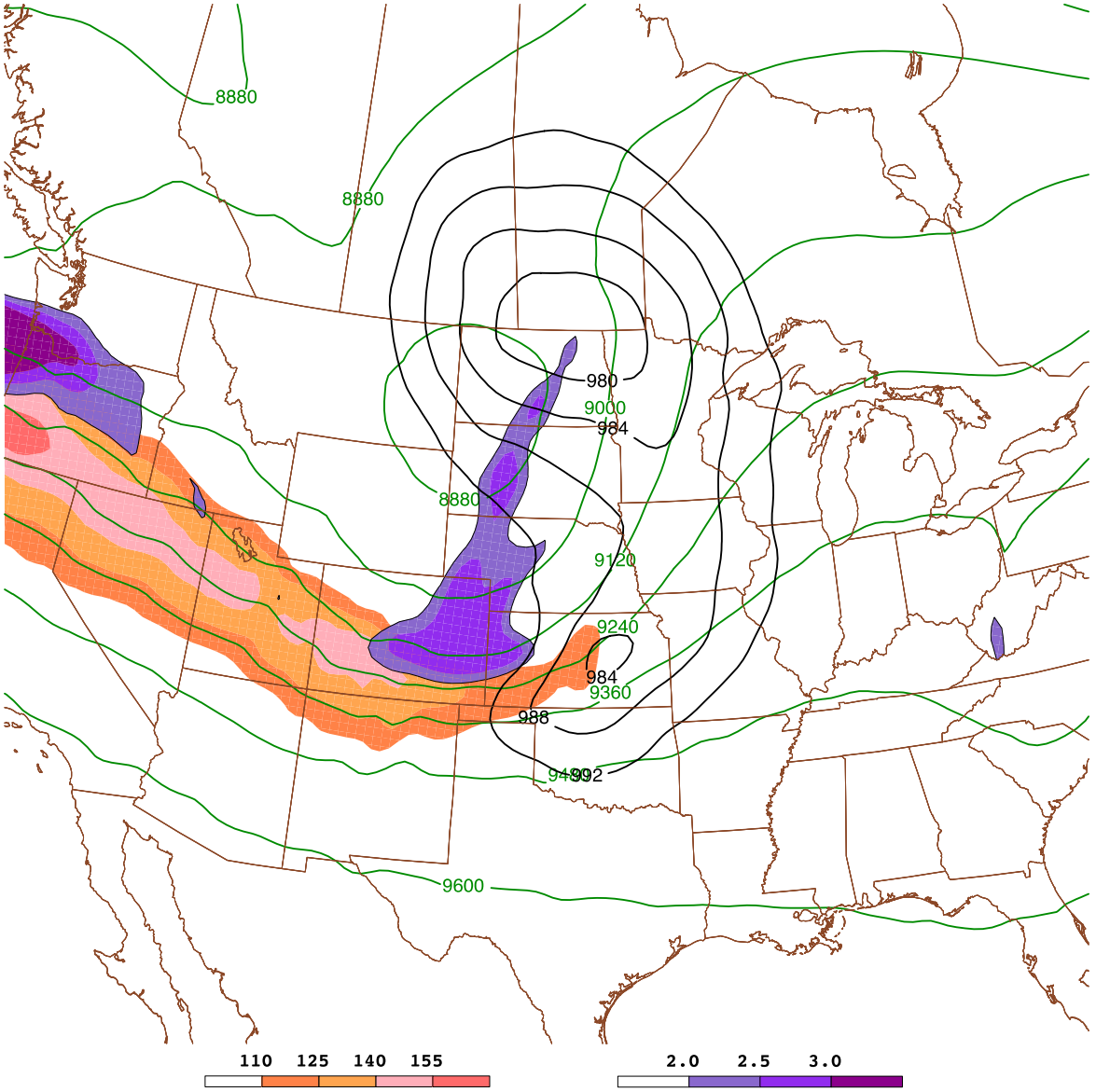

Figure 2.6. 0000 UTC 26 October synoptic chart produced from NCEP analysis data. 350 to 450 hPa layer PV (purple fill, beginning at $2x10^{-5}s^{-1}$, interval $0.5x10^{-5}s^{-1}$), 300 hPa geopotential height (green contours, interval 120 m), 300 hPa isotachs (peach fill, interval 15 knots above 110 knots), and sea level pressure (black contours, interval 4 hPa lower than 992 hPa).

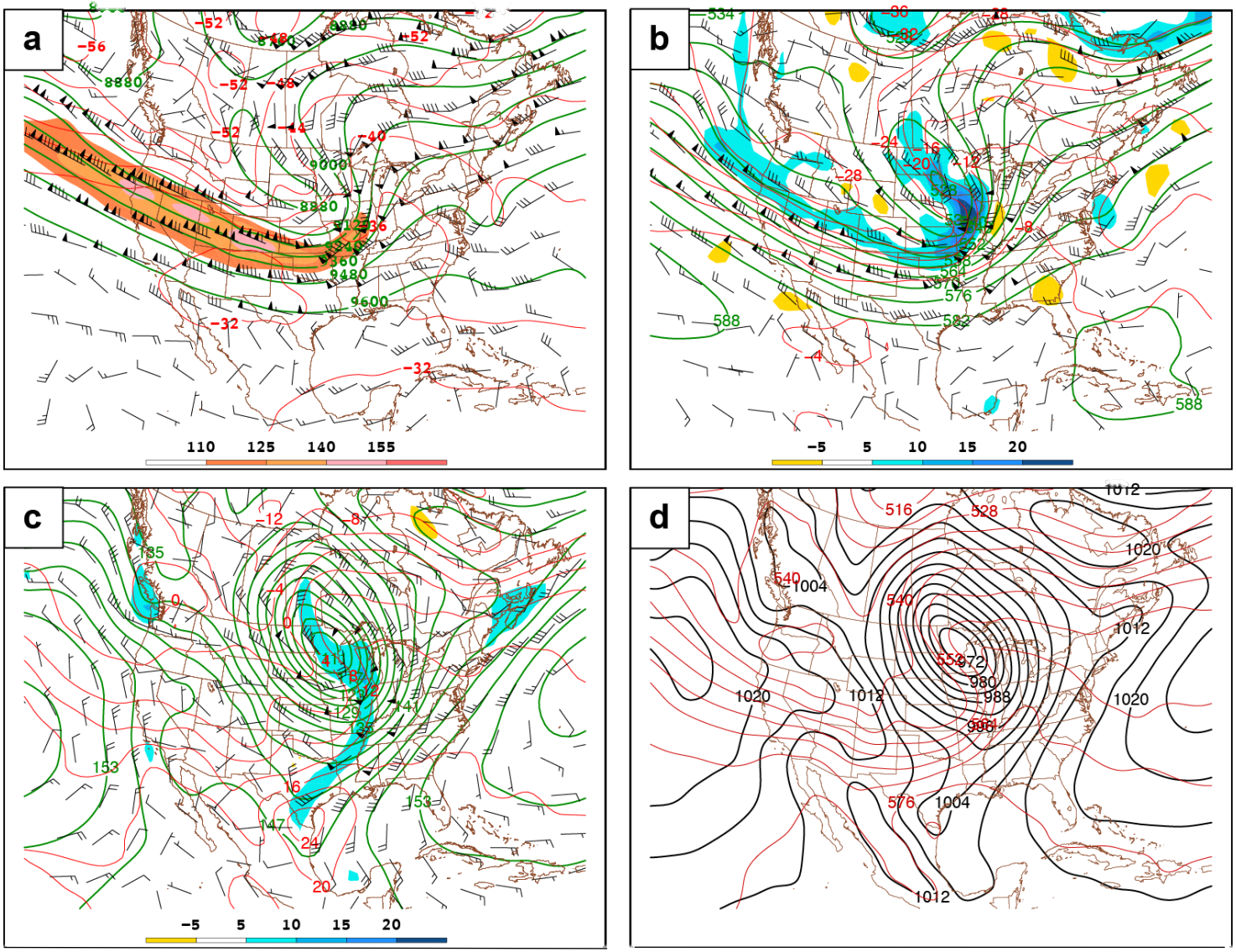

Figure 2.7. As in Fig 2, except for 1200 UTC 26 October 2010

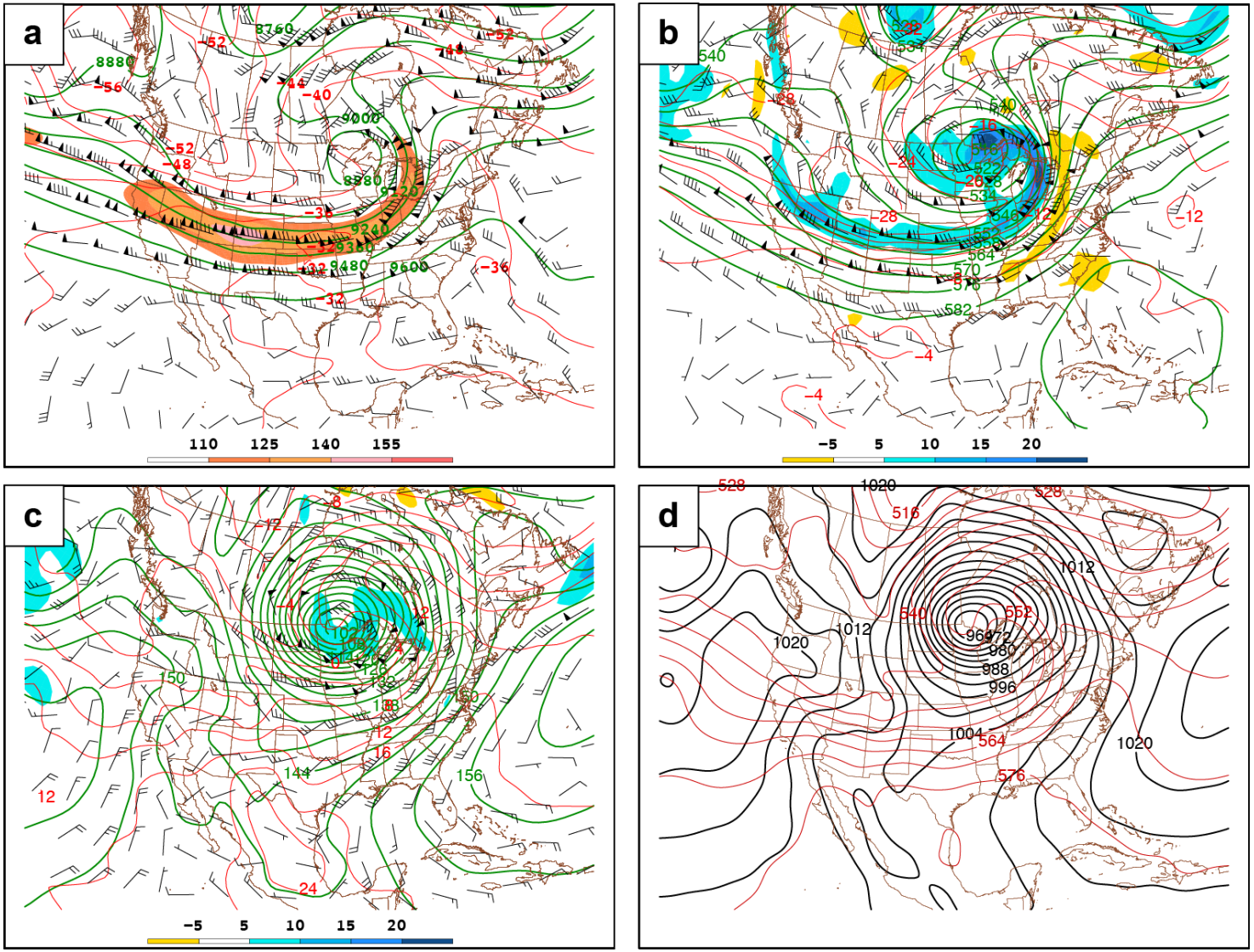

Figure 2.8. As in Fig 2, except for 0000 UTC 27 October 2010

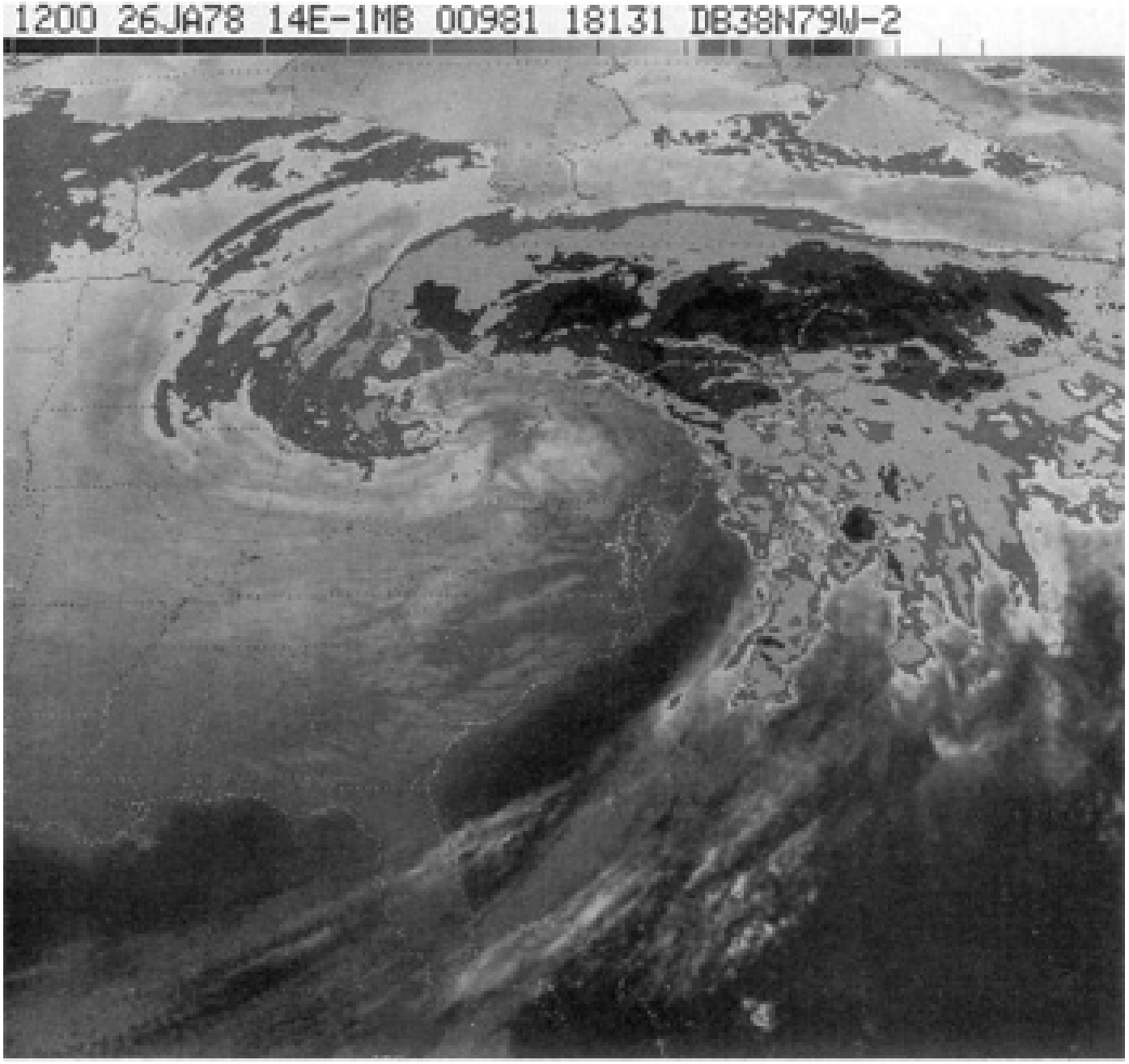

Figure 2.9. 1200 UTC 26 January 1978 infrared satellite image of the Cleveland Superbomb near peak intensity.

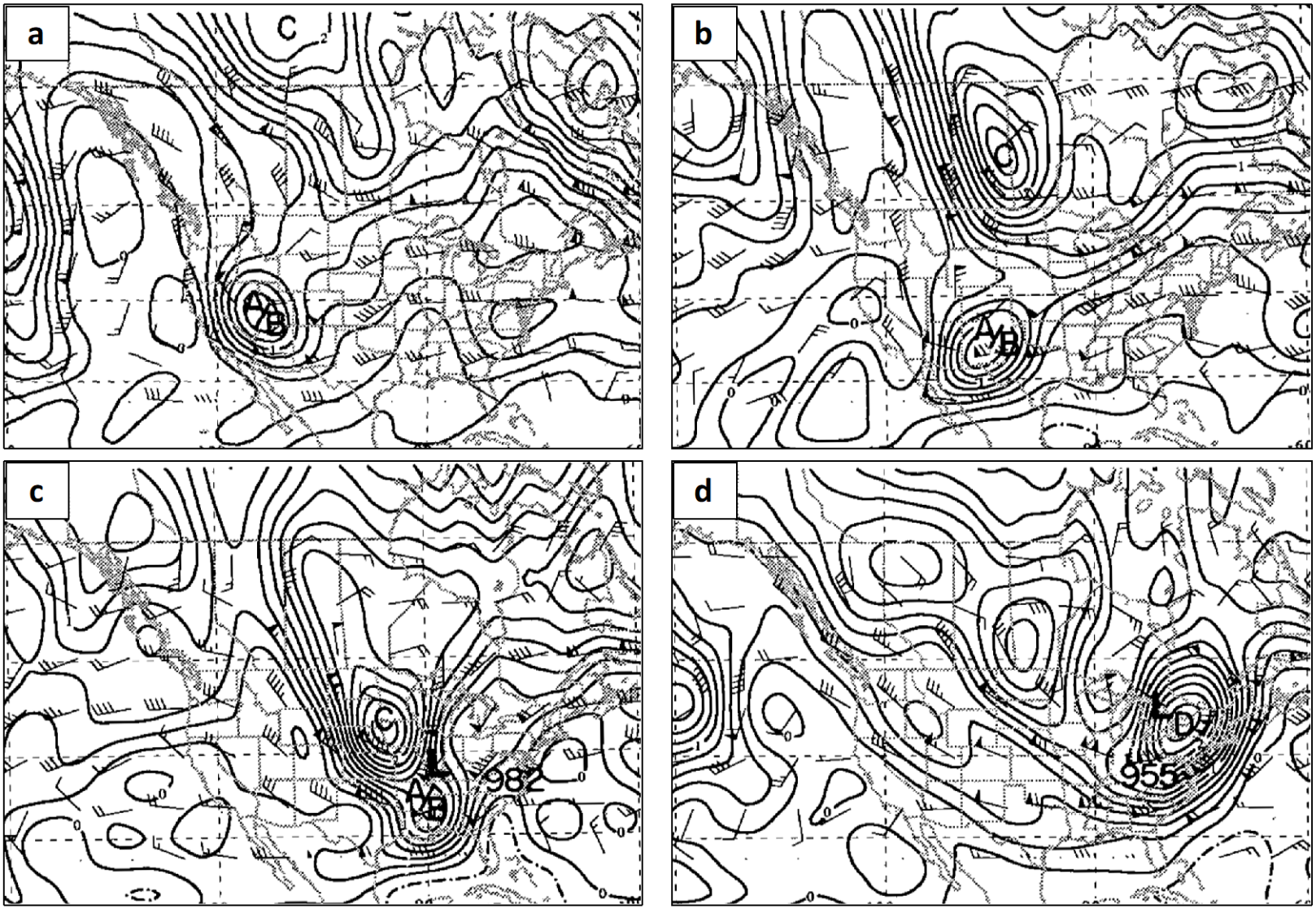

Figure 2.10. Synoptic charts adapted from Hakim et al. (1995) for 0000 UTC 24 January 1978 thru 0000 UTC 27 January 1978: (a) 0000 UTC 24 Jan. 500 hPa Quasi-geostrophic potential vorticity ((QGPV) contoured every 0.2 PVU), geostrophic wind barbs (with a half barb, full barb, and flag representing 2.5, 5, and 25 m s^{-1}). Precursor QGPV disturbances are labeled A/B and C; (b) Same as in (a) except for 0000 UTC 25 Jan.; (c) Same as in (a) except for 0000 UTC 26 Jan. and where **L** represents the surface cyclone; (d) Same as in (c) except for 0000 UTC 27 Jan. and where D represents the now merged precursor disturbances A/B and C.

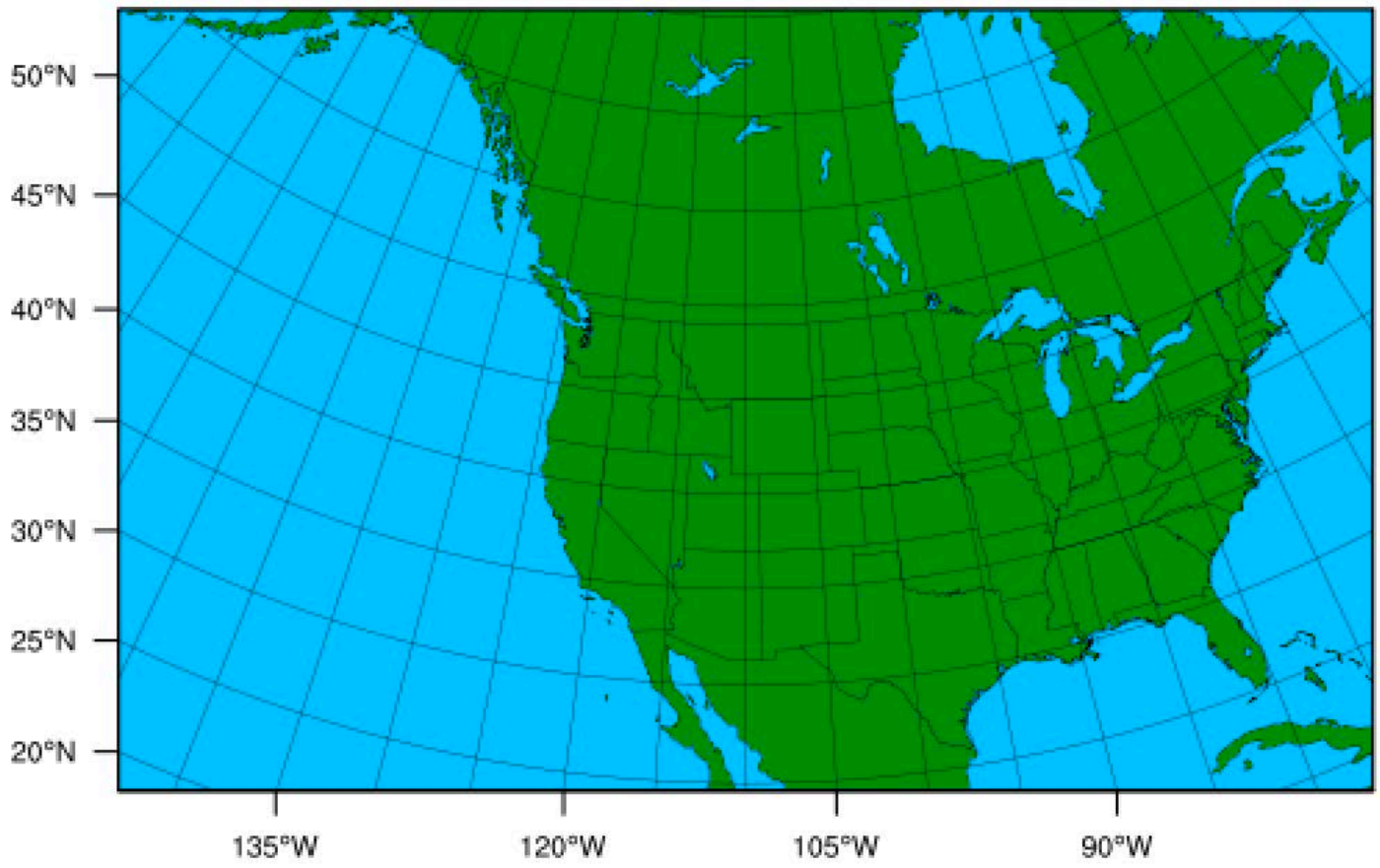

Figure 3.1. Horizontal extent of the domain used in the WRF forward and adjoint model integrations.

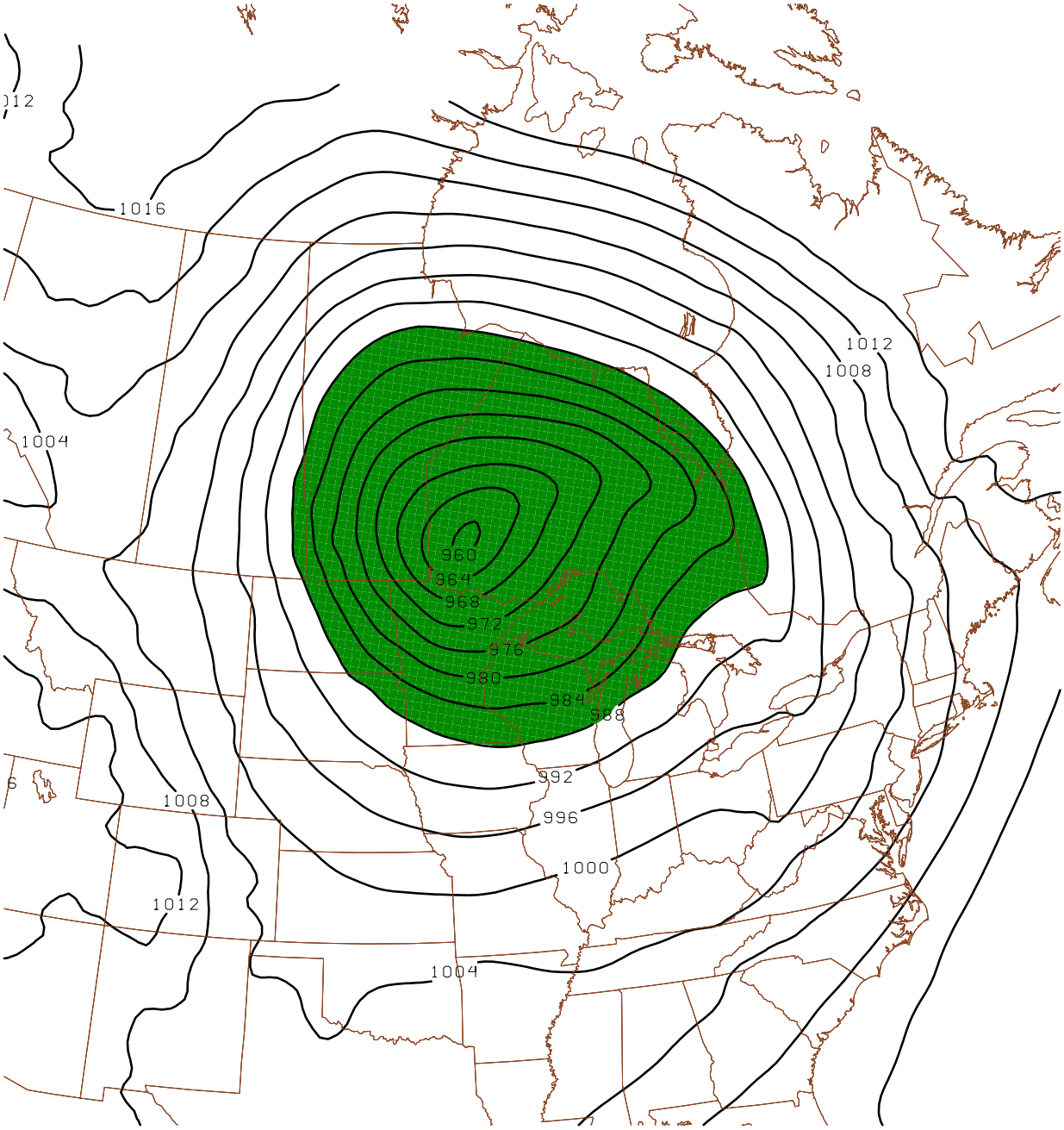

Figure 3.2. Region over which the response function is defined (green fill) and WRF control simulation sea level pressure (black contours, interval 4 hPa). The response function is the (perturbation) dry mass of the atmospheric column as measured at the surface and averaged over the area in which it is defined.

3. Data and Methods

The Weather Research and Forecasting (WRF) model (Skamarock et al. 2008) and its adjoint (Zhang et al. 2013) available in WRFPLUS (version 3.8.1) are used to simulate the event under investigation. The WRF simulations are initialized using the National Center for Environmental Prediction (NCEP) FNL (Final) operational global analyses on 1° x 1° grids available from the National Center for Atmospheric Research (NCAR) Research Data archive as dataset ds083[1]. The analyses, an optimal blend of Global Data Assimilation System (GDAS) model first-guess and observational data taken primarily from the Global Telecommunications System (GTS), are nearly the same as those used by NCEP to initialize the Global Forecast System (GFS). The one key difference between these analyses and those used to initialize the GFS are that these "final analyses" are derived in an assimilation cycle delayed to incorporate additional data into NCEP's analysis and forecast cycle. These analyses also include variables at the surface, below the surface, and at 26 mandatory levels from 1000 hPa to 10 hPa.

a) WRF-ARW and WRFPLUS Configurations

The WRF-ARW version 3.8.1 and its adjoint, WRFPLUS, are used in the simulation of the October 2010 event. The WRF-ARW is a nonlinear, non-hydrostatic, full-physics NWP model that can be run in multiple configurations for idealized cases or for "real data" simulations for case studies or real-time forecasts. The WRFPLUS includes both the forward and adjoint versions of WRF-ARW. The adjoint has the capability of being run in a stand-alone mode to produce sensitivity gradients for a chosen response function with respect to the model state at an earlier time, or as part of the WRF 4D-variational data assimilation system (through WRFDA) to minimize the distance between the model state and observations at the time in which the observations appear in the assimilation time-window. In the context of this study, it is being used as a stand-alone system in conjunction with WRF-ARW. A 48-hour WRF-ARW integration is

[1] National Centers for Environmental Prediction/National Weather Service/NOAA/U.S. Department of Commerce, 2000: NCEP FNL Operational Model Global Tropospheric Analyses, continuing from July 1999. Research Data Archive at the National Center for Atmospheric Research, Computational and Information Systems Laboratory, Boulder, CO. [Available online at https://doi.org/10.5065/D6M043C6]

produced beginning 0000 UTC 25 October and ending 0000 UTC 27 October. Integration of the model is completed using a 90 second time step over a domain with a horizontal extent that stretches from the Aleutian Islands in the northwest to Jamaica in the southeast (Fig. 3.1). The domain has a 30km horizontal grid spacing centered at 45°N and 110°W using a Lambert conic conformal projection with 42 equally spaced vertical eta levels. The model state is archived at every time-step to establish the nonlinear trajectory around which the WRF adjoint model is linearized. The WRF adjoint is integrated backward from 0000 UTC 27 October to 0000 UTC 25 October using the same grid spacing and vertical levels as WRF-ARW to produce sensitivity gradients of the response function with respect to the initial model state.

b) Response Function

The response function used in this study makes use of the WRF model variable, $\mu = p_s - p_{top}$, defined as the dry mass of a column of the atmosphere as measured at the surface. Since the top of the model is fixed at 50 hPa, any changes apparent in this measurement are a result of the addition or loss of mass somewhere in the column below 50 hPa and will be manifest as a change in surface pressure. As a consequence, this metric can be taken as a proxy for SLP. The response function, *R*, is defined to be equal to *minus* μ *integrated over an area surrounding the cyclone center*:

$$R = -\overline{\mu}. \tag{1}$$

The minus sign is chosen so that a decrease in column mass (surface pressure) is realized as an increase in both cyclone intensity *and* the response function: as *R* increases, the intensity of the cyclone increases, and μ decreases. The area defining *R* is taken within the region encompassed by the 988 hPa SLP contour at the final (48-hour) forecast time (Fig. 3.2).

c) Adjoint Sensitivity Analysis

Adjoint sensitivity analysis applied to numerical weather prediction (NWP) models involves the objective evaluation of the sensitivity of an aspect or feature of interest from that model (called a *response function, R*) to (changes in) the model's forecast trajectory (including

its initial state and boundary conditions). The adjoint of an NWP model allows for the efficient calculation of this sensitivity that is described by the gradient, $\partial R/\partial \mathbf{x}$ (Errico 1997). A brief description of an adjoint model and its relationship to the nonlinear forecast model follows.

A nonlinear NWP model can be represented as a function (M) that evolves an initial model state ($\mathbf{x}_0$, i.e., the initial conditions) forward in time to a model forecast state, $\mathbf{x}_f$ through solving a nonlinear system of prognostic equations for the state:

$$\mathbf{x}_f = M(\mathbf{x}_0). \tag{2}$$

The model output at the final forecast time, $\mathbf{x}_f$, can be used to define the response function, $R = R(\mathbf{x}_f)$. The nonlinear model (NLM) linearized about a specific forecast trajectory, is called the tangent linear model (TLM). The TLM can be represented by a matrix, $\mathbf{L}$, called the propagator matrix and is used to propagate an initial condition perturbation, $\mathbf{x}'_0$, forward in time to a final forecast state, $\mathbf{x}'_f$ by linearizing the system of prognostic equations about a state defined by the NLM trajectory:

$$\mathbf{x}'_f = \mathbf{L}\mathbf{x}'_0. \tag{3}$$

Mathematically, the adjoint of a linear operator (that may be represented as a matrix) is the transpose of that matrix. The adjoint operator, $\mathbf{L}^{\mathrm{T}}$, propagates the sensitivity of R with respect to the final-time forecast state, $\partial R/\partial \mathbf{x}_f$, backward in time to yield the sensitivity with respect to the initial state, $\partial R/\partial \mathbf{x}_0$:

$$\frac{\partial R}{\partial \mathbf{x}_0} = \mathbf{L}^{\mathrm{T}} \frac{\partial R}{\partial \mathbf{x}_f}. \tag{4}$$

The gradient, $\partial R/\partial \mathbf{x}_0$, is the sensitivity gradient at the initial forecast time and quantifies how the response function (at the final time) would change for perturbations to the model initial state.

Due to the linearization of the adjoint, highly nonlinear processes, such as diabatic heating, must be 'switched' on or off in the model according to the state of the model atmosphere. As a consequence, it can be difficult for adjoint models to accurately diagnose forecast sensitivities for forecast trajectories with regions of intense convection, as there is no

gradient in the on/off processes. This makes adjoint analysis more ideal for dynamical studies as it has been shown that the evolution of linear solutions of perturbations in the TLM generally match that of the nonlinear evolution in the NLM except in regions where there are parameterized moist processes (Vukićević and Errico, 1993). Most modern adjoints have become sophisticated enough that moist processes are at least represented in the large scale, and sometimes at the convective scale (Holdaway et al., 2014), and lead to significant decreases in forecast error as shown in different case studies explicitly examining moisture processes (Jung and Kim, 2009; Doyle et al., 2013). The linear processes of the adjoint are likely to stray from the nonlinear trajectory to some degree. It has been determined in a comparison of a NLM with a forward tangent linear model (TLM), that in order for the TLM to remain accurate with the NLM, its integration should not exceed 72 hours (Errico et al., 1993).

d) Perturbations

As indicated above, adjoint sensitivities indicate regions where slight perturbations to the initial conditions of a NWP model will have the largest impact in changing an outcome of a NWP forecast as measured by a response function. In this study, two types of perturbations are considered: perturbations that are proportional to the sensitivity gradients with no constraints (referred to as "non-optimal" perturbations), or perturbations intentionally designed to minimize initial perturbation energy to yield a prescribed change in the response function, δR (hereafter referred to as "optimal perturbations"). Both types of perturbations are considered as the non-optimal perturbations are perturbations that are designed to be reflective of the error threshold for observations taken at their respective vertical levels of the atmosphere. The goal of this is to see what sort of response in cyclone development occurs if discrepancies in the observations appear within sensitive regions of the atmosphere. Optimal perturbations are *designed* to produce a specific response function change at the final forecast time. This enables an investigation as to *how drastically* the atmosphere must be modified as well as the most effective means dynamically of producing the ascribed change in the response function.

1) NON-OPTIMAL PERTURBATIONS

The vector $\mathbf{x}_0' = \left(\mathbf{u}', \mathbf{v}', \mathbf{T}', \mathbf{q}_v', \mathbf{p}'\right)$ represents perturbations of the horizontal components of the wind, the temperature, the water vapor mixing ratio, and the perturbation pressure. For a non-optimal perturbation, these perturbations are calculated from a simple scaling of the sensitivity gradient at the time and region of interest (in this case the initial forecast time within and directly below the jet). So, $\mathbf{x}_0' = \alpha \dfrac{\partial R}{\partial \mathbf{x}_0}$ where α is a scaling factor used to create perturbations of a particular magnitude. This scaling factor generally must be modified for each variable and different vertical level perturbed as the strength of sensitivity gradients vary between different variables and throughout the domain. In the case under investigation, it has been set to 0.14 for upper tropospheric wind perturbations, 0.08 for mid-tropospheric wind perturbations, and 0.03 for mid-tropospheric temperature perturbations. The locations and magnitudes of these perturbations will be discussed in greater detail in the following chapter during the completion of the SPRD analysis. The magnitude is chosen so that the size of the perturbation is comparable to expected analysis uncertainties for each variable. Once the perturbations have been calculated, they are added to the initial state vector of the control integration.

2) OPTIMAL PERTURBATIONS

To test, ultimately, the interpretation of the forecast sensitivities as well as the assumptions of linearity, adjoint-informed initial condition perturbations are created to add to the control initial conditions to evaluate their impact on the response function and to diagnose their evolution. These perturbations are "optimal" in the sense that they represent the smallest perturbation to the model input (as measured by a quadratic norm) that can produce a prescribed change to a linear or linearized response function, *R*. The formulation of Errico (1997) is used in calculating the optimal perturbation. Here the quadratic norm used to measure the initial condition perturbation is the energy norm defined as:

$$\mathcal{E} = \frac{1}{2}\langle \mathbf{x}_0', \mathbf{W}\mathbf{x}_0' \rangle = \frac{1}{2}\int_0^1 \iint_{\Re} \left(u'^2 + v'^2 + \frac{c_p}{T_{ref}} T'^2 + \frac{L}{c_p T_{ref}} q_v'^2 + \frac{R_d T_{ref}}{p_{ref}} p'^2 \right) d\Re d\eta. \qquad (5)$$

The weights given to those components are given by a reference temperature and pressure, T_{ref} and p_{ref}; as well as the dry air gas constant, R_d; the specific heat of air at constant pressure, c_p; and the specific heat of vaporization, L. The integration is taken over the depth of the atmosphere and over the model domain, $\Re$. The discrete form of this expression may be expressed by the weighting matrix **W**. The total energy, $\mathcal{E}$, of the initial condition perturbation, $\mathbf{x}_0'$, is calculated as:

$$\mathcal{E} = \frac{1}{2}\left\langle \mathbf{x}_0', \mathbf{W}\mathbf{x}_0' \right\rangle, \tag{6}$$

where the energy norm matrix is a diagonal matrix whose elements correspond to the coefficients for each perturbed variable in Equation 5. For an initial condition perturbation with only perturbations to the horizontal flow field, **W**, would provide a measure of the kinetic energy per unit mass and be the identity matrix. To calculate dry energy of the perturbations, we use the diagonal weighting matrix, **W**, with entries of 1 along the diagonal for those entries that weight the wind components, and $\frac{c_p}{T_{ref}}$ for those that weight the temperature, producing an energy norm composed of both kinetic and available potential energy. In the calculation, we calculate the perturbations to initial state that minimize initial energy. This energy could be kinetic energy, kinetic energy plus available potential energy (total dry energy), or kinetic energy combined with available potential energy and latent energy (total moist energy).

To find the minimum of $\mathcal{E}$, subject to the constraint that the initial condition perturbation, $\mathbf{x}_0'$, results in a change in the response function, $\Delta R \cong \delta R = \left\langle \frac{\partial R}{\partial \mathbf{x}_0}, \mathbf{x}_0' \right\rangle$, we use the method of Lagrange multipliers. We define the Lagrangian, L:

$$L = \mathcal{E} + \lambda\left(\delta R - \left\langle \frac{\partial R}{\partial \mathbf{x}_0}, \mathbf{x}_0' \right\rangle \right) \tag{7}$$

where λ is the Lagrange multiplier. The minimum of L, is found at the location where:

$$\frac{\partial L}{\partial \mathbf{x}_0'} = \mathbf{W}\mathbf{x}_0' - \lambda \frac{\partial R}{\partial \mathbf{x}_0} = 0 \text{ or } \mathbf{x}_0' = \lambda \mathbf{W}^{-1} \frac{\partial R}{\partial \mathbf{x}_0} \text{and}$$

$$\frac{\partial L}{\partial \lambda} = \delta R - \left\langle \frac{\partial R}{\partial \mathbf{x}_0}, \mathbf{x}_0' \right\rangle = 0 \text{or } \delta R = \left\langle \frac{\partial R}{\partial \mathbf{x}_0}, \mathbf{x}_0' \right\rangle.$$

Substituting in $\mathbf{x}_0'$, $\delta R = \left\langle \frac{\partial R}{\partial \mathbf{x}_0}, \lambda \mathbf{W}^{-1} \frac{\partial R}{\partial \mathbf{x}_0} \right\rangle = \lambda \left\langle \frac{\partial R}{\partial \mathbf{x}_0}, \mathbf{W}^{-1} \frac{\partial R}{\partial \mathbf{x}_0} \right\rangle$, yields: $\lambda = \frac{\delta R}{\left\langle \frac{\partial R}{\partial \mathbf{x}_0}, \mathbf{W}^{-1} \frac{\partial R}{\partial \mathbf{x}_0} \right\rangle}$.

The initial condition perturbation is thus:

$$\mathbf{x}_0'^{opt} = \lambda \mathbf{W}^{-1} \frac{\partial R}{\partial \mathbf{x}_0} = \delta R \frac{\mathbf{W}^{-1} \frac{\partial R}{\partial \mathbf{x}_0}}{\left\langle \frac{\partial R}{\partial \mathbf{x}_0}, \mathbf{W}^{-1} \frac{\partial R}{\partial \mathbf{x}_0} \right\rangle}. \tag{8}$$

From this expression, we see that the initial condition perturbation is directly proportional to the initial-time adjoint-derived sensitivity gradient in the limiting case where the terms in **W** are constants.

After the perturbations are calculated, inserted into the NLM, and the model integrated to produce a perturbed forecast state, a comparison can be made between the observed change in the response function from the nonlinear evolution of perturbations, ΔR, and the calculated theoretical change in the response function assuming linear evolution of the perturbations, δR. This will help to determine whether the assumption of linearity in the adjoint is appropriate. This calculation can also be helpful in ascertaining the effectiveness of the perturbation in modifying the response function. Vukićević (1991) further discusses the evolution of errors and model integration departures in a comparison of linear and nonlinear evolutions of synoptic cyclogenetic events. It was found that the solutions and error fields associated with TLM integrations were nearly identical in shape and varied only slightly in amplitude compared to the NLM integrations. This helps to assure us that the linear nature of the adjoint integration is not introducing excess error into the experiment. Errico and Vukićević (1991) further show that tangent linear solutions are able to accurately predict the evolution of perturbations out to 36 hours when compared to a nonlinear model. This is especially true for a case study in which the event under consideration is dynamically driven versus diabatically driven.

4. Results of SPRD Analysis

The control (unperturbed) WRF simulation produced a cyclone with a minimum SLP of 958.7 hPa at 0000 UTC 27 October. This is a 1 hPa higher SLP value at this time compared to the NCEP analysis data at this time (Fig. 4.1). Compared to the observed minimum of 955.2hPa at 2213 UTC 26 October, the WRF output indicates that there is a slight deviation in the timing and intensity of the cyclone simulation. It can also be noted that there is a slight shift of the cyclone center to the north in the WRF simulation. Even with these differences the WRF is able to simulate the event quite accurately as the simulated cyclone still undergoes intense development and deepens 23.7 hPa for the 24-hour period ending at 0000 UTC 27 October, compared to deepening 24.8 hPa in the same 24-hour time period as seen in the analysis data. The intense and rapid development of the simulated cyclone is one of the key features that has been crucial in motivating the selection of this case for study. The other feature being the merger of the two surface cyclones. The following sections will be the completion of a 'SPRD' analysis of a 48-hour control forecast, subsequent 48hr adjoint integration, and lastly different 48-hour perturbation forecasts. The analysis will focus on upper- and mid-tropospheric phenomena in order to gain a more robust understanding of wind, vorticity, and temperature dynamics that are most important in the development of this event. Each of the sensitivity, perturbation, response, and diagnosis sections in the SPRD analysis will contain sub-categories as follows. The sensitivity section contains three sub-categories that explore the sensitivity fields of 1) the upper troposphere, 2) a vertical cross section and the mid-troposphere, and 3) the lower troposphere. Next, the perturbation section contains two sub-categories that describe 1) non-optimal perturbations and 2) optimal perturbations. The response section contains two sub-categories that describe the response of the perturbed simulations containing initial state vectors modified with 1) non-optimal perturbations and 2) optimal perturbations. Lastly, the diagnosis section contains two sub-categories that indicate exactly which structures of the model atmosphere were modified in order to produce the response observed in the simulations for both 1) non-optimal and 2) optimal perturbations.

a) Sensitivity

As a qualitative check to ensure that the adjoint simulation results are reasonable, an examination of some of the sensitivity fields from the first hour of the adjoint integration (forecast hour 47) is completed. Figure 4.2a depicts 850 hPa sensitivity to temperature and wind at this time as indicated by the fill patterns and vectors respectively. The sensitivity fields indicate two ways to increase the response function (decrease the mass of the column) through modification of the model state one hour prior to evaluation of the response function: warm the column at 850 hPa and/or perturb the winds in such a way that mass is diverged from the column (Fig. 4.2a). The increase in temperature would immediately result in a hydrostatic impact of lower surface pressure. The divergence of mass from the column above the regions defining the response function would have the same result. An examination of a vertical cross section through the region of high sensitivity (Fig. 4.2b) reveals that both sensitivity fields remain consistent throughout the depth of the model atmosphere, although the fields begin to weaken considerably above 200 hPa. An examination of these two sensitivities fields across the entire domain indicates that the largest sensitivities are located in the immediate region in which the response function is defined. This is reasonable as perturbations made outside of the immediate region of the response function do not have enough time to evolve in one hour to have a large impact on the response function.

1) UPPER TROPOSPHERE

Initial time sensitivity analysis at the jet level, 300hPa, indicates that the most predominate wind sensitivities lie in the immediate vicinity of the jet. From the sensitivity to the zonal and meridional components of the wind ($\hat{u}$ and $\hat{v}$), sensitivity to relative vorticity ($\hat{\zeta}$) can be diagnosed from sensitivities to the horizontal wind (Kleist and Morgan, 2005), through the solution of a Poisson-type equation:

$$\nabla^2\hat{\zeta} = -\left(\frac{\partial \hat{v}}{\partial x} - \frac{\partial \hat{u}}{\partial y}\right) \tag{1}$$

It is seen that the sensitivity vectors are oriented in such a way that they are associated primarily with regions of sensitivity to *cyclonic* vorticity along the cyclonic shear side of the jet as well as some minor regions of sensitivity to *anticyclonic* vorticity along the anticyclonic shear side of

the jet (Fig. 4.3). The sensitivity to wind and vorticity fields indicate that if the existent jet were modified in such a way as to increase its speed and to narrow it, a stronger surface cyclone should be produced 48 hours later at the final forecast time. Perhaps another enhancement to development is indicated by the flow pattern that is likely to result (large dark blue arrows) due to vorticity perturbations in the indicated sensitive regions. It can be seen that there is a proportion of the flow oriented to the thermal gradient in such a way that cold advection into the jet will occur. This will help to enhance the trough located downstream and any upper-tropospheric PV anomaly associated with it. It will also work to enhance subsidence of high PV stratospheric air into the jet and increase the strength of the tropopause fold that is present. Interestingly, an examination of sensitivity to temperature at this level yields no clear pattern in the field (not shown). There is also a region of sensitivity to anticyclonic vorticity located downstream of the trough axis over Minnesota and Wisconsin. This feature indicates that if the ridge were enhanced downstream of the trough axis, there would be greater divergence between it and the trough axis, adding to the large-scale ascent in this region which is critical for cyclogenesis.

2) CROSS SECTION AND MID-TROPOSPHERE

In order to further examine how the upper-tropospheric wind, temperature, and associated potential vorticity might be perturbed to enhance the development of the cyclone, a cross section through the jet (along segment A-B in Fig. 4.4) is examined (Fig. 4.5). A strong tropopause fold and upper front can be seen in association with the intense jet. The sensitivities to vorticity apparent on the cyclonic and anticyclonic fringes of the jet at 300hPa are much weaker than those located below the jet. There is a maximum in sensitivity to vorticity located near 600 hPa within the cross section. The cyclonic vorticity sensitivity is resident within the tropopause fold. Adding sensitivity to temperature to the cross section (Fig. 4.6) allows for a discussion of the impact of temperature and vorticity perturbations on the distribution of mid-tropospheric PV on the cyclone intensity. The maximum in the sensitivity fields at mid-levels indicate that perturbations within the mid-troposphere are more effective at intensifying the cyclone than perturbations of the same amplitude in the upper troposphere. Thermal wind balance requires that if temperature perturbations were made within the sensitive regions indicated, the already strong horizontal temperature gradient below the jet will become even stronger and thus intensify

the jet. The intensification of the jet will subsequently increase the cyclonic and anticyclonic shear not only all along the jet, but also in the sensitive regions indicated in the figure. It must also be noted that there exists a region sensitive to cold perturbations near 600 hPa that extends from the cold side of the baroclinic zone to the warm side that would have no effect in enhancing the thermal wind if perturbations were placed there. However, cold perturbations placed here *would* enhance the vertical stratification above the region. An examination of the equation defining Ertel's PV (Eqn. 2), translates how these perturbations to vorticity and temperature in the sensitive regions would increase the PV perturbation associated with the tropopause fold:

$$q = -g(\zeta + f)\frac{\partial \theta}{\partial p} \tag{2}$$

Ertel PV will increase if the cyclonic vorticity and/or the potential temperature stratification were to increase.

The location of the maximum in sensitivity to cyclonic vorticity and maximum in sensitivity to cold temperature perturbations, are located directly in the region that will further enhance the already existent tropopause fold. If this tropopause fold were enhanced, so too would the surface cyclone's mid-tropospheric cyclogenetic precursor. The enhanced downstream positive vorticity advection (PVA) of this precursor would aid in producing greater height falls at mid- and lower-tropospheric levels and enhance cyclone development. This hypothesis will be tested in the perturbation experiments described later.

3) LOWER TROPOSPHERE

Lower-tropospheric sensitivities to temperature and wind will be examined at 0000 UTC 26 October (forecast hour 24). 850 hPa sensitivity fields to temperature and wind at forecast hour 24 indicate that the most prominent sensitivities are situated to the southwest of the nascent southern cyclone over Kansas (Fig. 4.7). The most conspicuous feature in the sensitivity to temperature field indicates that an increase in baroclinicity along the developing cold front is critical to enhancing future development of the southern cyclone. Interestingly, it is noted that the robust distribution of sensitivity to temperature along the trailing cold front is only present during the first few hours of development of the southern cyclone. Once cyclogenesis is initiated, other dynamics become more important to development (mid-tropospheric vorticity dynamics for example) of the cyclone than low level baroclinicity directly near the cyclone.

Sensitivities to the temperature field at this time indicate that development is sensitive to enhanced warming within the warm sector (Fig. 4.7). It has been found that reductions in the static stability within the warm sector by the addition of warm perturbations throughout, can greatly enhance explosive cyclogenesis (Nuss and Anthes, 1987). A possible side effect of this reduced static stability is the likelihood of increased convection ahead of the cold front as the system propagates eastward. This will help to further enhance the severe weather that lead to much of the damage associated with this event.

Hydrostatically, an increase in temperature within the warm sector will be associated, through the hypsometric equation, with an increase in geopotential height of the column. This increase in height in the warm sector will help to enhance the ridge downstream of the upper-tropospheric trough and create a mid-tropospheric synoptic environment more conducive for large-scale ascent (due to divergence of the ageostrophic wind between the trough and ridge axes). These mechanisms, as inferred from the sensitivity fields, would be favorable in supporting the enhanced development of the southern cyclone.

A cross section through the maxima in temperature sensitivities and taken nearly normal to the baroclinic zone reveals a northwestward tilt with height of the sensitivity to temperature field (Fig. 4.8). The vertical shear associated with any increase of baroclinicity in this region will enhance the circulation associated with the developing frontal region. This is critical in helping to convert the potential energy stored in the thermal structure into kinetic energy which will help to enhance development of the cyclone.

An examination of the sensitivity to lower-tropospheric wind (Fig. 4.7) reveals two important results: 1) The sensitivity to wind field in conjunction with the isotherms indicate that enhanced cold air advection within the region sensitive to cold temperature perturbations, and warm air advection into the region sensitive to warm temperature perturbations would increase the baroclinicity along the front, and hence cyclone intensity 24-hours later; and 2) an enhancement of the already strong 850hPa southerly jet will lead to a stronger cyclone by advecting more of the warm, moist air present over the Gulf of Mexico into the southern Plains (Fig. 4.7). These observations allow us to note how closely connected the wind and temperature sensitivities are to each other at these low levels and one can deduce that temperature characteristics of the lowest levels of the atmosphere are most important to intense extratropical cyclogenesis.

In order to test these hypotheses, the impact of perturbations to the initial state on the control cyclone simulation are studied in the next section.

b) Perturbations

A brief description of the calculation of initial state perturbations that will be inserted into the control simulation will be provided in this section, the effects of these perturbations on the outcome of a model forecast will be compared to that of the control forecast and will be discussed in the next section. Non-optimal perturbations and optimal perturbations are used in this study. Non-optimal perturbations are those that are calculated based on a scaling of the adjoint derived sensitivity fields. Optimal perturbations are constrained to minimize the initial perturbation energy that upon evolution, achieve a prescribed change to the response function. Since this study is focused upon the upper- and mid-tropospheric dynamics that influence the development of the southern cyclone as described earlier, non-optimal perturbations will be calculated and inserted into the model upper and mid-troposphere only. Optimal perturbations will more objectively perturb the entire model state wherever regions of large sensitivity reside. Since the largest sensitivities are found to lie in the mid- to lower troposphere at the initial forecast time, the optimal perturbations that have been calculated will preferentially perturb these regions of the model. Both types of perturbations will be calculated and inserted into the model at the initial time.

1) NON-OPTIMAL PERTURBATIONS

Non-optimal perturbations have been calculated for the jet level and mid-troposphere and are inserted over the horizontal domain indicated in Fig. 4.9. For each variable, the non-optimal initial perturbations are calculated by scaling the sensitivity field at the initial time, $\left(\frac{\partial R}{\partial \mathbf{x}_0} \right)$ for that variable by a scalar weighting factor, α, in order to produce initial condition perturbations proportional to the sensitivity field (Eqn. 3):

$$\mathbf{x}_0' = \alpha \frac{\partial R}{\partial \mathbf{x}_0} \tag{3}$$

At jet level, the clearest and most consistent sensitivity pattern is that of the wind. The non-optimal perturbations calculated at the jet level lie between the 27 and 31 eta levels which interpolated to pressure coordinates is approximately between the 200 hPa and 400 hPa pressure surfaces. Magnitude of the largest wind perturbation is 2.1 m s^{-1} and found at the 350 hPa level. The horizontal region in which these perturbations are inserted is denoted by the box in Fig. 4.9 (this region is used for both the upper- and mid-tropospheric perturbations described below). The distribution and relative strength of the wind perturbations at 300 hPa at the initial time is depicted in Fig. 4.10a.

In the mid-troposphere, non-optimal wind perturbations have been calculated and inserted between the 16 and 20 eta levels which interpolated to pressure coordinates is approximately between the 400 hPa and 650 hPa pressure surfaces. The magnitude of the largest wind perturbation is 1.7 m s^{-1} and found at the 600 hPa level. The wind perturbation values are those taken to be within the maximum value one may expect to find in the error of an observation taken at these levels (Fig. 4.10b).

Non-optimal perturbations to temperature, calculated from the sensitivity to temperature described earlier are made within the same horizontal region and vertical extent as for mid-tropospheric wind perturbations (Fig. 4.10c). The maximum temperature perturbation for this perturbation is 1.5K and found at 550 hPa.

2) OPTIMAL PERTURBATIONS

Recall from the Data and Methods chapter, optimal perturbations, $\mathbf{x}_0^{'opt}$, are defined as those initial perturbations with minimum energy that produce a prescribed change, δR, in the response function and are calculated as:

$$\mathbf{x}_0^{'opt} = \delta R \frac{\mathbf{W}^{-1} \frac{\partial R}{\partial \mathbf{x}_0}}{\left\langle \frac{\partial R}{\partial \mathbf{x}_0}, \mathbf{W}^{-1} \frac{\partial R}{\partial \mathbf{x}_0} \right\rangle} \tag{4}$$

where $\mathbf{W}$ is the inverse of the weighting matrix used to define the norm measuring initial perturbation amplitude.

The optimal perturbations to wind and temperature calculated are found to lie mostly between the 450 hPa and 800 hPa pressure levels. For a prescribed change of δR= -2.5 hPa the range of values for the perturbation wind speed at these levels was 0.8 m s^{-1} to 2.5 m s^{-1}, while the range for temperature was -1.5K to 1.5K. The horizontal distribution of these perturbations are concentrated in two regions: immediately upstream of the mid-level trough axis and in the region of the mid-level ridge downstream of the trough axis. This general pattern holds throughout the depth of the mid-troposphere (e.g., at 550 hPa level; Fig. 4.10d).

c) Response

1) NON-OPTIMAL PERTURBATIONS

The response of cyclone development to the non-optimal upper-tropospheric wind perturbations was a 0.1 hPa deeper cyclone at the final (48-hour) forecast time and a cyclone positioned slightly to the northeast relative to the control. While the perturbations are designed to have an impact on the response function (minus the averaged mass in the 988 hPa sea level isobar at 48-hours), other variables will necessarily have changed also. Figure 4.11a shows also that there are small temperature perturbations throughout much of the troposphere. At 650 hPa they are 1°C within the region defined by the response function. The anomalies present at this level indicate no strong signature in the temperature field (Fig. 4.11a).

The response of the cyclone intensity to the non-optimal mid-tropospheric wind perturbations resulted in a 2 hPa deeper cyclone that shifted slightly to the south-southeast of the cyclone in the control forecast. The 650 hPa temperature perturbations indicate an enhanced pocket of warm air in the mid-troposphere associated with the cyclone center of the perturbed forecast. The temperature difference is 1.5°C at this level (Fig. 4.11b). From 0000 UTC 26 October to 0000 UTC 27 October the cyclone achieved “bomb” status as it deepened 25.6 hPa over the period.

The wind perturbations made within the upper and mid-troposphere were able to modify each simulation in a way that the *efficiency* with which they were able to deepen the storm was

similar. This measure, known as *linearity,* describes how well perturbations calculated based on the linear set of equations of the adjoint, evolve in a nonlinear forward trajectory. It can describe how effective perturbations are in affecting the response function. The upper-tropospheric experiment maintained 57% linearity and the mid-tropospheric experiment maintained 60% linearity. Since both the magnitude of the perturbations and the linearity are similar in each of the experiments, more merit can be given to the conclusion that mid-tropospheric wind perturbations below the jet are indeed more effective at modifying the response function and increasing cyclone intensity than wind perturbations made within the jet (also indicated by the distribution of the sensitivity fields).

Lastly, non-optimal mid-tropospheric perturbations to temperature produced a cyclone that was 1.7 hPa deeper than the control and featured a slight shift to the south as well. There is again a strong warm perturbation of 1.5°C evident within the shifted cyclone center at 650 hPa (Fig. 4.11c). The simulated cyclone rapidly intensified, deepening 25 hPa between 0000 UTC 26 October to 0000 UTC 27 October.

Of the three non-optimal experiments, mid-tropospheric perturbations to temperature will be the focus in the coming sections.

2) OPTIMAL PERTURBATIONS

An optimal perturbation was created with the intent to decrease the response function by 2.5 hPa. The perturbed cyclone achieved a decrease of 6.1 hPa along with a slight shift to the south (Fig. 4.11d) - bringing it closer to its true position as shown by the NCEP analysis data (Fig. 4.1b). The deepening rate observed in this case was 27.9 hPa in the 24-hour period between 0000 UTC 26 October and 0000 UTC 27 October. Also of importance, there is a 5.7°C increase in temperature at 650 hPa (Fig. 4.11d).

As briefly described in the previous section, since the non-optimal and optimal perturbations have been calculated based on the adjoint model and the linear system of equations associated with it, the evolution of the perturbations utilizing a nonlinear system of equations in a forward evolving model will cause a deviation in the outcome of the response function from

what is to be expected. The degree in which the perturbations maintain their linearity at the final forecast time can be calculated by the relation shown below (Eqn. 5).

$$\frac{\Delta R}{\delta R} \tag{5}$$

where 'δR' represents the prescribed, *linear* change in the response function and 'ΔR' represents the observed change in the response function calculated from the response function difference between the perturbed and control forecasts. Based on this calculation, 53% linearity was maintained in the optimal perturbation experiment. This means that the decrease in pressure averaged within the 988 hPa SLP contour should be approximately 1.3 hPa. As comparison, in the case of the non-optimal mid-tropospheric temperature perturbations, 43% linearity was maintained.

d) Diagnosis

The following section will investigate the dynamical processes and adjustments associated with the evolution of the perturbed simulations in order to determine the most pertinent upper- and mid-tropospheric processes that have been critical in the modulation of explosive development of this event.

1) NON-OPTIMAL PERTURBATIONS

As shown in the previous section, mid-tropospheric perturbations produced the greatest response in cyclone development for the case under investigation. A comparison between the impact of mid-tropospheric wind perturbations and temperature perturbations on cyclone intensity reveals that the model atmosphere produced the same response to these different perturbations. Therefore, the impact of mid-tropospheric temperature perturbation on the cyclone evolution will be explored exclusively.

At 24-hours into the perturbed simulation, an enhancement of the upper-tropospheric PV anomaly apparent in the unperturbed base state near the jet exit region (Fig. 4.12), directly upstream of the developing surface cyclone over Kansas, is the main driver of enhanced

cyclogenesis. This enhancement of Type B cyclogenesis due to a strengthening of an upper-tropospheric PV feature perhaps indicates that a strong precursor PV anomaly and upper front are critical in the explosive development of this cyclone. A cross section taken along segment A-B in Fig. 4.12 is shown in Fig. 4.13. The cross section indicates an enhancement of this feature and the upper front associated with it. *It is noted that these perturbations are exceedingly small, but as will be shown with the larger, optimal perturbation, with its more robust impact, the processes noted here will still be relevant.* An enhancement of the tropopause fold, and associated increase in mid-tropospheric vorticity, imply lower geopotential heights in the base of the amplified trough. An amplification of the trough will then mean enhanced vorticity production due to curvature and will strengthen the effect of positive vorticity advection (PVA) by the thermal wind. Increased PVA will generate subsequently more ascent downstream of the trough axis as described by the absolute vorticity advection term in the Trenberth (1978) form of the quasi-geostrophic (QG) omega (ω) equation (Eqn. 6):

$$\sigma\left(\nabla^2 + \frac{f_0^2}{\sigma}\frac{\partial^2}{\partial p^2}\right)\omega \approx 2\left[f_0 \frac{\partial \overrightarrow{V_g}}{\partial p} \cdot \nabla\left(\zeta_g + f\right)\right] \qquad (6)$$

As described above, an enhanced tropopause fold contributes to enhanced PVA by the thermal wind. Subsequently, mid-tropospheric height falls within the trough are enhanced, which helps to sharpen the trough and generate more relative vorticity. Analysis of mid-tropospheric perturbations beginning at forecast hour 24 (the time at which the southern cyclone begins to develop over Kansas) indicate that there are indeed lower geopotential heights at 550 hPa at this time in the base of the trough compared to the control forecast. Congruent with this is a small positive vorticity anomaly upshear of the developing southern surface cyclone (Fig. 4.14a). Interestingly, there is also a small positive vorticity anomaly upshear of the surface cyclone to the north.

As the forecast evolves, the mid-level trough continues to deepen. At forecast hour 30, both the vorticity perturbations and trough, now situated over southern Iowa and northern Missouri, have evolved to become more favorable to development (Fig. 4.14b). Curiously, while there is a clear, but small scale, positive vorticity perturbation associated with the northern cyclone, there exists an increase of geopotential height centered over the North and South Dakota borders. A

cross section taken through the region of increased height reveals that there is a decrease in stratification throughout the lower to mid-troposphere, and subsequently, a decrease in low to mid-tropospheric PV (not shown). The increased geopotential height within the region are likely due to reduced PVA by the thermal wind within the mid-troposphere as read in the context of the Trenberth form of the QG-omega equation as described above.

By forecast hour 36, a larger area within the base of the trough is associated with lowered geopotential heights while higher heights still exist near the southern edge of the cut off. The vorticity perturbation has also become stronger and more directly aligned with the surface cyclone (Fig. 4.14c). A cross section through the region indicated in Fig. 4.14c reveals that at this stage of cyclogenesis, characterized by explosive intensification, mid-tropospheric positive vorticity perturbations upshear of the developing cyclone, driven by a lowered tropopause and enhanced upper-tropospheric PV anomaly, are the main drivers of enhanced cyclogenesis (Fig. 4.15a). The upshear tilt of the PV and relative vorticity structures above the cyclone (between the surface and 450 hPa) are another strong indication that development of the cyclone will continue. As the perturbed simulation continues to evolve, the faster flow aloft will tilt these vorticity structures more in the vertical. Once tilted and stacked directly above the surface circulation, the cyclone will have reached its peak intensity. Once vertically stacked the cyclone will begin to weaken as there is no longer any forcing to promote development. From a hydrostatic viewpoint, the warm temperature perturbation that exists near the surface, directly above the cyclone may be indicative of the enhancement of the warm seclusion previously mentioned at the final forecast time (Fig. 4.15b). Another region of interest lies congruent with the enhanced tropopause. Colder air exists below the region of enhancement while warmer air above indicating increased stability. In the context of Ertel's PV as discussed earlier, this indicates a region of enhanced PV upshear of the surface cyclone, a location that is conducive to continued development.

2) OPTIMAL PERTURBATIONS

As shown with the non-optimal perturbations, a cross section through the jet exit region depicted in Fig. 4.12, the experiment utilizing optimal perturbations reveals an enhancement of the tropopause fold and upper front much larger than the non-optimal perturbation experiment (Fig. 4.16). The optimal perturbations were *designed* to produce a response function change of -

2.5 hPa at the final forecast time, whereas the non-optimal wind and temperature perturbations are perturbations that were designed to be within the error threshold for observations taken at their respective vertical levels. Therefore, there was no prescribed size for the perturbation horizontal wind components or the perturbation temperature in the optimal perturbation experiment, and the non-optimal perturbations were not prescribed to meet the -2.5 hPa response function change established for the optimal perturbations.

Analysis of 550 hPa relative vorticity perturbations beginning at forecast hour 24 indicate that there are indeed lower geopotential heights at 550 hPa at this time, again in the base of the trough. Consistent with this is a positive vorticity anomaly to the north-northwest of the developing surface cyclone (Fig. 4.17a). Six hours later, the mid-tropospheric trough continues to deepen. At forecast hour 30 the vorticity perturbation associated with the southern cyclone becomes oriented more favorably upshear of the surface cyclone. The trough has also evolved to become more favorable for further cyclone development within the previous six hours as shown by lower geopotential heights throughout the base (Fig. 4.17b). Advancing another six hours to forecast hour 36, the alignment of the vorticity perturbation continues to remain favorable. The deepening of the trough continues as the extent in which the deepening is occurring becomes broader as well (Fig. 4.17c). A cross section through the region indicated in Fig. 4.17c reveals that there are similar vorticity perturbations between the surface and 450 hPa compared to the non-optimal case investigated in the previous section (Fig. 4.18a). Temperature structures remain quite similar as well, indicating the enhancement of warm air in the cyclone center as well as enhanced stratification near the tropopause contributing to a stronger tropopause fold.

The warm temperature perturbations found at 650 hPa, and the mid-troposphere in general as described in the previous sections, are likely indicative of an enhancement of the warm seclusion that often forms with deeply occluded extratropical cyclones. As the cold front over runs the warm front, a pocket of warm air is essentially cut off and trapped at the cyclone center. An enhancement of this feature indicates a stronger cyclonic circulation prior to occlusion. The enhanced circulation effectively enhances the advection of warm air from the warm sector along the warm front of the cyclone toward the center. This warming near the cyclone center is consistent with the interpretation of the 1-hour back in time adjoint sensitivity to temperature field (Fig. 4.2) that suggested warm temperature perturbations near the cyclone center would be associated with a reduction of surface pressure an hour later.

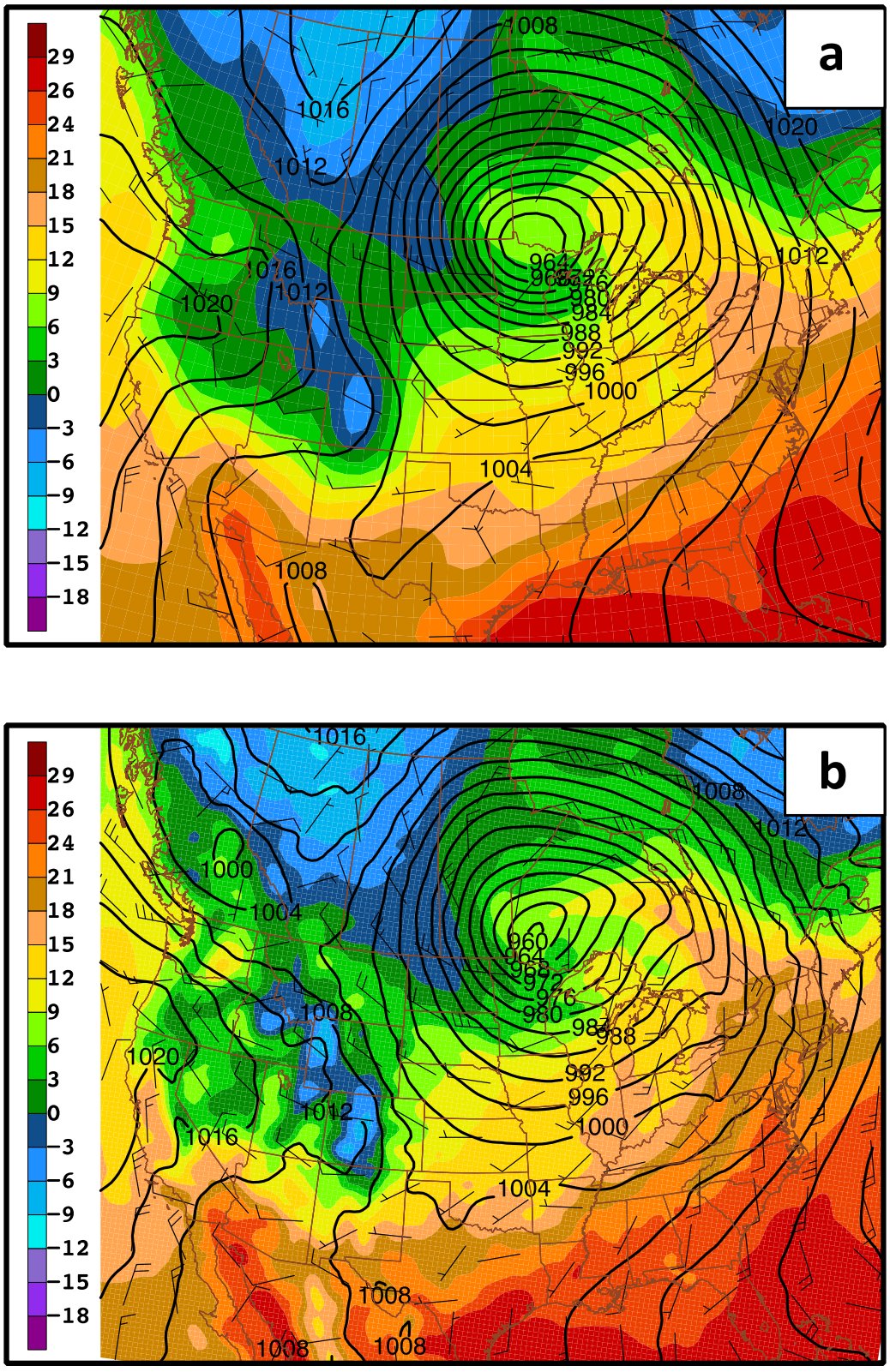

Figure 4.1. 0000UTC 27 October 2010 surface conditions: (a) Analysis of NCEP analysis data used to initialize the WRF model. 2 meter above ground temperature in Celsius (fill pattern, interval 3°C), 10 meter above ground wind (barbs, knots), and sea level pressure (black contours, interval 4 hPa). (b) Same as in (a) except for the final forecast time of the WRF simulation.

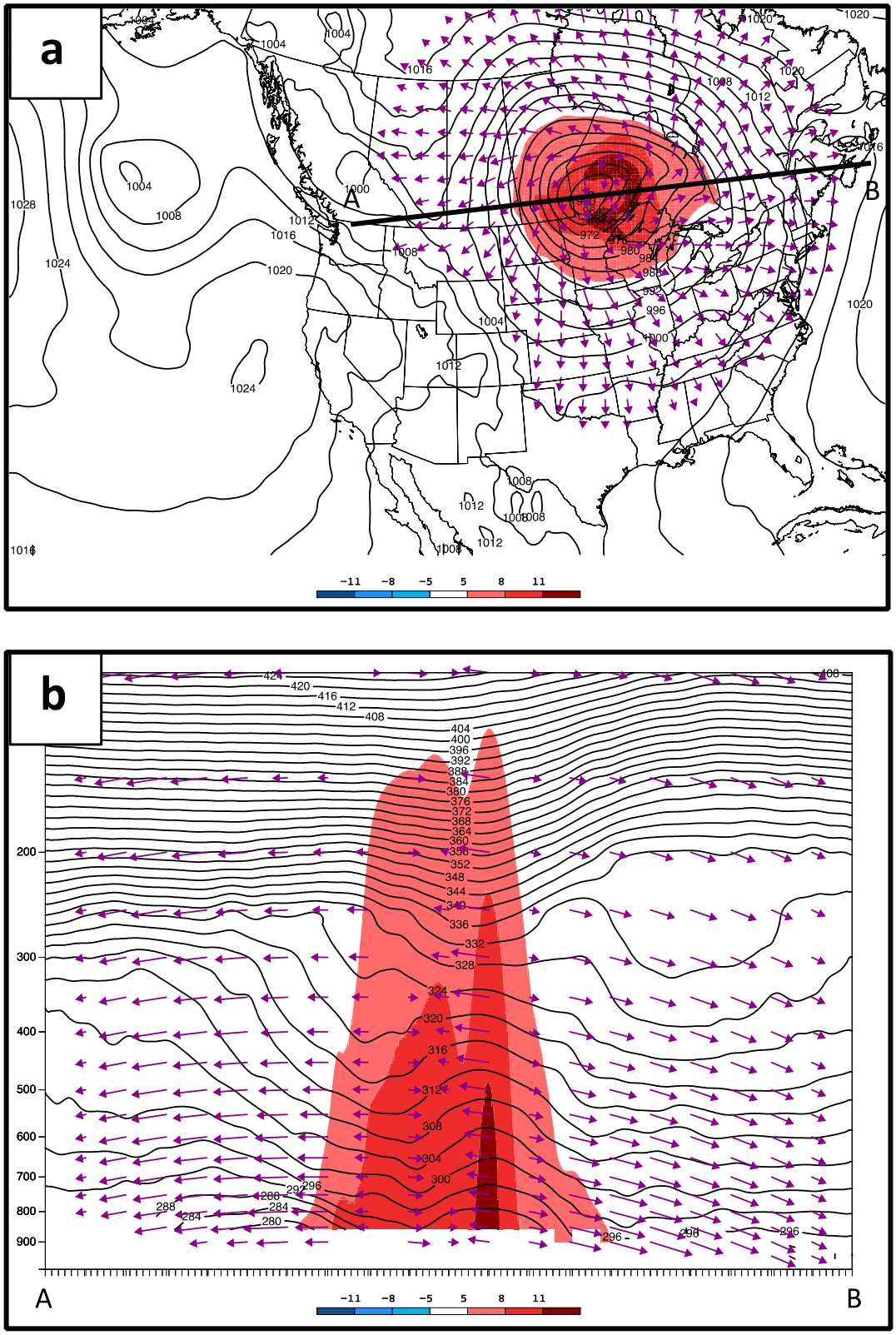

Figure 4.2. Sensitivity analyses taken one hour into the adjoint integration (forecast hour 47). (a) 850 hPa sensitivity to temperature (red fill, warm beginning at 5 Pa K^{-1}; blue fill, cold beginning at -5 Pa K^{-1}, interval 3 Pa K^{-1}), sensitivity to wind (vectors), and location of cross section indicated by line A-B. (b) Sensitivity to temperature (red fill, warm beginning at 5 Pa K^{-1}; blue fill, cold beginning at -5 Pa K^{-1}, interval 3 Pa K^{-1}), sensitivity to wind (vectors), and isentropes (black contours, interval 4K).

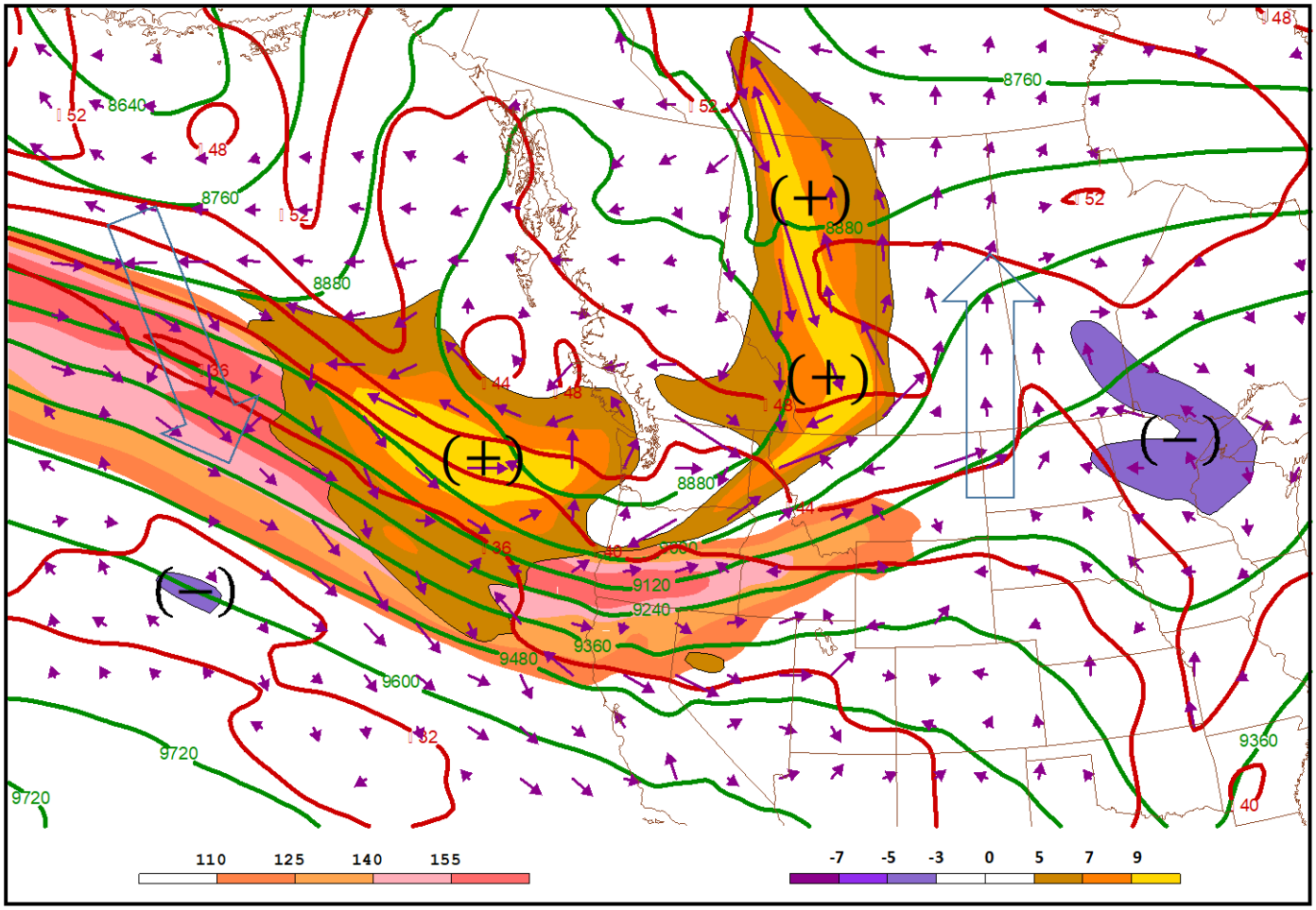

Figure 4.3. 300 hPa geopotential height (green contours, interval 120 m), jet core (peach fill, contoured every 15 knots beginning at 110 knots), temperature (red contours, interval 4°C), sensitivity to relative vorticity (gold fill, positive beginning at 5×10^{-5} Pa s; purple fill, negative beginning at -3×10^{-5} Pa s, interval 2×10^{-5} Pa s), sensitivity to wind (purple vectors), and resultant wind enhancements due to vorticity perturbations inserted into regions of high sensitivity to vorticity at initial forecast time (large blue vectors) at 0000 UTC 25 October.

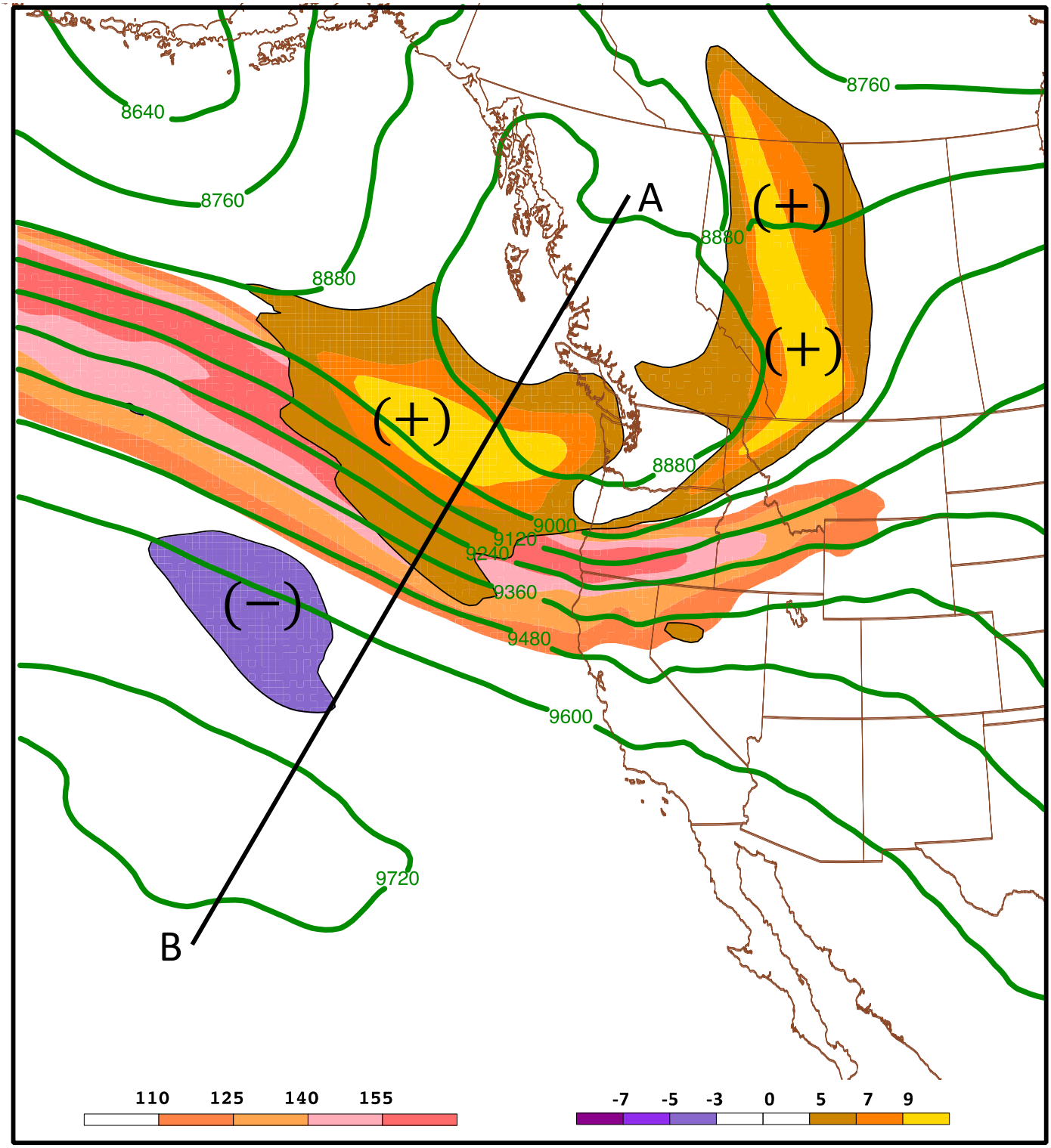

Figure 4.4. Location of cross section shown in figs 5 and 6 taken at 0000 UTC 25 October.

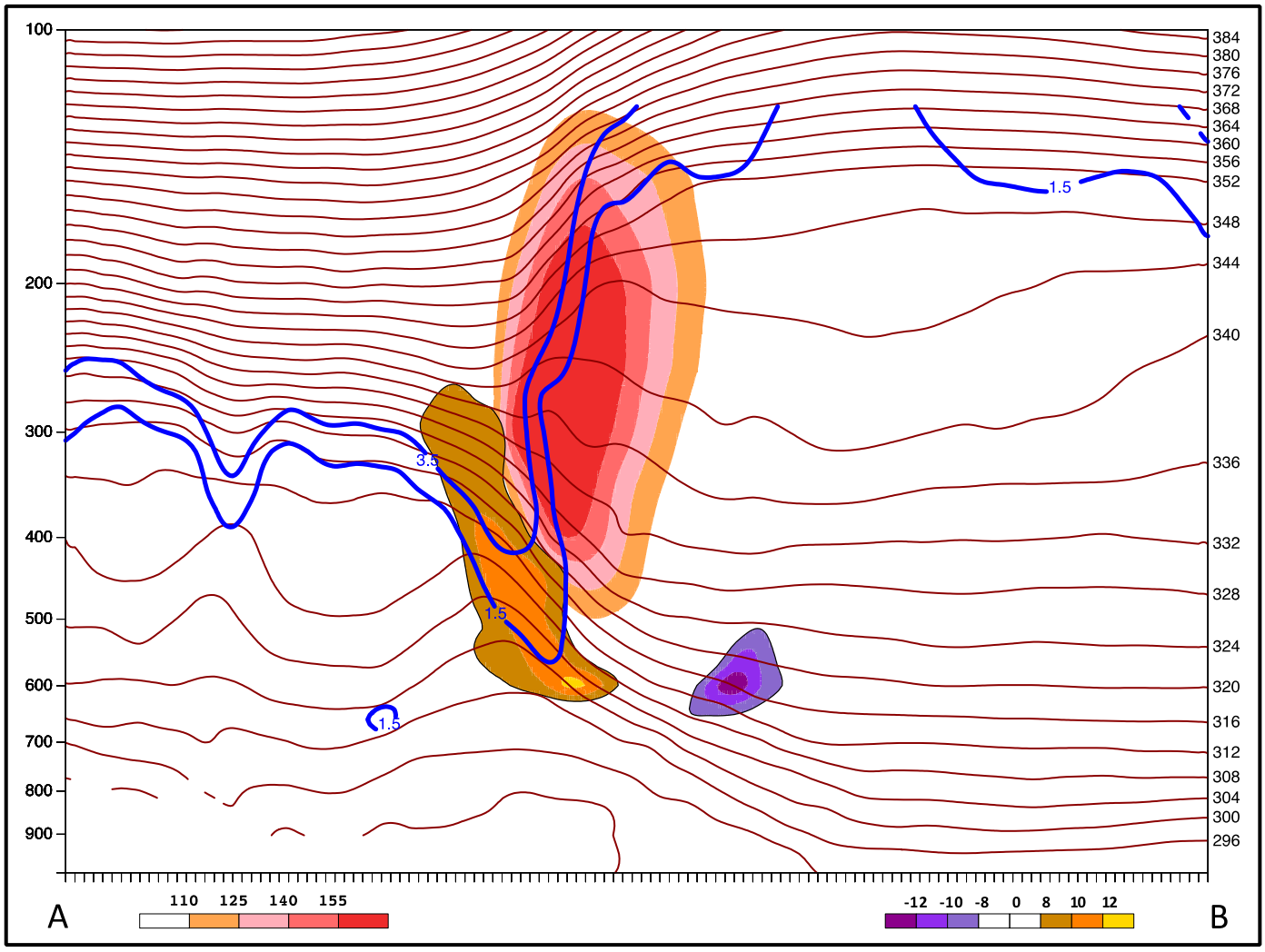

Figure 4.5. Cross section taken through location indicated in fig 4. Jet core (peach fill, contoured every 15 knots beginning at 110 knots), potential temperature (dark red contours, interval 4K), sensitivity to relative vorticity (gold fill, positive beginning at $8x10^{-5}$ Pa s; purple fill, negative beginning at $-8x10^{-5}$ Pa s, interval $2x10^{-5}$ Pa s), and 1.5 and 3.5 PVU surfaces (blue contours) at 0000 UTC 25 October.

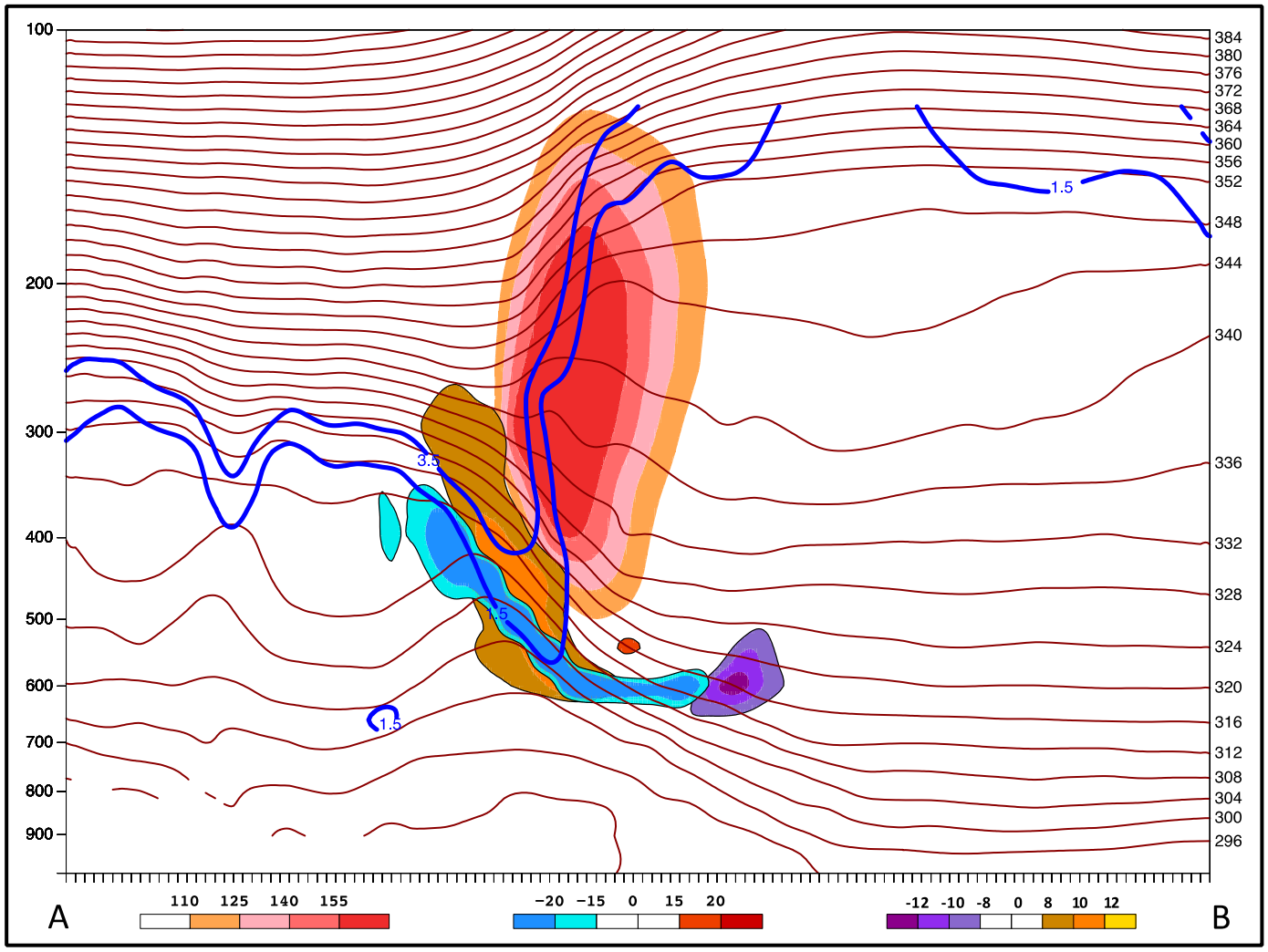

Figure 4.6. Cross section taken through location indicated in fig 4. Jet core (peach fill, contoured every 15 knots beginning at 110 knots), potential temperature (dark red contours, interval 4K), sensitivity to relative vorticity (gold fill, positive beginning at 8×10^{-5} Pa s; purple fill, negative beginning at -8×10^{-5} Pa s, interval 2×10^{-5} Pa s), sensitivity to temperature (red fill, warm beginning at 15 Pa K^{-1}; blue fill, cold beginning at -15 Pa K^{-1}, interval 5 Pa K^{-1}), and 1.5 and 3.5 PVU surfaces (blue contours) at 0000 UTC 25 October.

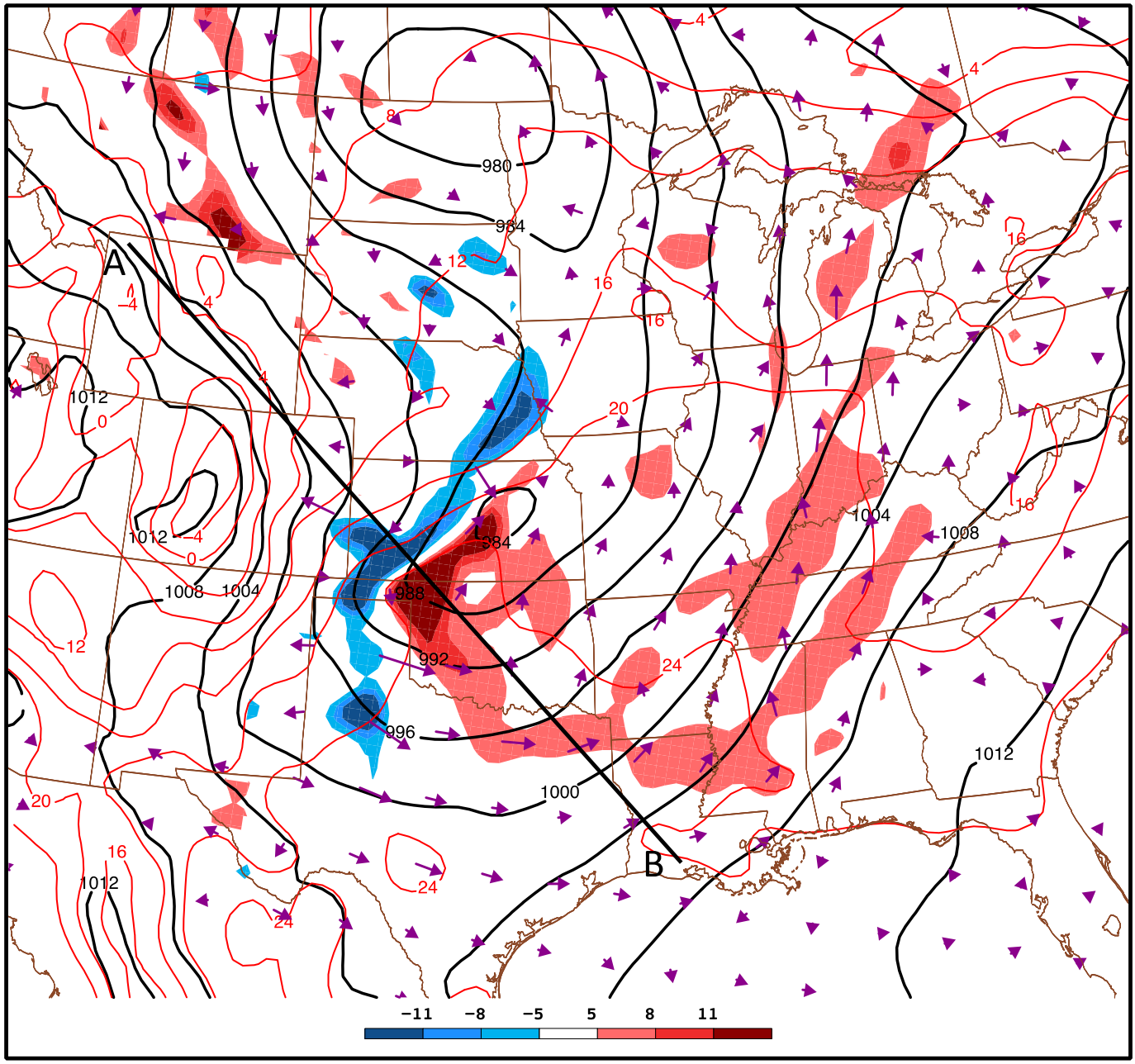

Figure 4.7. 0000 UTC 26 October depiction of sea level pressure (black contours, interval 4 hPa), 850 hPa sensitivity to temperature (red fill, warm beginning at 5 Pa K^{-1}; blue fill, cold beginning at -5 Pa K^{-1}, interval 3 Pa K^{-1}), sensitivity to wind (purple vectors), two meter above ground temperature (red contours, interval 4°C), and line depicting location of cross section in fig 8 from A to B.

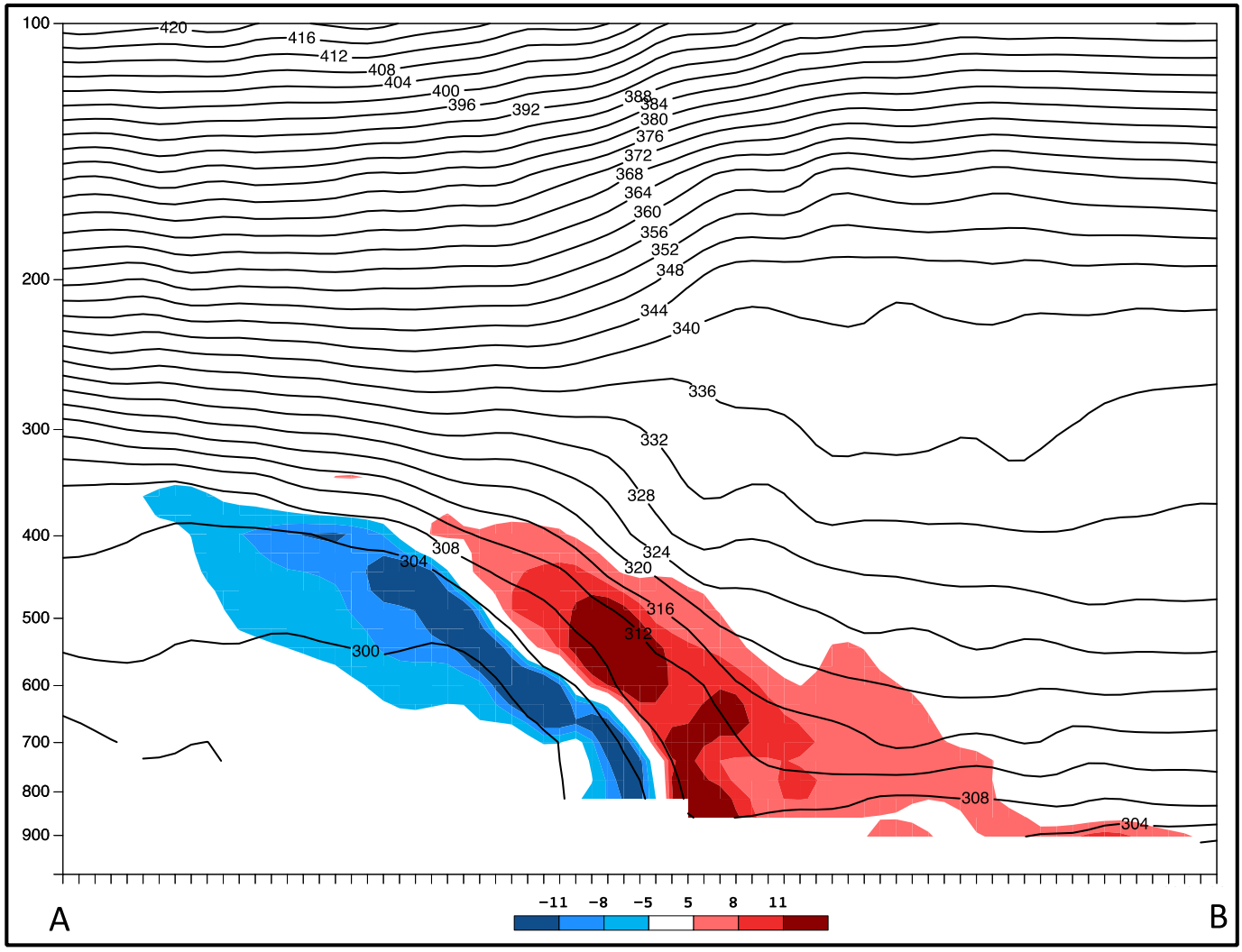

Figure 4.8. 0000 UTC 26 October depiction of potential temperature (black contours, interval 4K) and sensitivity to temperature (red fill, warm beginning at 5 Pa K^{-1}; blue fill, cold beginning at -5 Pa K^{-1}, interval 3 Pa K^{-1}) taken along line A-B as shown in fig 7.

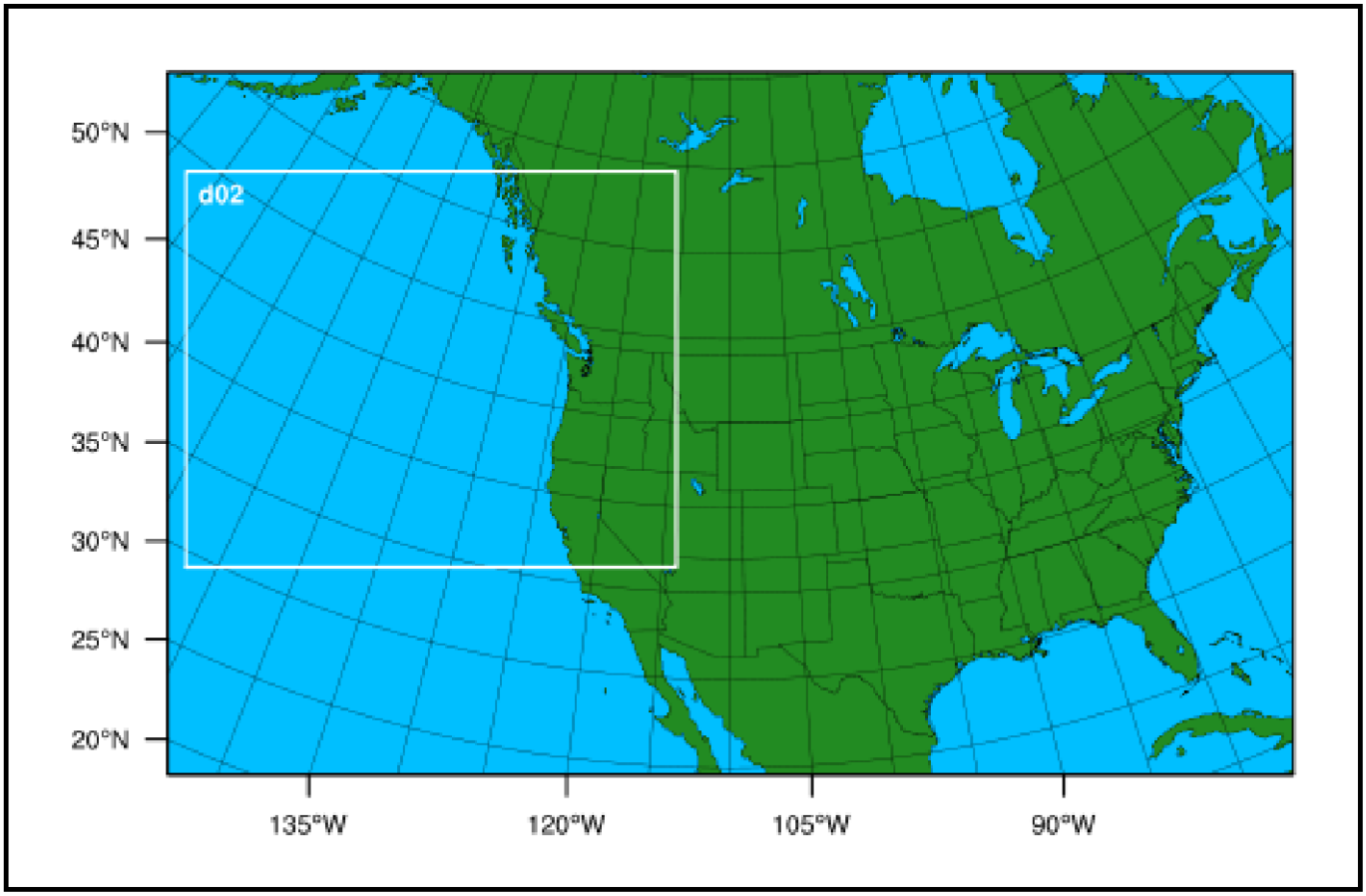

Figure 4.9. Horizontal extent in which the non-optimal perturbations have been inserted into the model are represented by the box ‘d02’.

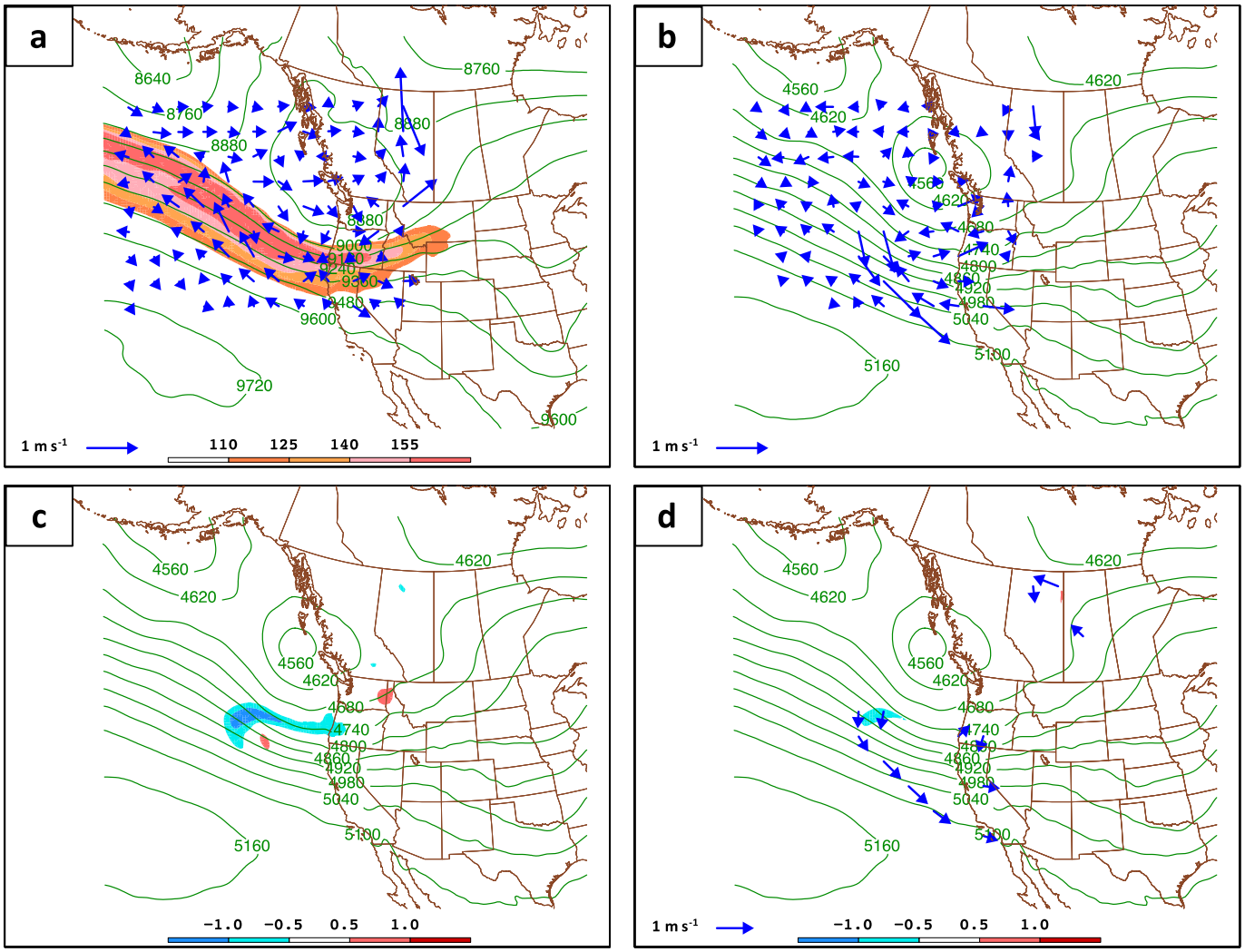

Figure 4.10. Perturbation maps for 0000 UTC 25 October 2010: (a) 300 hPa geopotential height (green contours, interval 120 m), non-optimal wind perturbations (blue vectors, m s^{-1}), and isotachs (fill, interval 15 knots above 110 knots); (b) 550 hPa geopotential height (green contours, interval 60 m) and non-optimal wind perturbations (blue vectors, m s^{-1}); (c) 550 hPa geopotential height (green contours, interval 60 m), non-optimal temperature perturbations (red fill, warm beginning at 0.5°C; blue fill, cold beginning at -0.5°C; interval 0.5°C); (d) 550 hPa geopotential height (green contours, interval 60 m), optimal temperature perturbations (red fill, warm beginning at 0.5°C; blue fill, cold beginning at -0.5°C; interval 0.5°C), and optimal wind perturbations (blue vectors, m s^{-1}).

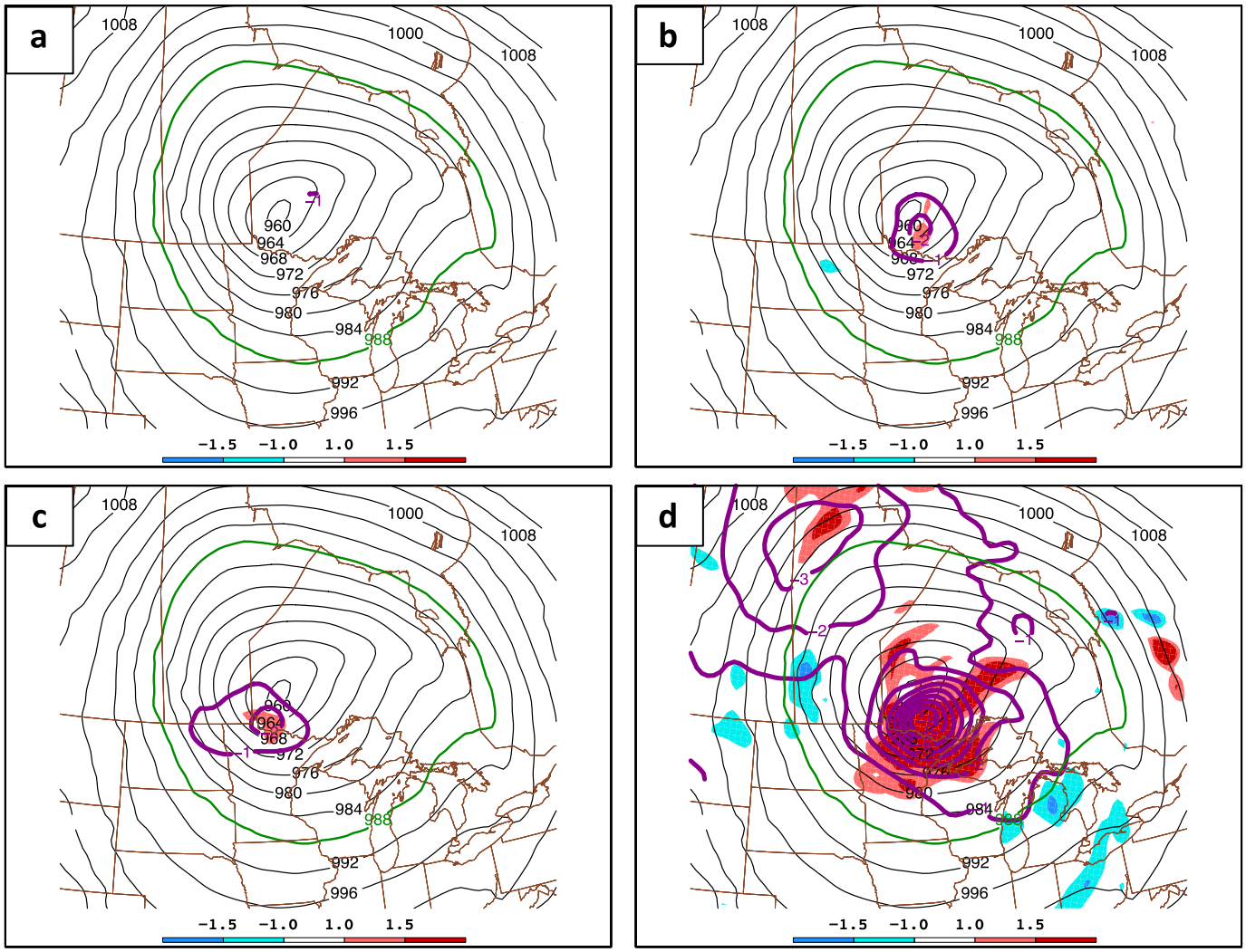

Figure 4.11. Perturbation maps for 0000 UTC 27 October 2010: (a) Non-optimal upper tropospheric wind perturbation resultant difference in sea level pressure between control and perturbed simulations (purple contours, interval -1 hPa), 650 hPa perturbation temperature (red fill, warm beginning at 1°C; blue fill, cold beginning at -1°C; interval 0.5°C), control sea level pressure (black contours, interval 4 hPa), and area in which response function is defined (988 hPa control SLP contour, in green); (b) same as in (a) except for non-optimal mid-tropospheric wind perturbations; (c) same as in (a) except for non-optimal mid-tropospheric temperature perturbations; (d) same as in (a) except for optimal wind and temperature perturbations.

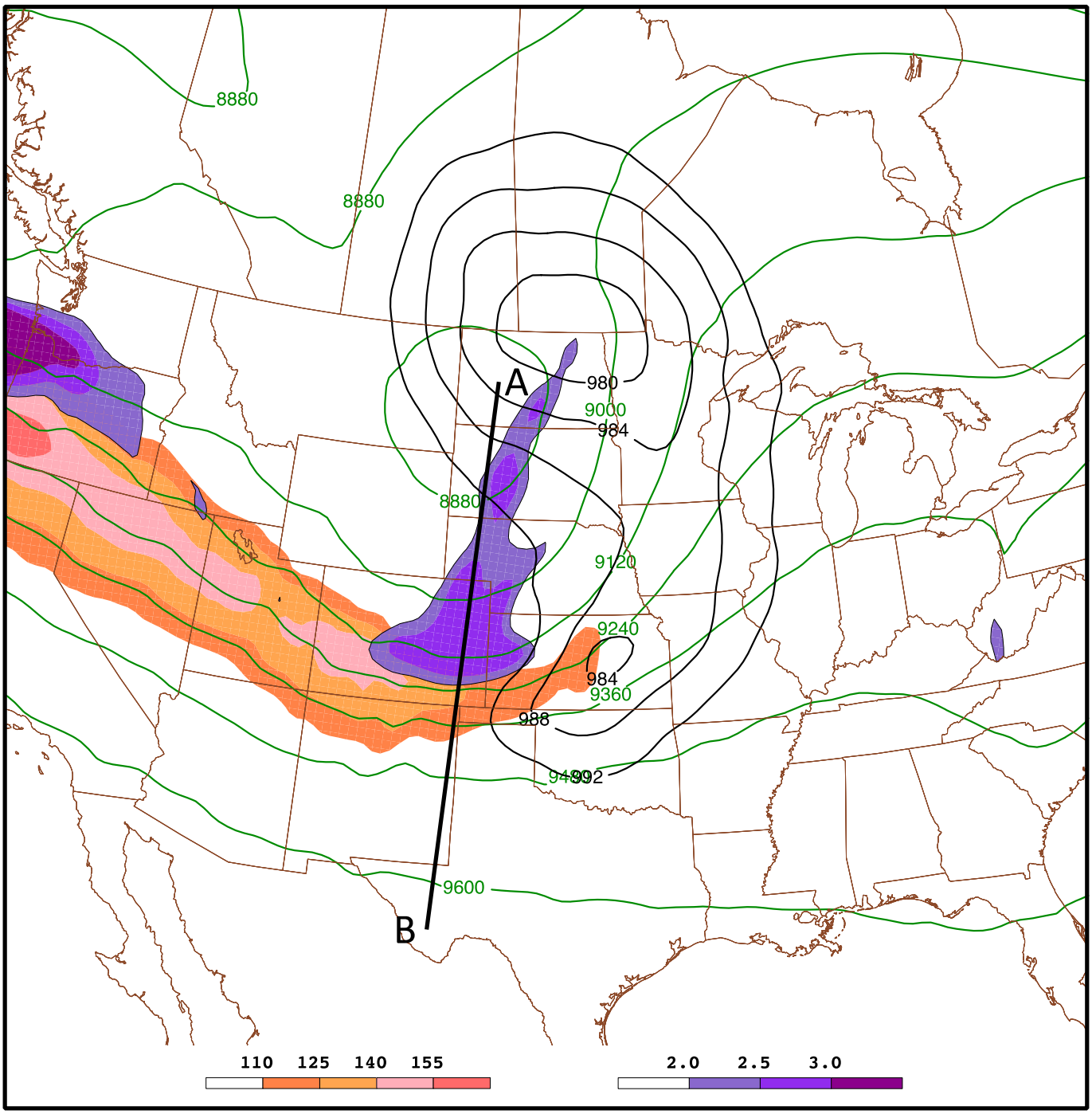

Figure 4.12. 0000 UTC 26 October synoptic chart. 350 to 450 hPa layer PV (purple fill, beginning at $2x10^{-5}s^{-1}$, interval $0.5x10^{-5}s^{-1}$), 300 hPa geopotential height (green contours, interval 120 m), 300 hPa isotachs (peach fill, interval 15 knots above 110 knots), and sea level pressure (black contours, interval 4 hPa lower than 992 hPa), at the time in which the southern cyclone begins to develop over Kansas. The line A-B is the location in which the cross section is taken in Fig. 13.

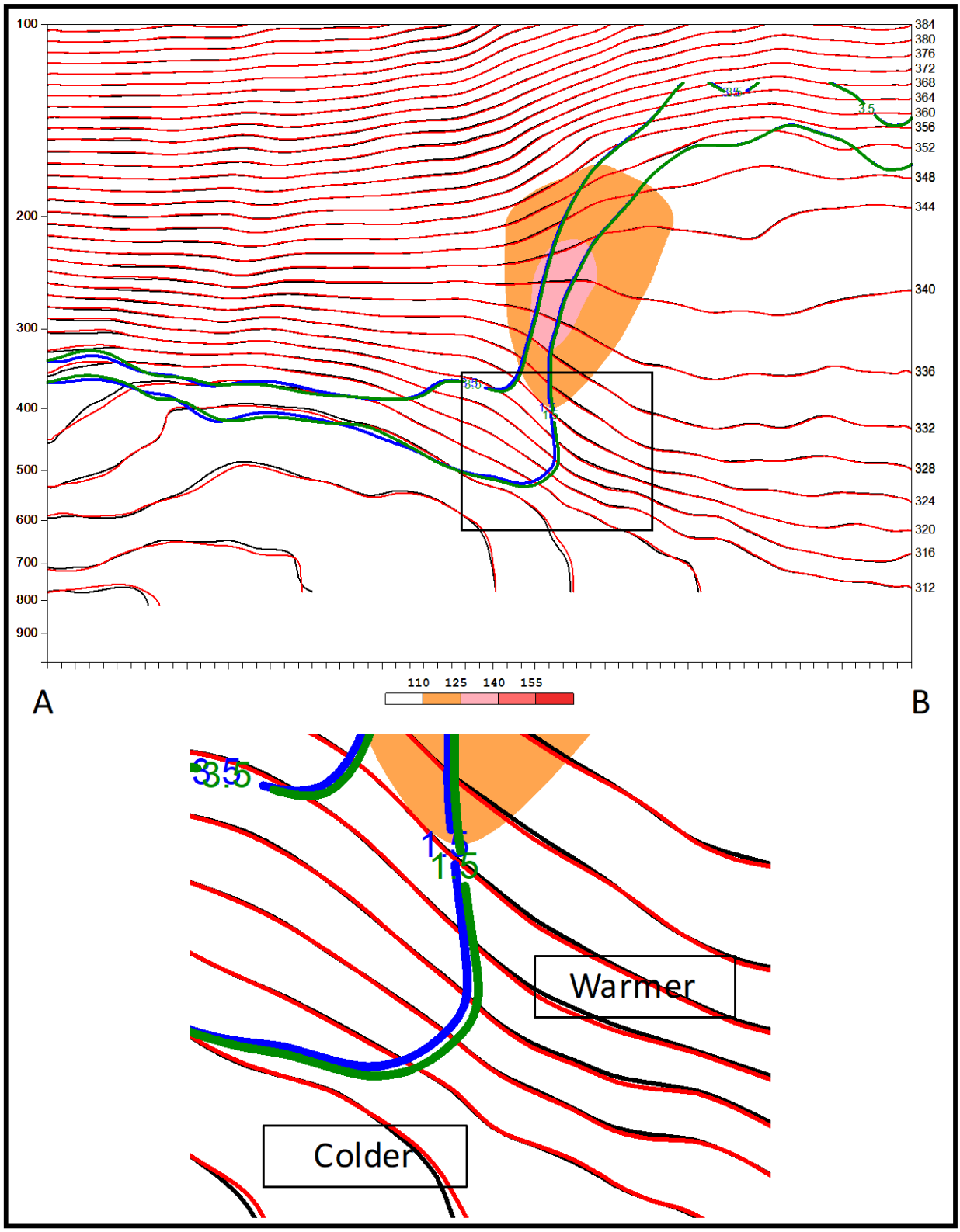

Figure 4.13. 0000 UTC 26 October cross section along line A-B as indicated in fig 12. 1.5 and 3.5 PVU surfaces (blue contours, control simulation; green contours, perturbed mid-tropospheric temperature simulation; scaled by $1x10^{-5}s^{-1}$), potential temperature (black contours, control simulation; red contours, perturbed mid-tropospheric temperature simulation; interval 4K), isotachs (peach fill, interval 15 knots above 110 knots), region of inset indicated by black box, and indication of cooler (blue shading) and warmer (red shading) air temperatures within inset affirming an increased temperature gradient along the pre-existent upper front.

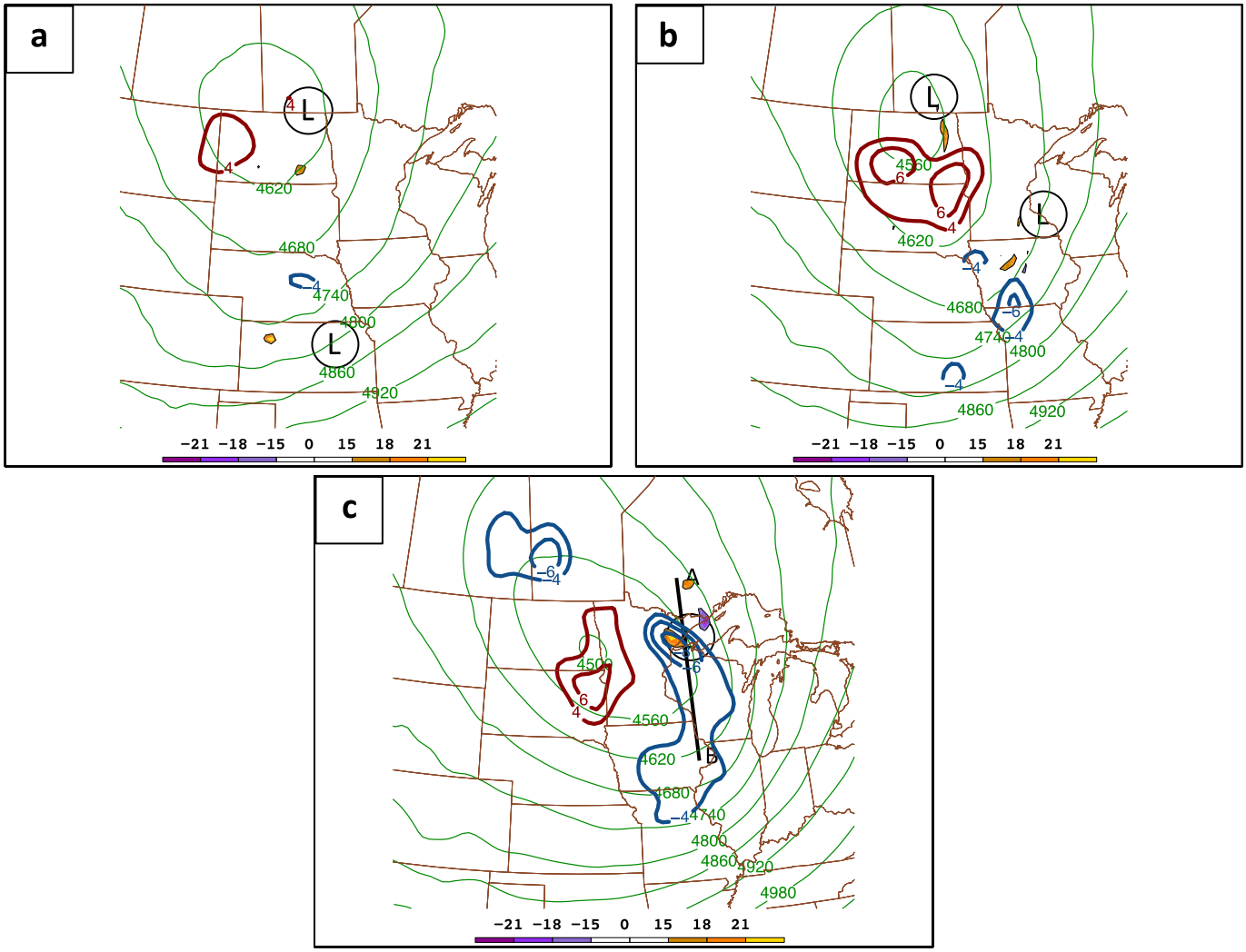

Figure 4.14. Analysis of 550 hPa vorticity and height differences between the control and the perturbed mid-tropospheric temperature simulations. (a) 0000 UTC 26 Oct relative vorticity perturbations (gold fill, positive beginning at $15x10^{-5}s^{-1}$; purple fill, negative beginning at $-15x10^{-5}s^{-1}$, interval $3x10^{-5}s^{-1}$), regions of geopotential height perturbations (dark blue contours, decrease beginning at -4 m; dark red contours, increase beginning at 4 m, interval 2 m), and locations of surface cyclones denoted by 'L'. (b) Same as in (a) except for 0600 UTC 26 Oct. (c) Same as in (a) except for 1200 UTC 26 Oct. Location of fig 15 cross section along line A-B also depicted.

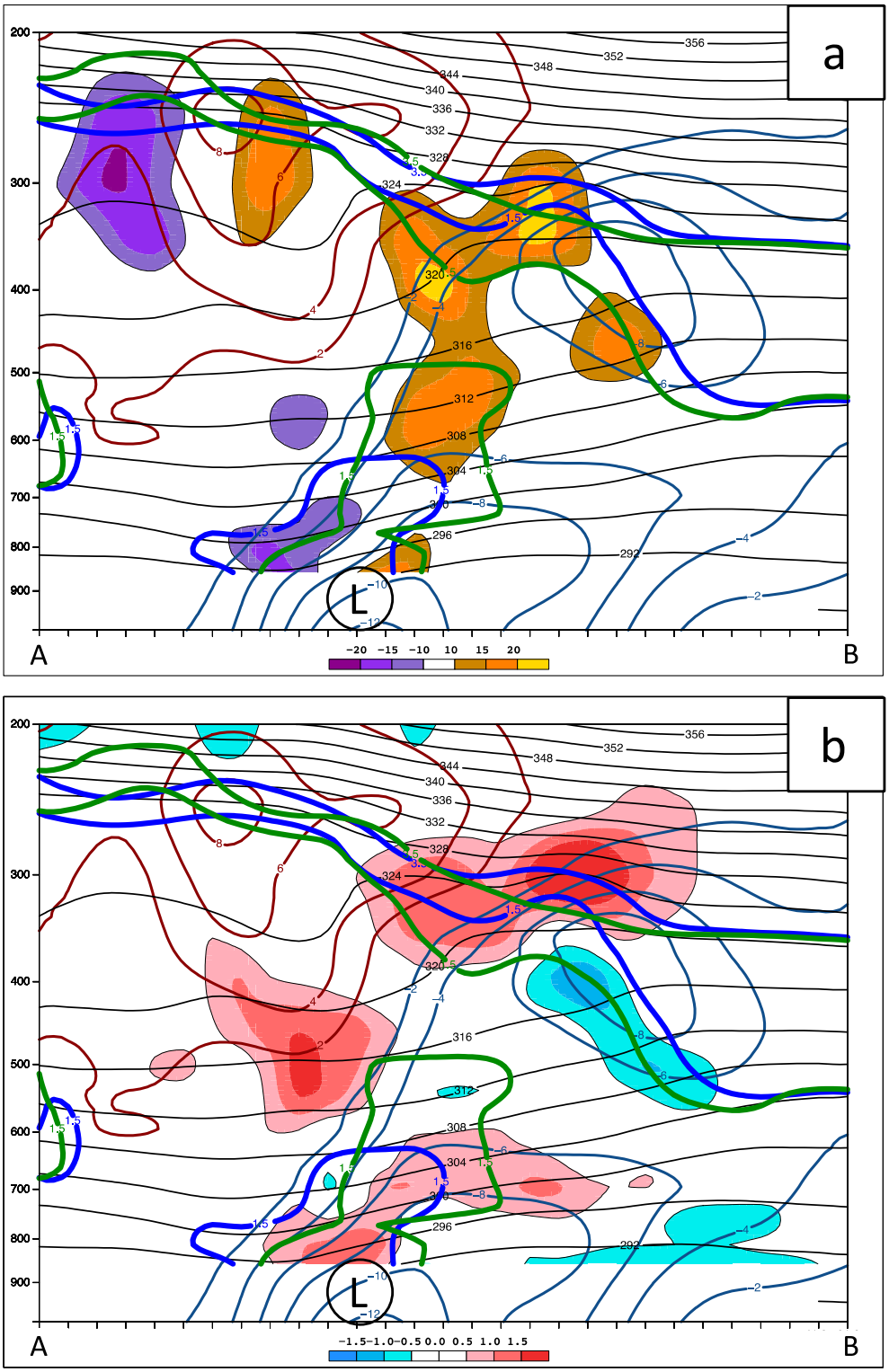

Figure 4.15. 1200 UTC 26 October cross section taken along line A-B denoted in fig 14c. (a) potential temperature (black contours, interval 4K), 1.5 and 3.5 PVU surfaces (blue contours, control simulation; green contours, perturbed mid-tropospheric temperature simulation; scaled by $1x10^{-5}s^{-1}$), regions of geopotential height perturbations (dark blue contours, decrease beginning at -2 m; dark red contours, increase beginning at 2 m, interval 2 m), relative vorticity perturbations (gold fill, positive beginning at $10x10^{-5}s^{-1}$; purple fill, negative beginning at $-10x10^{-5}s^{-1}$, interval $5x10^{-5}s^{-1}$), and locations of surface cyclone denoted by 'L'. (b) Same as in (a) except fill patterns now represent temperature perturbations (red fill, warm beginning at 0.5°C; blue fill, cold beginning at -0.5°C, interval 0.5°C).

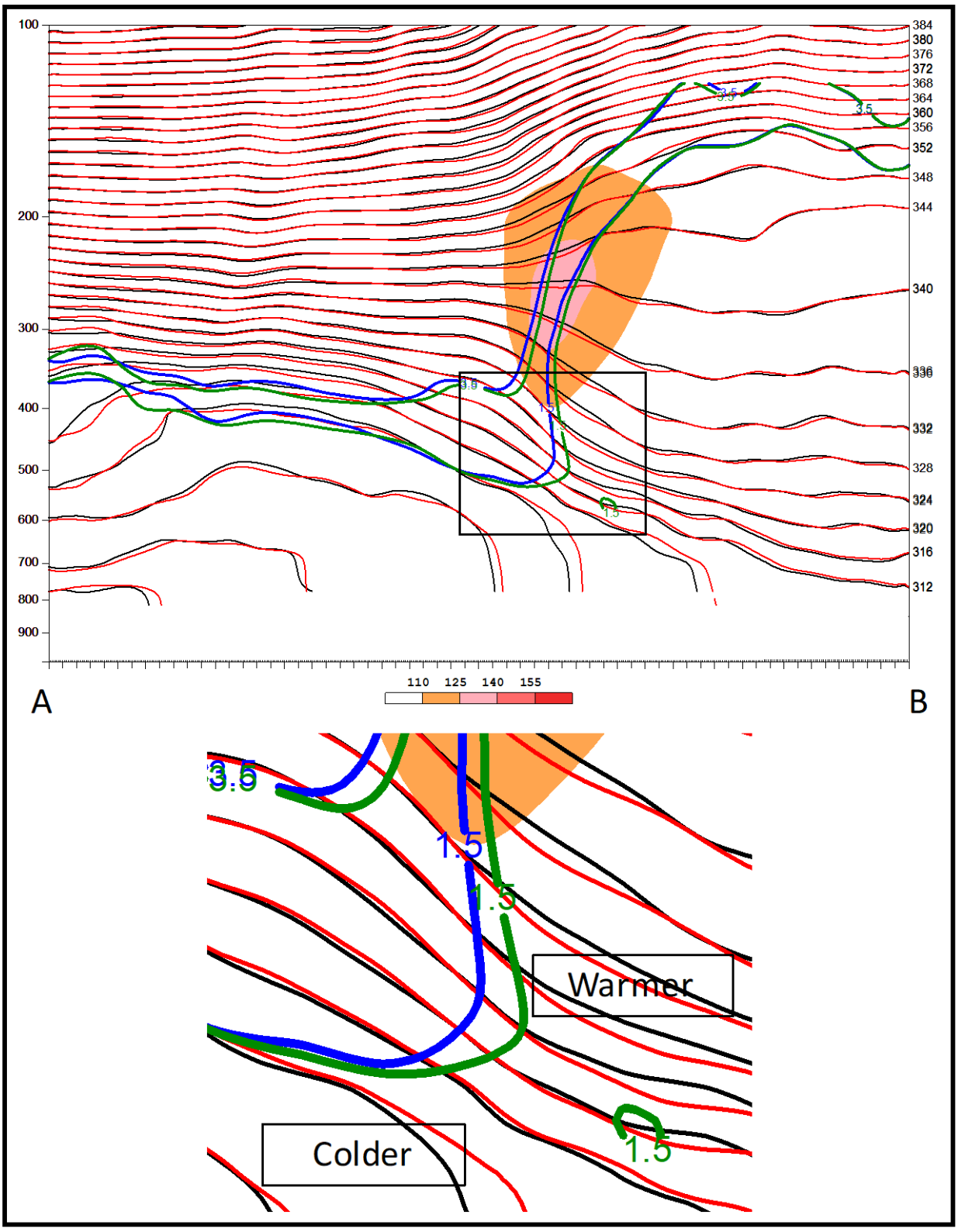

Figure 4.16. 0000 UTC 26 October cross section along line A-B as indicated in fig 12. 1.5 and 3.5 PVU surfaces (blue contours, control simulation; green contours, optimally perturbed simulation; scaled by $1x10^{-5}s^{-1}$), potential temperature (black contours, control simulation; red contours, optimally perturbed simulation; interval 4K), isotachs (peach fill, interval 15 knots above 110 knots), region of inset indicated by black box, and indication of cooler (blue shading) and warmer (red shading) air temperatures within inset affirming an increased temperature gradient along the pre-existent upper front.

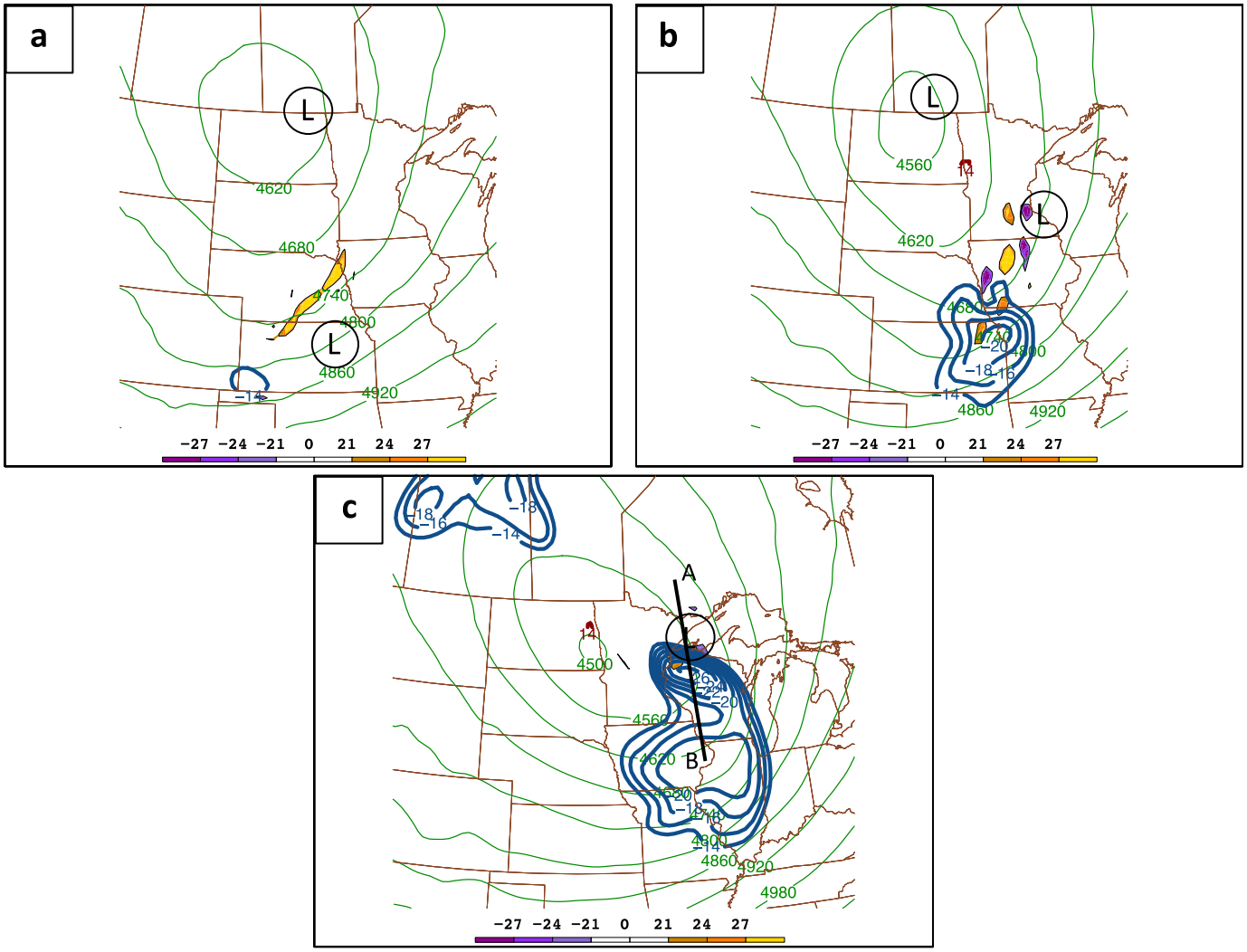

Figure 4.17. Analysis of 550 hPa vorticity and height differences between the control and the optimally perturbed simulations. (a) 0000 UTC 26 Oct relative vorticity perturbations (gold fill, positive beginning at $21 \times 10^{-5} s^{-1}$; purple fill, negative beginning at $-21 \times 10^{-5} s^{-1}$, interval $3 \times 10^{-5} s^{-1}$), regions of geopotential height perturbations (dark blue contours, decrease beginning at -14 m; dark red contours, increase beginning at 14 m, interval 2 m), and locations of surface cyclones denoted by 'L'. (b) Same as in (a) except for 0600 UTC 26 Oct. (c) Same as in (a) except for 1200 UTC 26 Oct. Location of fig 18 cross section along line A-B also depicted.

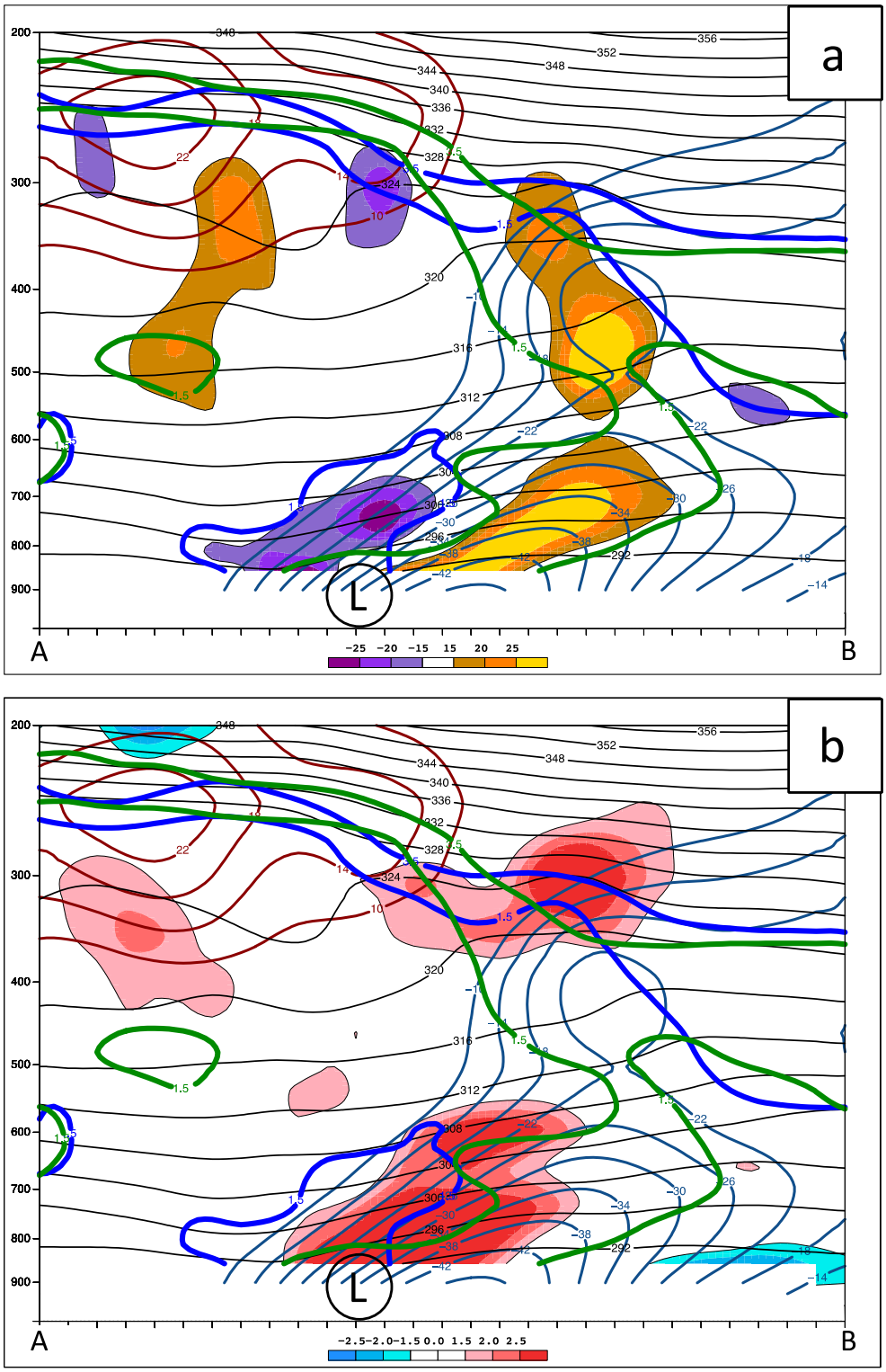

Figure 4.18. 1200 UTC 26 October cross section taken along line A-B denoted in fig 17c. (a) potential temperature (black contours, interval 4K), 1.5 and 3.5 PVU surfaces (blue contours, control simulation; green contours, optimally perturbed simulation; scaled by $1x10^{-5}s^{-1}$), regions of geopotential height perturbations (dark blue contours, decrease beginning at -10 m; dark red contours, increase beginning at 10 m, interval 4 m), relative vorticity perturbations (gold fill, positive beginning at $15x10^{-5}s^{-1}$; purple fill, negative beginning at $-15x10^{-5}s^{-1}$, interval $5x10^{-5}s^{-1}$), and locations of surface cyclones denoted by 'L'. (b) Same as in (a) except fill patterns now represent temperature perturbations (red fill, warm beginning at 1.5°C; blue fill, cold beginning at -1.5°C, interval 0.5°C).

5. Summary and Conclusion

An investigation of upper- and mid-tropospheric precursor dynamics of a complex, explosively deepening extratropical cyclone has demonstrated the utility of adjoint-derived sensitivity analysis in diagnosing important dynamical processes. As was noted in the synoptic analysis of the event, an upper level PV anomaly associated with the jet exit region of a strong, superimposed polar and subtropical jet, initiates a cyclonic surface circulation over Montana and North Dakota through Petterssen Type-B cyclogenesis. This circulation, paired with a strong southerly 850 hPa jet over the southern plains, is critical in helping to advect warm, moist air northward. As the upper level wave evolves and the northwest to southeast oriented jet over the western United States continues to dig south, the PV anomaly associated with the jet exit region shifts from Wyoming to Colorado. Due to this, further development of the northern cyclone located over Montana and North Dakota slows as there is no longer strong upper-level forcing to further its development. Once over Colorado, lee cyclogenesis takes effect as air parcels containing high vorticity are advected over the Colorado Front Range. Due to the northern circulation and 850 hPa southerly jet, there exists a strong region of baroclinicity along the east slope of Colorado and into Kansas. This synoptic set up is quite ideal for rapid development of a surface cyclone, which was observed in this event. A southern cyclone begins to develop explosively over Kansas and begins to track to the northeast. Once over western Lake Superior the two surface circulations merge and continue to develop until the end of the model simulation.

Adjoint-derived sensitivity analysis indicate that:

1) the regions of greatest sensitivity to wind and temperature at the initial forecast time lie directly below the jet within the mid-troposphere and near the subjectively identified upper-to-mid-tropospheric precursor;
2) an increase in the amplitude of the wave and an increase in the vorticity are key to increasing the intensity of the control cyclone (as measured by the response function chosen);
3) a strengthening of the tropopause fold, and the PV associated with it, is the most effective way to strengthen the surface cyclone. This is indicated by both the adjoint-informed

(optimal and non-optimal) perturbations to vorticity and temperature as interpreted through Ertel PV;

4) a strong sensitivity to temperature pattern near the surface in the region of the developing southern cyclone indicates that an increase in the baroclinicity becomes critical during the initial stage of cyclogenesis 24 hours into the model integration, but not thereafter. Together, these two patterns are indicative of enhanced Petterssen Type-B cyclogenesis.

By using adjoint-informed non-optimal and non-balanced perturbations, a better understanding of the adjustment process of the model atmosphere and its resultant effect on cyclone development can be attained. Non-optimal wind perturbations with a maximum value of 2.1 m s^{-1} have been calculated for upper model levels between levels 27 and 31, which interpolated to pressure coordinates is approximately 200 to 400 hPa. Non-optimal perturbations to wind *and* temperature have been calculated for middle model levels. The maximum perturbation to wind is 1.7 m s^{-1} and the maximum perturbation to temperature is 1.5K. These perturbations are inserted in the same horizontal area as the upper level perturbations and lie between eta levels 16 and 20, which interpolated to pressure coordinates is approximately 400 to 650 hPa. Optimal perturbations have also been calculated and used to perturb the model at the initial time to identify the most effective means of increasing the strength of the cyclone using the least amount of energy. The optimal perturbations have been calculated throughout the depth of the model atmosphere and over the entire domain.

An examination of the distribution of the optimal perturbations at the initial forecast time show that cold advection below the jet maximum, upstream of the mid-level trough axis, is indeed the most ideal region to perturb the initial state to achieve enhanced cyclogenesis. This is also the region in which the mid-level non-optimal perturbations were calculated and inserted. Examination of the resultant deviation of the forecast from the control shows that an enhancement of the tropopause fold and upper front does indeed occur in the case of the optimal perturbations and both mid-tropospheric non-optimal perturbation cases. Non-optimal wind perturbations made directly at jet level had very little impact on development. The subsequent advection of the enhanced PV anomaly downstream effectively lowers mid-tropospheric

geostrophic heights in the base of the trough as described by the QG height tendency equation. The deepening of the trough then adds to the production of relative vorticity by curvature in a location that is upshear of the rapidly intensifying surface cyclone, which is ideal for enhanced development of the surface cyclone compared to the control.

In all cases the perturbations had the intended impact on the intensity of the cyclone as measured by the response function in that the observed change, ΔR, was of the same sign as the prescribed change, δR. The ratio of these quantities, $\Delta R / \delta R$, representing the degree to which the assumption of linearity appropriately approximates the impact of perturbations in the nonlinear model, was equal to 43% for the non-optimally perturbed mid-tropospheric temperature simulation and 53% for the optimally perturbed simulation and is deemed within reason for the study considered here. It was observed also that both optimal and non-optimal perturbations shifted the cyclone slightly to the south nearer the position in the NCEP analysis data at the final forecast time.

It has been seen that the development and application of adjoint derived analysis tools are extremely useful in completing a diagnoses of a complex cyclogenesis event. Adjoint techniques have been proven useful in the diagnosis of the most important precursor dynamics relevant to extratropical cyclogenesis in works by Doyle et al. (2013) and Errico and Vukicevic (1991). These studies have indicated that low- to mid-level dynamics are *generally* most critical to cyclogenesis, but lack an in-depth analysis of upper level dynamics utilizing these techniques. The upper-tropospheric diagnostics completed here have shown that adjoint-derived sensitivity analyses are *indeed* extremely useful in this regard. Further development of these tools will hopefully allow a sensitivity study of other pertinent dynamics to be completed, such as sensitivity to PV. The techniques used here can also be further applied to the study of other extratropical cyclogenesis events in order to help understand what sensitivities exist in mid-latitude weather systems that are most likely related to forecast uncertainties or forecast busts.

6. References

Ancell, B.C., and C.F. Mass, 2006: Structure, Growth Rates, and Tangent Linear Accuracy of Adjoint Sensitivities with Respect to Horizontal and Vertical Resolution. *Mon. Wea. Rev.*, **134**, 2971-2988.

Arbogast, P., 1998: Sensitivity to potential vorticity. *Q. J. R. Meteorol. Soc.*, **124**, 1605-1615.

Bannister, R.N., 2007: *Elementary 4D-VAR.* DARC Technical Report No. 2., Data Assimilation Research Centere, University of Reading, UK., 16 pp.

Barker, D.M., W. Huang, Y.-R. Guo, A.J. Bourgeois, and Q.N. Xiao, 2004: A Three-Dimensional Variational Data Assimilation System for MM5: Implementation and Initial Results. *Mon. Wea. Rev.*, **132**, 897-914.

Bjerknes, J., 1919: On the Structure of Moving Cyclones. *Mon. Wea. Rev.*, 95-99.

Cacuci, D.G., and M.C.G. Hall, 1984: Efficient Estimation of Feedback Effects with Application to Climate Models. *Journ. Atmos. Sci.*, **41**, 2063-2068.

Carlson, T.N., 1961: Lee-side frontogenesis in the Rocky Mountains. *Mon. Wea. Rev.*, **89**, 163-172.

Chung, Y.-S., K.D. Hage, and E.R. Reinelt, 1976: On Lee Cyclogenesis and Airflow in the Canadian Rocky Mountains and the East Asian Mountains. *Mon. Wea. Rev.*, **104**, 879-891.

Doyle, J.D., C. Amerault, C.A. Reynolds, and P.A. Reinecke, 2014: Initial Condition Sensitivity and Predictibility of a Severe Extratropical Cyclone Using a Moist Adjoint. *Mon. Wea. Rev.*, **142**, 320-342.

Eady, E.T., 1949: Long Waves and Cyclone Waves. *Tellus.*, **1:3**, 33-52.

Eichler, T., and W. Higgins, 2006: Climatology and ENSO-Related Variability of North American Extratropical Cyclone Activity. *Journ. Climate.*, **19**, 2076-2093.

Eliassen, A., 1962: On the Vertical Circulation in Frontal Zones. *Geofys. Publ.*, **24**, 147-160.

Errico, R.M., and T. Vukicevic, 1992: Sensitivity Analysis Using an Adjoint of the PSU-NCAR Mesoscale Model. *Mon. Wea. Rev.*, **120**, 1644-1660.

Errico, R.M., T. Vukićević, and K. Raeder, 1993: Examination of the accuracy of a tangent linear model. *Tellus.*, **45**, 462-477.

Errico, R.M., 1997: What is an Adjoint Model? *Bull. Amer. Meteorol. Soc.,* **78**, 2577-2591.

Gaza, R.S., and L.F. Bosart, 1990: Trough-Merger Characteristics over North America. *Wea. Fore.*, **5**, 314-331.

Gerhardt, M.B.: Midwest High Wind Event October 25th – October 27th 2010. *National Weather Service.*

Giering, R., and T. Kaminski, 1996: *Recipes for adjoint code construction.* Internal Report 212 from Max-Plank Institute fur Meteorologie, Hamburg, Germany., 35 pp.

Grumm, R.H.: The Historic Storm of 24-26 October 2010-Draft. *National Weather Service.*

Hakim, G.J., L.F. Bosart, and D. Keyser, 1995: The Ohio Valley Wave-Merger Cyclogenesis Event of 25-26 January 1978. Part I: Multiscale Case Study. *Mon. Wea. Rev.*, **123**, 2663-2692.

Hakim, G.J., D. Keyser, L.F. Bosart, 1996: The Ohio Valley Wave-Merger Cyclogenesis Event of 25-26 January 1978. Part II: Diagnosis Using Quasigeostrophic Potential Vorticity Inversion. *Mon. Wea. Rev.*, **124**, 2176-2205.

Hall, M.C.G., Cacuci, D.G., and M.E. Schlesinger, 1982: Sensitivity Analysis of a Radiative-Convective Model by the Adjoint Method. *Journ. Atmos. Sci.*, **39**, 2038-2050.

Hall, M.C.G., and Cacuci, D.G., 1983: Physical Interpretation of the Adjoint Functions for Sensitivity Analysis of Atmospheric Models. *Journ. Atmos. Sci.*, **40**, 2537-2546.

Holdaway, D., R. Errico, R. Gelaro, and J.G. Kim, 2014: Inclusion of linearized moist physics in NASA's Goddard Earth Observing System data assimilation tools. *Mon. Wea. Rev.*, **142**, 414-433.

Homar, V., and D.J. Stensrud, 2004: Sensitivities of an intense Mediterranean cyclone: Analysis and validation. *Q. J. R. Meteorol. Soc.*, **130**, 2519-2540.

Hoover, B.T., 2010: *Dynamical Sensitivity Analysis of Tropical Cyclone Steering and Genesis Using an Adjoint Model.*, 132 pp.

Hoskins, B.J., M.E. McIntyre, and A.W. Robertson, 1985: On the use and significance of isentropic potential vorticity maps. *Royal Met. Soc.*, **111**, 877-946.

Hoskins, B., M. Pedder, and D. Wyn Jones, 2003: The omega equation and potential vorticity. *Q. J. R. Meteorol. Soc.*, **129**, 3277-3303.

Jung, B.-J., H.M. Kim, 2009: Moist adjoint-based forecast sensitivities for a heavy snowfall event over the Korean Peninsula on 4-5 March 2004. *Journ. Geophys. Rea.*, **114**, D15104.

Kekuan, C., and Y. Zhang, 2016: Adjoint Sensitivity Study on Idealized Explosive Cyclogenesis. *Journ. Meteorol. Res.*, **30**, 547-558.

Kiladis, G.N., K.M. Weickmann, 1992: Circulation Anomalies Associated with Tropical Convection during Northern Winter. *Mon. Wea. Rev.*, **120**, 1900-1923.

Kim, H.M., and R.J. Beare, 2011: Characteristics of adjoint sensitivity to potential vorticity. *Meteorol. Atmos. Phys.*, **111**, 91-102.

Kleist, D.T., and M.C. Morgan, 2005a: Interpretation of the Structure and Evolution of Adjoint-Derived Forecast Sensitivity Gradients. *Mon. Wea. Rev.*, **133**, 466-484.

Kleist, D.T., and M.C. Morgan, 2005b: Application of adjoint-derived forecast sensitivities to the 24-25 January 2000 U.S. east coast snowstorm. *Mon. Wea. Rev.*, **133**, 3148-3175.

Kucharski, F., and A.J. Thorpe, 2001: The influence of transient upper-level barotropic growth on the development of baroclinic waves. *Q. J. R. Meteorol. Soc.*, **127**, 835-844.

Kuo, Y.-H., M.A. Shapiro, and E.G. Donall, 1991: The Interaction between Baroclinic and Diabatic Processes in a Numerical Simulation of a Rapidly Intensifying Extratropical Marine Cyclone. *Mon. Wea. Rev.*, **119**, 368-384.

Lagouvardos, K., V. Kotroni, and E. Defer, 2007: The 21-22 January 2004 explosive cyclogenesis over the Aegean Sea: Observations and model analysis. *Q. J. R. Meteorol. Soc.*, **133**, 1519-1531.

Langland, R.H., R.L. Elsberry, and R.M. Errico, 1995: Evaluation of physical processes in an idealized extratropical cyclone using adjoint sensitivity. *Q. J. R. Meteorol. Soc.*, **121,** 1349-1386.

Langland, R.H., R.L. Elsberry, and R.M. Errico, 1996: Adjoint sensitivity of an idealized extratropical cyclone with moist physical processes. *Q. J. R. Meteorol. Soc.*, **122**, 1891-1920.

Langland, R.H., M.A. Shapiro, and R. Gelaro, 2002: Initial Condition Sensitivity and Error Growth in Forecasts of the 25 January 2000 East Coast Snowstorm. *Mon. Wea. Rev.,* **130**, 957-974.

Lorenc, A.C., 2003: Modelling of error covariances by 4D-Var data assimilation. *Q. J. R. Meteorol. Soc.*, **129**, 3167-3182.

Lorenc, A.C., 2003: The potential of the ensemble Kalman filter for NWP – a comparison with 4D-Var. *Q. J. R. Meteorol. Soc.*, **129**, 3183-3203.

Martin, J.E., 2006: *Midlatitude Atmospheric Dynamics: A First Course.* John Wiley and Sons., 336 pp.

Martin, J.E., 2014: Quasi-geostrophic diagnosis of the influence of vorticity advection on the development of upper level jet-front systems. *Q. J. R. Meteorol. Soc.*, **140**, 2658-2671.

Mattocks, C., and R. Bleck, 1986: Jet Streak Dynamics and Geostrophic Adjustment Processes during the Initial Stages of Lee Cyclogenesis. *Mon. Wea. Rev.,* **114**, 2033-2056.

McGinley, J., 1982: A Diagnosis of Alpine Lee Cyclogenesis. *Mon. Wea. Rev.*, **110**, 1271-1287.

Nuss, W.A., and R.A. Anthes, 1987: A Numerical Investigation of Low-Level Processes in Rapid Cyclogenesis. *Mon. Wea. Rev.*, **115**, 2728-2743.

Palmén, E., and C.W. Newton, 1969: *Atmospheric Circulation Systems.* Academic Press., 334-335.

Park, S.K., and D. Županski, 2003: Four-dimensional variational data assimilation for mesoscale and storm-scale applications. *Meteorol. Atmos. Phys.*, **82**, 173-208.

Petterssen, S., and S.J. Smebye, 1971: On the development of extratropical cyclones. *Q. J. R. Meteorol. Soc.*, **97**, 457-482.

Rabier, F., H. Järvinen, E. Klinker, J.-F. Mahfouf, and A. Simmons, 2000: The ECMWF operational implementation of four-dimensional variational assimilation. I: Experimental

results with simplified physics. *Q. J. R. Meteorol. Soc.*, **126**, 1143-1170.

Ranson, M., L. Tarquinio, and A. Lew, 2016: Modeling the Impact of Climate Change on Extreme Weather Losses. *NCEE., Working Paper #16-02.*, 94 pp.

Reeder, M.J., and D. Keyser, 1988: Balanced and Unbalanced Upper-Level Frontogenesis. *Journ. Atmos. Sci.*, **45**, 3366-3386.

Sawyer, J.S., 1956: The vertical circulation at meteorological fronts and its relation to frontogenesis. *Proc. Roy. Soc. Lon.*, **234**, 346-362.

Shapiro, M.A., D. Keyser, 1990: Fronts, Jet Streams and the Tropopause. *Extratropical Cyclones: The Erik Palmén Memorial Volume.* C.W. Newton and E.O. Holopainen, Eds., Amer. Meteor. Soc., 167-191.

Steenburgh, W.J., and C.F. Mass, 1994: The structure and evolution of a simulated Rocky Mountain lee trough. *Mon. Wea. Rev.*, **122**, 2740-2761.

Thépaut, J.-N., and P. Courtier, 1991: Four-dimensional variational data assimilation using the adjoint of a multilevel primitive-equation model. *Q. J. R. Meteorol. Soc.*, **117**, 1225-1254.

Torn, R.D., and G.J. Hakim, 2008: Ensemble-Based Sensitivity Analysis. *Mon. Wea. Rev.*, **136,** 663-667.

Torn, R.D., and G.J. Hakim, 2009: Initial Condition Sensitivity of Western Pacific Extratropical Transitions Determined Using Ensemble-Based Sensitivity Analysis. *Mon. Wea. Rev.*, **137**, 3388-3406.

Vukićević, T., 1991: Nonlinear and Linear Evolution of Initial Forecast Errors. *Mon. Wea. Rev.*, **119**, 1602-1611.

Vukićević, T., and R.M. Errico, 1993: Linearization and adjoint of parameterized moist diabatic processes. *Tellus.*, **45**, 493-510.

Vukićević, T., and K. Raeder, 1995: Use of an Adjoint Model for Finding Triggers for Alpine Lee Cyclogenesis. *Mon. Wea. Rev.*, **123**, 800-816.

Wang, H., and Y. Wang, 2014: A Numerical Study of Typhoon Megi (2010). Pat I: Rapid Intensification. *Mon. Wea. Rev.*, **142**, 29-48.

Whittaker, L.M., and L.H. Horn, 1984: Northern Hemisphere Extratropical Cyclone Activity for Four Mid-season Months. *Journ. Clim.*, **4**, 297-310.

Wu, C.-C., S.-G. Chen, J.-H. Chen, K.-H. Chou, and P.-H. Lin, 2009: Interaction of Typhoon Shanshan (2006) with the Midlatitude Trough from both Adjoint-Derived Sensitivity Steering Vector and Potential Vorticity Perspectives. *Mon. Wea. Rev.*, **137**, 852-862.

Zhang, X., and X.-Y. Huang, 2013: Development of the Upgraded Tangent Linear and Adjoint of the Weather Research and Forecasting (WRF) Model. *Journ. Atm. Ocn. Tech.*, **30**, 1180-1188.

Zhu, H., and A. Thorpe, 2006: Predictability of Extratropical Cyclones: The Influence of Initial Condition Model Uncertainties. *Journ. Atm. Sci.*, **63**, 1483-1497.

Zou X., F. Vandenberghe, M. Pondeca, and Y.-H. Kuo, 1997*: Introduction to adjoint techniques and the MM5 adjoint modeling system.* NCAR technical notes., NCAR/TN-435-STR., 110 pp.